Atom-Photon Entanglement

Dissertation at the Department of Physics
of the
Ludwig-Maximilians-Universität München

Jürgen Volz

München, March 21, 2006

meinen Eltern

Zusammenfassung

Verschränkung ist das Schlüsselelement vieler Experimente in der Quantenkommunikation und -information. Besonders im Hinblick auf zukünftige Anwendungen wie den Aufbau von Quantennetzwerken ist Verschränkung von unterschiedlichen Quantensystemen wie z.B. Atomen und Photonen unentbehrlich, da sie die Schnittstelle zwischen atomaren Quantenspeichern und optischen Kommunikationskanälen darstellt und die Verteilung von Verschränkung über große Entfernungen ermöglicht. Darüber hinaus ist Atom-Photon-Verschränkung das Hauptelement zur Beantwortung von Einsteins Frage, ob eine lokale und realistische Beschreibung der Realität möglich ist oder nicht. Bisher wurde anhand der Verletzung der Bellschen Ungleichung in verschiedenen Experimenten gezeigt, dass lokale realistische Theorien keine gültige Beschreibung der Realität darstellen. Allerdings mussten in all diesen Experimenten Annahmen getroffen werden, die eine vollständige Widerlegung dieser Theorien unmöglich machte. In diesem Zusammenhang stellt Atom-Photon Verschränkung einen entscheidenden Schritt zur Realisierung eines endgültigen Tests der Bellschen Ungleichung mit Hilfe zweier verschränkter Atome dar, bei dem keine zusätzlichen Annahmen benötigt werden.

Diese Arbeit beschreibt die Erzeugung und den Nachweis eines verschränkten Zustands zwischen einem einzelnen Atom und einem einzelnen Photon, mit einer zur Informationsübertragung geeigneten Wellenlänge. Zu diesem Zweck wird ein einzelnes ^{87}Rb Atom in einer optischen Dipolfalle gefangen. Anschließend wird es in einem angeregten Zustand präpariert, der zusammen mit seinen beiden möglichen Zerfallskanälen ein sogenanntes Λ-System bildet. Aufgrund der Drehimpulserhaltung entsteht in dem darauffolgenden spontanen Zerfall ein verschränkter Zustand zwischen dem atomaren Drehimpuls und der Polarisation des emittierten Photons. Der Nachweis der Verschränkung erfolgt durch eine atomare Zustandsmessung, die auf einem zustandsselektiven adiabatischen Populationstransfer basiert. Diese Methode erlaubt eine Analyse des internen atomaren Zustands in beliebigen Messbasen ohne Zuhilfenahme zusätzlicher Manipulationen am atomaren Quantenbit. Zusammen mit einer Polarisationsmessung des emittierten Photons wurden Korrelationsmessungen sowie eine komplette Zustandstomographie des Atom-Photon Zustands durchgeführt. Die experimentellen Resultate zeigen eine Güte des verschränkten Zustands von 87%, wodurch die Verschränkung des Zustand eindeutig verifiziert wird.

Der in unserem Experiment beobachtete Grad an Verschränkung ist hoch genug um zwei entfernte Atoms durch Verschränkungstransfer zu verschränken und damit einen endgültigen Test der Bellschen Ungleichung durchzuführen, der keine Schlupflöcher für lokale realistische Theorien mehr bietet. Desweiteren bildet die beobachtete Verschränkung eine wichtige Ressource für mögliche Anwendungen in der Quanteninformationsverarbeitung und Quantenkommunikation.

Summary

Entanglement is the key element for many experiments in quantum communication and information. Especially for future applications like quantum networks or the quantum repeater it is mandatory to achieve entanglement also between separated quantum processors. For this purpose, entanglement between different quantum objects like atoms and photons forms the interface between atomic quantum memories and photonic quantum communication channels, finally allowing the distribution of quantum information over arbitrary distances. Furthermore, atom-photon entanglement is also the key element to give the final answer to Einstein's question wether a local and realistic description of physical reality is possible or not. Until now, the results of many experiments testing Bell's inequality indicate that local realistic theories are not a valid description of nature. However, all these tests were subject to loopholes. In this context, atom-photon entanglement represents a crucial step towards the realization of entanglement between distant atoms that would allow a final loophole-free test of Bell's inequality.

This thesis describes the generation and verification of an entangled state between a single neutral atom and a single photon at a wavelength suitable for long distance information transport. For this purpose we store a single ^{87}Rb atom in an optical dipole trap. The atom is prepared in an excited state, that together with its two decay channels forms a Λ-type transition. In the following spontaneous decay, conservation of angular momentum leads to the formation of an entangled state between the angular momentum of the atom and the polarization of the emitted photon. To verify the entanglement we introduce an atomic state-analysis, based on a state-selective adiabatic population transfer between atomic hyperfine levels. This allows the direct analysis of the internal state of the atom in arbitrary measurement bases without the necessity of additional state manipulations. Using this method together with a polarization measurement of the emitted photon, we performed correlation measurements as well as a full state tomography of the combined atom-photon system. From the experimental results we obtain an entanglement fidelity of 87%, which clearly shows that the generated state is entangled.

The degree of entanglement observed in our experiment is high enough to allow the generation of entanglement between distant atoms via entanglement swapping, which would allow a final, loophole-free test of Bell's inequality. Furthermore, it opens up a variety of applications in quantum communication and information science.

Contents

1. Introduction

"Those who are not shocked when they first come across quantum mechanics cannot possibly have understood it.", is a statement of Niels Bohr and expresses the attitude of many physicists in the early days of quantum mechanics towards the then new theory. Especially non-separable two- (or many-) particle states, so-called entangled states, with their high degree of correlation between measurement results were the origin of vivid discussions. In 1935 Einstein, Podolsky and Rosen (EPR) [1] addressed this problem in a Gedankenexperiment. From the conditions of realism and locality, that are – according to them – essential for every physical theory, they concluded by means of an entangled two-particle state that quantum mechanics is not complete. Hence, EPR motivated an extension of quantum theory by so-called local hidden variables that would complete quantum mechanics and restore determinism.

The original Gedankenexperiment by EPR did not point at observable differences between quantum theory and a local realistic description of nature. Therefore, their argument was merely considered a philosophical question. In 1964 however, Bell was able to derive an inequality [2] based on Bohm's simplified version of EPR's Gedankenexperiment [3]. Bell showed that for theories based on EPR's assumptions certain bounds exist for the expectation value of spin correlation measurements that do not hold for the predictions derived by quantum mechanics. Bell's inequality allowed for the first time experimental tests that could distinguish whether nature adheres local realism or not.

Until know many experiments have been performed testing Bell's original inequality and equivalent formulations [4, 5, 6]. The first experiments where performed using entangled photon pairs generated in the cascade decay of calcium atoms [7, 8]. A strong violation of Bell's inequality was observed in improved experiments by the group of Aspect et al. [9, 10]. They also addressed for the first time the problem of locality by performing a fast though non-random switching of the measurement bases [11].

Although the observed violation of Bell's inequality in all these experiments was in favor of quantum mechanics, the experiments were all subject to two major loopholes, that still make possible a local realistic description of the experiment. One loophole is the so-called locality loophole, that addresses the problem of possible remote interaction between the measurement apparatuses or the entangled particles [12, 13]. In 1998 the first experimental violation of Bell's inequality under strict relativistic locality conditions [14] has been performed, closing the locality loophole. However, due to the low detection efficiency of single photons, in all these experiments only a certain part of the generated entangled particles was detected. This opens up the so-called detection loophole, describing the possibility that the whole ensemble behaves according to local realism while the detected particles do not [15, 16]. This issue was addressed in an experiment using two entangled ions [17], where the high detection efficiency allowed to close the detection loophole. However, due to the small distance between the ions in this experiment the locality loophole remained open. Until now, no experiment has been

performed closing both loopholes at the same time. Thus a final loophole-free test of Bell's inequality still has to be performed to completely rule out a local realistic description of nature.

In order to close both loopholes at the same time, atom-photon entanglement is the key ingredient[1], because it allows to combine the possibility to generate long distance entanglement (mediated by photons) with the high detection efficiency of atoms. Two photons, each entangled with an atom, can be distributed far enough to ensure space-like separation. A Bell-state measurement on them serves to swap the entanglement to the atoms [20, 21, 22] whose states now can be observed with high efficiency. This enables the ideal configuration of a so called "event-ready" scheme [12, 20] which does not require any assumption at all.

Nowadays, entanglement is the main resource for applications in quantum communication and quantum information [23, 24] and entanglement between up to five photons [25, 26, 27], eight ions [28, 29] or some thousand neutral atoms in a so-called cluster state [30] has been reported. The key element of many quantum communication protocols is represented by entangled photons which can easily be transported through optical fibers or air. Therefore, they are ideal carriers of quantum information and are e.g. used for entanglement based quantum cryptography [31] or for the distribution of quantum information [32, 33, 34, 35] between remote locations. On the other hand, trapped ions or neutral atoms are an ideal resource for the reliable storage of quantum information. Together with the possibility to address and manipulate single qubits they are a promising candidate for the realization of quantum memories or quantum computers [36, 37, 38, 39].

For future applications in quantum information science as e.g. the quantum repeater [40] or quantum networks, the faithfull mapping of quantum information between a stable quantum memory and a reliable quantum communication channel is essential. Because quantum states can in general not be copied, entanglement between the quantum memory and the communication channel is necessary. Therefore, entanglement between between different species like atoms and photons is an essential resource. Combining the advantages of photons (information transport over large distances) and atoms (reliable information storage), atom-photon entanglement enables the interface between atomic quantum memories and photonic quantum communication channels and allows the distribution of quantum information over large distances.

Quantum state transfer between atoms and light has been investigated in a number of experiments using Rydberg atoms traveling through high-Q cavities [41] or the interaction between photons and the collective angular momentum of dense atomic clouds [42, 43], where also entangled states have been reported [44, 45]. However, entanglement between individual particles has only once been realized using a single trapped $^{111}Cd^+$ ion and a single photon at a wavelength of 214 nm [46].

This thesis describes the generation of an entangled state between the angular momentum of a single neutral ^{87}Rb atom and the polarization of a single photon at a wavelength of 780 nm. The entanglement is created by conservation of angular momentum in spontaneous decay

---

[1]Recently, two other experimental schemes for a loophole-free test of Bell's inequality have been proposed. These proposals rely on the homodyne detection of entangled non-Gaussian light states [18] and on the analysis of the perfect correlations present in states generated in the entanglement swapping process [19], respectively.

of the atom with two possible decay channels in a Λ-configuration. Because the decay to each of the two ground states is connected with the emission of a photon in a defined polarization state, the final atom-photon state is entangled.

The main ingredient for the generation of atom-photon entanglement is a single localized Rubidium atom, well isolated from the environment. A Single ^{87}Rb atom can efficiently be stored in an optical dipole trap and its level structure provides a good approximation to the ideal Λ-transition. Moreover, the emitted photons have a wavelength of 780 nm that allows low-loss communication through air or optical fibers as well as a highly efficient single photon detection. For the verification of entanglement it is necessary to analyze correlations between the internal atomic state and the polarization of the emitted photon. While polarization measurements of photons are straightforward, the analysis of internal atomic states in different measurement bases is more difficult. In principle it requires the ability to detect arbitrary superpositions of atomic Zeeman states. This is realized in our experiment using the stimulated Raman adiabatic passage (STIRAP) technique [47, 48, 49, 50, 51, 52], where in essence, the polarization of the STIRAP light field defines the atomic measurement basis. Using this detection process we can analyze the combined atom-photon state in any measurement basis and therefore verify whether it is entangled or not.

Overview

The second chapter of this thesis gives a short introduction into entanglement and its relevance for the EPR-paradox and the derivation of Bell's inequality. Furthermore, the generation of atom-photon entanglement in spontaneous decay is discussed and the nature of the entangled state for our experimental parameters is analyzed. Chapter three describes the characteristics of the optical dipole trap, which is used to store a single ^{87}Rb atom. Due to the small trap size, a blockade mechanism occurs, limiting the maximum number of trapped atoms to one. Measuring the second order correlation function of the fluorescence light verified the presence of a single atom in the trap, and from the measured spectrum of resonance fluorescence we determined the temperature of the trapped atom. In the fourth chapter the detection process of the internal atomic states is described in detail, where we use a combination of a darkstate projection and the STIRAP technique to transfer well defined superposition states from the $F = 1$ to the $F = 2$ atomic hyperfine ground level. Together with a hyperfine level detection scheme this allows to analyze the internal atomic states in arbitrary measurement bases. Finally, chapter five describes the generation of the entangled atom-photon state in the spontaneous decay. Application of the atomic state detection scheme together with a polarization measurement of the emitted photon allows to perform correlation measurements as well as a complete state tomography of the entangled atom-photon state. The experimental results show a high degree of entanglement between the atom and the emitted photon. The last chapter summarizes our experimental results and discusses possible applications of the entangled atom-photon state.

2. Theory of atom-photon entanglement

Contents

The main goal of this thesis is the generation of an entangled state between the angular momentum of a single atom and the polarization of a single photon emitted in the spontaneous decay. Therefore, the following chapter gives a short introduction into entanglement by means of qubit states. Implications of entanglement for the EPR paradox and Bell's inequality are discussed and two basic applications of entangled states are presented. The second part of this chapter describes the spontaneous decay process and the generation of atom-photon entanglement in a decay in a Λ-type atomic system. Finally, the dependence of the entangled atom-photon state on the collection efficiency of the emitted photons is analyzed for our experimental parameters.

2.1. Entanglement and Bell's inequality

This section shortly describes the quantum mechanical properties of spin-1/2 (qubit) systems and entangled states consisting of two qubits. Afterwards, the EPR paradox is discussed and a derivation of Bell's inequality is presented, that shows that the predictions of certain

measurement outcomes of quantum mechanics do not agree with the predictions from theories based on the assumption of local realism. Finally, two basic applications of entangled states – namely quantum teleportation and entanglement swapping – are introduced.

2.1.1. Spin-1/2 system

The most basic, non-trivial quantum mechanical system is the spin-1/2 or qubit state, which is the quantum mechanical analog of a classical bit. In contrast to classical mechanics, the spin-1/2 system can not only be in the states $|\uparrow\rangle$ and $|\downarrow\rangle$, but also a superposition of these two basis states is allowed and therefore the general qubit state is given by

$$|\Psi\rangle = \alpha\,|\uparrow\rangle + \beta\,|\downarrow\rangle\,. \tag{2.1}$$

The coefficients α and β are complex numbers, where the possibility to obtain the result $|\downarrow\rangle$ and $|\uparrow\rangle$ in a measurement is given by $|\alpha|^2$ and $|\beta|^2$, respectively and the normalization condition requires $|\alpha|^2 + |\beta|^2 = 1$. Because the global phase of the state is irrelevant, we can describe the qubit by

$$|\Psi\rangle = \cos\frac{\theta}{2}\,|\uparrow\rangle + e^{i\phi}\sin\frac{\theta}{2}\,|\downarrow\rangle \tag{2.2}$$

with the real parameters θ and ϕ. According to this definition, every qubit can be represented as a point on the surface of the so called Bloch-sphere (Fig. 2.1), given by the spherical angles θ and ϕ.

In principle, every quantum mechanical system with two degrees of freedom can be described as a qubit state. Examples are the polarization of a photon or the state of a spin-1/2 particle, where the basis-vectors $|\uparrow\rangle$ and $|\downarrow\rangle$ directly correspond to the two possible spin orientations along a given axis.

Quantum mechanical measurements

In quantum mechanics, measurements are described by Hermitian operators $\hat{A}$. In a measurement the unknown state $|\Psi\rangle$ is projected onto the eigenstates of $\hat{A}$, whereby the possible measurement outcomes are given by the corresponding eigenvalues. The expectation value of a measurement outcome is given by $\langle\hat{A}\rangle = \langle\Psi|\hat{A}|\Psi\rangle$. For spin-1/2 systems, the Pauli-matrices

$$\hat{\sigma}_x = \begin{pmatrix} 0 & 1 \\ 1 & 0 \end{pmatrix}, \qquad \hat{\sigma}_y = \begin{pmatrix} 0 & i \\ -i & 0 \end{pmatrix}, \text{ and } \hat{\sigma}_z = \begin{pmatrix} 1 & 0 \\ 0 & -1 \end{pmatrix} \tag{2.3}$$

form a complete set of complementary operators with the eigenvalues ± 1 and the corresponding eigenstates

$$|\uparrow\rangle_x = \frac{1}{\sqrt{2}}\left(|\downarrow\rangle_z + |\uparrow\rangle_z\right), \tag{2.4}$$

$$|\downarrow\rangle_x = \frac{1}{\sqrt{2}}\left(|\downarrow\rangle_z - |\uparrow\rangle_z\right), \tag{2.5}$$

$$|\uparrow\rangle_y = \frac{1}{\sqrt{2}}\left(i\,|\downarrow\rangle_z + |\uparrow\rangle_z\right), \tag{2.6}$$

$$|\downarrow\rangle_y = \frac{1}{\sqrt{2}}\left(|\downarrow\rangle_z + i\,|\uparrow\rangle_z\right), \tag{2.7}$$
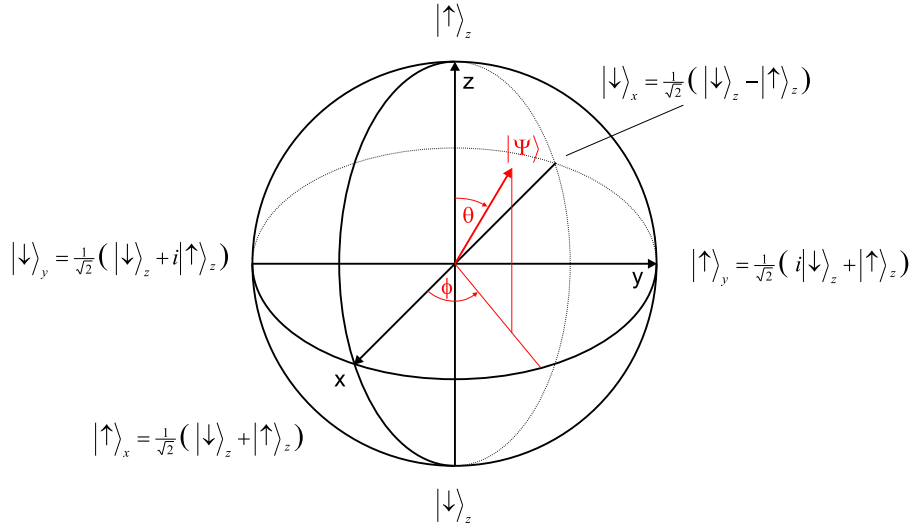
Figure 2.1.: Representation of the qubit states on the Bloch sphere. Any possible state $|\Psi\rangle$ of a single qubit can be represented as a point on the surface of the sphere, defined by the spherical angles θ and ϕ.

$|\uparrow\rangle_z$ and $|\downarrow\rangle_z$. Figure 2.1 shows the representation of these states on the Bloch-sphere. The three measurement bases $\hat{\sigma}_x$, $\hat{\sigma}_y$ and $\hat{\sigma}_z$ are complementary, i.e., measuring a physical system prepared in a certain eigenstate in a complementary basis yields a maximum uncertainty of the measurement outcome, i.e. the result is completely random.

2.1.2. Entanglement

If we consider quantum states consisting of more than one particle, there exists a certain class of states, where the combined two-particle system $|\Psi\rangle$ can not be described as tensor product of single particle states $|\Psi\rangle_a$ and $|\Psi\rangle_b$:

$$|\Psi\rangle \neq |\Psi\rangle_a \otimes |\Psi\rangle_b. \tag{2.8}$$

These systems are called entangled (in contrast to separable states) and have the interesting physical property, that while the combined two-particle state can be a well defined quantum state, this is not the case if we consider only the single particles for themself.

Bell states

A quantum system consisting of two qubits defines a four dimensional Hilbert space. In analogy to the preceding section a possible basis is defined by the four separable product states $|\uparrow\rangle_z |\uparrow\rangle_z$,

$|\uparrow\rangle_z |\downarrow\rangle_z$, $|\downarrow\rangle_z |\uparrow\rangle_z$ and $|\downarrow\rangle_z |\downarrow\rangle_z$. A different basis can be defined by four maximally entangled states:

$$\left|\Psi^-\right\rangle = \frac{1}{\sqrt{2}} \left(|\uparrow\rangle_z |\downarrow\rangle_z - |\downarrow\rangle_z |\uparrow\rangle_z \right) \tag{2.9}$$

$$\left|\Psi^+\right\rangle = \frac{1}{\sqrt{2}} \left(|\uparrow\rangle_z |\downarrow\rangle_z + |\downarrow\rangle_z |\uparrow\rangle_z \right) \tag{2.10}$$

$$\left|\Phi^-\right\rangle = \frac{1}{\sqrt{2}} \left(|\uparrow\rangle_z |\uparrow\rangle_z - |\downarrow\rangle_z |\downarrow\rangle_z \right) \tag{2.11}$$

$$\left|\Phi^+\right\rangle = \frac{1}{\sqrt{2}} \left(|\uparrow\rangle_z |\uparrow\rangle_z + |\downarrow\rangle_z |\downarrow\rangle_z \right). \tag{2.12}$$

These states are often named Bell states [53], where $|\Psi^-\rangle$ is the antisymmetic singlet state and the other three entangled states correspond to the symmetric triplet states. Using the definitions in eqns (2.4)-(2.7) we can describe e.g the $|\Psi^+\rangle$ state in the complementary bases $\hat{\sigma}_x$ and $\hat{\sigma}_y$:

$$\left|\Psi^+\right\rangle = \frac{1}{\sqrt{2}} \left(|\downarrow\rangle_x |\downarrow\rangle_x + |\uparrow\rangle_x |\uparrow\rangle_x \right) \tag{2.13}$$

$$= \frac{1}{\sqrt{2}} \left(|\downarrow\rangle_y |\downarrow\rangle_y - |\uparrow\rangle_y |\uparrow\rangle_y \right). \tag{2.14}$$

This transformation shows the main properties of entangled states. On the one hand, it is not possible to find a basis in which the state is separable, i.e. an entangled state is entangled in any measurement basis. Furthermore, the outcome of a state-measurement on one of the two particles of the above states is completely random for every measurement basis. But on the other hand, perfect measurement correlations are present: If we measure the state of one particle, we will instantly know the state of the second particle with probability one.

This high degree of correlations present in entangled states is at the heart of quantum mechanics and raised many questions about the physical description of reality that lead to the EPR paradox and Bell's inequality.

2.1.3. EPR paradox

In 1935, Einstein, Podolsky and Rosen (EPR) published an article in which they raised the question, *"Can quantum-mechanical description of physical reality be considered complete ?"* [1]. In this work, they made three basic assumptions, that should – according to their opinion – be fulfilled by any physical theory:

1. **Completeness:** *"Every element of physical reality must have a counterpart in the physical theory."*

2. **Realism:** *"If, without in any way disturbing a system, we can predict with certainty (i.e., with probability one) the value of a physical quantity, then there exists an element of reality corresponding to this physical quantity."*

3. **Locality:** Physical systems can be separated such (e.g. due to large distance), that their interaction can be neglected.

They proposed a Gedankenexperiment using two particles entangled in their momentum and position degree of freedom. The particles are separated far enough from each other to assure the assumption of locality. By a position measurement of particle 1 one can according to quantum mechanics predict with certainty the position measurement outcome of particle 2. Therefore, this position is an element of physical reality. In the same way one can conclude that also the momentum of this particle is an element of reality, which contradicts the uncertainty principle. Therefore, EPR conclude that quantum mechanics is not complete and a more fundamental theory should exist, fulfilling their three assumptions. In order to extend quantum theory to form a complete local realistic theory, typically so-called local hidden variables (LHV) are introduced, which according to EPR are elements of reality necessary for a full description of the physical system.

Bohr [54] replied to the conclusion obtained from EPR, that the definition of an element of reality can not be made without considering the experimental apparatus. Since EPR consider measurements of complementary observables, in principle two different (complementary) measurement setups would be required to obtain information about their values. Thus, it is not justified to speak of the simultaneous reality of the complementary degrees of freedom and therefore he rejects their conclusion that quantum mechanics is incomplete. Schrödinger summarized these results in his article *"The present situation of quantum mechanics"* [55], in which he also first introduced the term entanglement (Verschränkung).

The original argument of EPR was based on entanglement between position and momentum degree of freedom. This is mathematically complicated due to the infinite dimensions of the corresponding Hilbert space. An easier mathemtical formalism of the above Gedankenexperiment was derived by Bohm [3], who considered the case of two entangled spin-1/2 particles, initially prepared in the state $|\Psi^-\rangle$ by the decay of a spin-0 system. This allowed a much simpler mathematical description of the problem and allowed Bell to derive his inequality [2].

2.1.4. Bell's inequality

The problem introduced by EPR was somehow of philosophical nature, because no measureable contradiction between a possible local-realistic description of reality and quantum mechanics was assumed. However, in 1964 Bell [2] was able to show that the predictions of local realistic theories for the expectation values of certain measurement outcomes are not compatible with the quantum mechanical description. The following chapter gives a more generalized derivation of his argument, that does not rely on perfect correlations and was derived by CHSH [4] and generalized by Bell [5].

In our consideration we assume a source emitting entangled pairs of qubits in the state $|\Psi^-\rangle$. From each pair, one particle is sent to observer A and one to observer B. They performe spin measurements on their particle in one of the two measurement bases defined by the vectors $\mathbf{a}$ and $\mathbf{a}'$ and $\mathbf{b}$ and $\mathbf{b}'$, respectively (see Fig. 2.2). According to quantum mechanics the possible measurement outcomes are the states $|\uparrow\rangle$ and $|\downarrow\rangle$, that we assign the values $+1$ and -1, respectively.
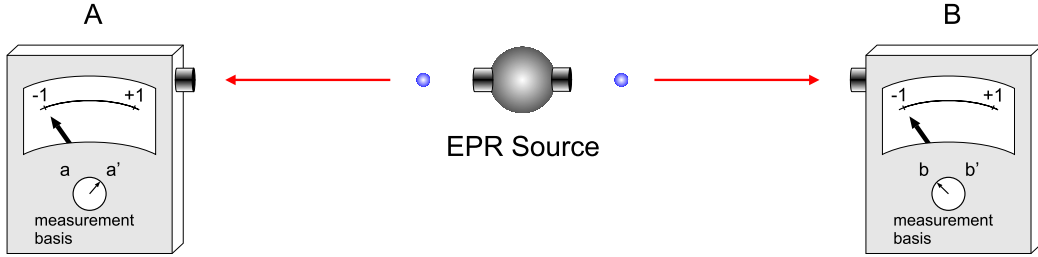
Figure 2.2.: Typical experiment to test Bell's inequality. An EPR source generates pairs of entangled particles in the state $|\Psi^-\rangle$. From each pair, one particle is send to observer A and B, respectively. The observers perform a spin measurement on their particle along the measurement directions $\mathbf{a}$, $\mathbf{a}'$ and $\mathbf{b}$, $\mathbf{b}'$, with the possible measurement results ± 1.

Local realistic description

In local realistic theories, all measurement outcomes are determined by a set of unknown local hidden variables λ. According to these theories, the probabilistic nature of measurements in quantum mechanics is due to the fact, that even for identically prepared particles, the corresponding hidden variables are in an unknown statistically distribution $p(\lambda)$ of possible values λ. The normalization condition of the probabilities requires

$$\int_\Lambda p(\lambda)d\lambda = 1. \tag{2.15}$$

The observables $A_{\mathbf{a}}(\lambda) = \pm 1$ and $B_{\mathbf{b}}(\lambda) = \pm 1$ describe the single measurement outcome for observer A and B, respectively. These outcomes are only determined by the value of the hidden variables λ and the analyzer setting $\mathbf{a}$, $\mathbf{a}'$ and $\mathbf{b}$, $\mathbf{b}'$ (reality) and not by the analyzer setting of the other observer (locality). Therefore, the expectation value of the joint measurement $A_{\mathbf{a}}(\lambda) \cdot B_{\mathbf{b}}(\lambda)$ is given by

$$E(\mathbf{a}, \mathbf{b}) = \int_\Lambda A_{\mathbf{a}}(\lambda)B_{\mathbf{b}}(\lambda)p(\lambda)d\lambda. \tag{2.16}$$

Introducing an alternative analyzer setting $\mathbf{a}'$ and $\mathbf{b}'$ we get

$$E(\mathbf{a}, \mathbf{b}) - E(\mathbf{a}, \mathbf{b}') = \int_\Lambda \left[A_{\mathbf{a}}(\lambda)B_{\mathbf{b}}(\lambda) - A_{\mathbf{a}}(\lambda)B_{\mathbf{b}'}(\lambda) \right] p(\lambda)d\lambda, \tag{2.17}$$

that can be rewritten as

$$
\begin{aligned}
E(\mathbf{a}, \mathbf{b}) - E(\mathbf{a}, \mathbf{b}') = {} & \int_\Lambda A_{\mathbf{a}}(\lambda)B_{\mathbf{b}}(\lambda) \left[1 \pm A_{\mathbf{a}'}(\lambda)B_{\mathbf{b}'}(\lambda) \right] p(\lambda)d\lambda - \\
& \int_\Lambda A_{\mathbf{a}}(\lambda)B_{\mathbf{b}'}(\lambda) \left[1 \pm A_{\mathbf{a}'}(\lambda)B_{\mathbf{b}}(\lambda) \right] p(\lambda)d\lambda.
\end{aligned}
\tag{2.18}
$$

Because the measurement outcomes have the possible values ± 1, the observables are bound by $|A_{\mathbf{a}}(\lambda)| \leq 1$ and $|B_{\mathbf{b}}(\lambda)| \leq 1$ and one obtains from eqn (2.18):

$$|E(\mathbf{a}, \mathbf{b}) - E(\mathbf{a}, \mathbf{b}')| \leq \int_{\Lambda} \left[1 \pm A_{\mathbf{a}'}(\lambda) B_{\mathbf{b}'}(\lambda)\right] p(\lambda) d\lambda + \int_{\Lambda} \left[1 \pm A_{\mathbf{a}'}(\lambda) B_{\mathbf{b}}(\lambda)\right] p(\lambda) d\lambda, \quad (2.19)$$

that yields

$$S(\mathbf{a}, \mathbf{a}', \mathbf{b}, \mathbf{b}') = |E(\mathbf{a}, \mathbf{b}) - E(\mathbf{a}, \mathbf{b}')| + |E(\mathbf{a}', \mathbf{b}) + E(\mathbf{a}', \mathbf{b}')| \leq 2. \quad (2.20)$$

Equation (2.20) is the CHSH-representation of Bell's inequality. In its derivation we only used EPR's basic assumptions of locality and reality and therefore eqn (2.20) must be satisfied for any theory based on local hidden variables. In order to show the contradictions between quantum mechanics and local realistic theories, we have to evaluate the expectation value of the spin-correlations function $S(\mathbf{a}, \mathbf{a}', \mathbf{b}, \mathbf{b}')$ for the quantum mechanical case.

Quantum mechanical description

In quantum mechanics, the spin measurement of particle 1 and 2 along the direction $\mathbf{a}$ and $\mathbf{b}$ is defined by the observables

$$\hat{A}_{\mathbf{a}} = \hat{\sigma}_{\mathbf{a}} = (\hat{\sigma}_x, \hat{\sigma}_y, \hat{\sigma}_z) \cdot \mathbf{a} \qquad \text{and} \qquad (2.21)$$

$$\hat{B}_{\mathbf{b}} = \hat{\sigma}_{\mathbf{b}} = (\hat{\sigma}_x, \hat{\sigma}_y, \hat{\sigma}_z) \cdot \mathbf{b}, \qquad (2.22)$$

respectively. If we perform a joint spin measurement on the state $|\Psi^-\rangle$, the expectation value is

$$\begin{aligned} E_{qm}(\mathbf{a}, \mathbf{b}) &= \langle \hat{A}_{\mathbf{a}} \cdot \hat{B}_{\mathbf{b}} \rangle = \langle \Psi^- | \sigma_{\mathbf{a}} \otimes \sigma_{\mathbf{b}} | \Psi^- \rangle \\ &= -\mathbf{ab}. \end{aligned} \qquad (2.23)$$

Using the analyzer setting, where all vectors $\mathbf{a}$, $\mathbf{b}$, $\mathbf{a}'$ and $\mathbf{b}'$ lie in one plane and inclose the angles $\angle(\mathbf{ab}) = \angle(\mathbf{ba}') = \angle(\mathbf{a}'\mathbf{b}') = 45°$, one can derive the quantum mechanical expectation value of S_{qm}, that is given by

$$S_{qm}(\mathbf{a}, \mathbf{a}', \mathbf{b}, \mathbf{b}') = 2\sqrt{2} > 2, \qquad (2.24)$$

which clearly violates the CHSH inequality. Hence, the description of EPR's Gedankenexperiment by theories based on local hidden variables contradicts the quantum mechanical prediction. Therefore, a local realistic extension of quantum mechanics is not possible.

Loopholes

Equation (2.20) provides an experimentally testable quantity that allows to determine whether nature can be described by local realistic theories or not. However, the observation of a violation of eqn (2.20) does not necessarily rule out all local realistic theories. In (up to date) all experimental tests of Bell's inequality some additional assumptions concerning the detected particles had to be made, opening loopholes for a local realistic description. In general there are two main loopholes:

1. Detection loophole: In most real experiments only a certain subset of the generated entangled particles is detected (due to e.g. limited detection or collection efficiency). Even if the measured pair events violate Bell's inequality, there exists still the possibility, that the whole ensemble (including the undetected particles) does not. Therefore, one has to rely on the assumption, that the detected particles are in a representative subset of the whole ensemble (fair sampling).

2. Locality loophole: For the derivation of Bell's inequality one has to assume, that the measurement result of particle one is independent of the analyzer setting of observer two (locality), which introduces another loophole. In order to rule out any possible local realistic description, the only way to ensure this condition is to assume that no interaction faster than the speed of light is possible, so the independence of the two measurement outcomes can be achieved by a space-like separation of the two particles with respect to their measurement time.

Until now, many experiments have been performed analyzing the violation of Bell's inequality. The first experiments used the cascade decay in calcium for the generation of polarization entangled photon pairs [7, 8] and showed a violation of the CH-inequality [6]. Later on, Aspect et al. improved these experiments [9] and introduced two channel polarizers [10] that allowed the direct measurement of the expectation values $E(\mathbf{a}, \mathbf{b})$ in a single run. Furthermore, they addressed for the first time the problem of the locality loophole by using acousto-optical modulators for a fast switching of the measurement bases [11]. The occurrence of parametric-down conversion [56, 57, 58] greatly simplified the generation of entangled photon pairs. This lead to the first experimental violation of Bell's inequality under strict locality conditions [14], that allowed to close the locality loophole.

In all these experiments the detection efficiency of the photons was low, thus the experimental outcomes had to rely on the fair sampling assumption. In an experiment using a pair of entangled trapped ions it was possible for the first time to close the detection loophole [17]. The ion state detection was performed by scattering light from the atom. Therefore, a high detection efficiency was achieved and no fair sampling assumption had to be made. However, due to the small distance of a few μm between the entangled ions, the locality loophole remained. Until now, no experiment has been performed, that closed the detection and the locality loophole at the same time. Thus, a local realistic description of physical reality is not completely ruled out and a final test of Bell's inequality still has to be performed.

2.1.5. Application of entanglement

Entanglement of quantum systems is not only interesting from a fundamental point of view, but it is also the basic ingredient for quantum communication and information applications [24, 23]. The following section gives a short introduction into two basic applications namely quantum teleportation [32, 33] allowing the distribution of arbitrary quantum states, and entanglement swapping [34] that can be used for the generation of entanglement between remote systems.
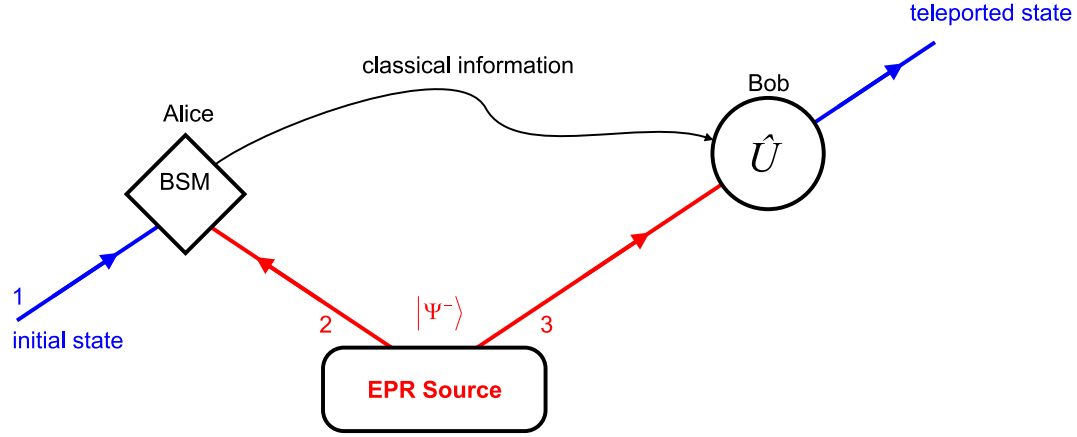
Figure 2.3.: Simplified scheme of the quantum teleportation protocoll. The initial particle (1) that should be teleported and one particle from an entangled state are sent to Alice. She performs a Bell state measurement (BSM) on the combined state. Depending on her measurement outcome, Bob has to perform one out of four unitary transformation, to reconstruct the initial state of particle 1.

Quantum Teleportation

The main idea of the quantum teleportation protocol [32, 33] is the transfer of an unknown quantum state of a given particle (see eqn (2.1)) from Alice to a remote location (Bob) without directly sending the particle itself. Measuring the unknown state of Alice's particle and sending the result to Bob is not possible, because according to the projection postulate of quantum mechanics, the measurement will destroy the quantum state without revealing all necessary information for its reconstruction. To overcome this problem, we assume, that Alice and Bob share the entangled state $|\Psi^-\rangle$ (see Fig. 2.3). If we label the initial particle by 1 and the two particles of the entangled state by 2 and 3 the combined three photon state can be written as

$$
\begin{aligned}
|\Psi\rangle_{123} = |\Psi\rangle_1 \otimes |\Psi^-\rangle_{23} \;=\; \frac{1}{2}\big[& |\Psi^-\rangle_{12}\left(-\alpha|\uparrow\rangle_3 - \beta|\downarrow\rangle_3\right) \\
& + |\Psi^+\rangle_{12}\left(-\alpha|\uparrow\rangle_3 + \beta|\downarrow\rangle_3\right) \\
& + |\Phi^-\rangle_{12}\left(+\beta|\uparrow\rangle_3 + \alpha|\downarrow\rangle_3\right) \\
& + |\Phi^+\rangle_{12}\left(-\beta|\uparrow\rangle_3 + \alpha|\downarrow\rangle_3\right) \big].
\end{aligned}
\tag{2.25}
$$

Alice now performs a measurement on the particles 1 and 2 in the Bell basis. Depending on her measurement outcome, particle 3 will be in one of the four possible states given in eqn (2.25). For example, if Alice measures the state $|\Psi^-\rangle_{12}$, particle 3 will (up to a global phase) be in the
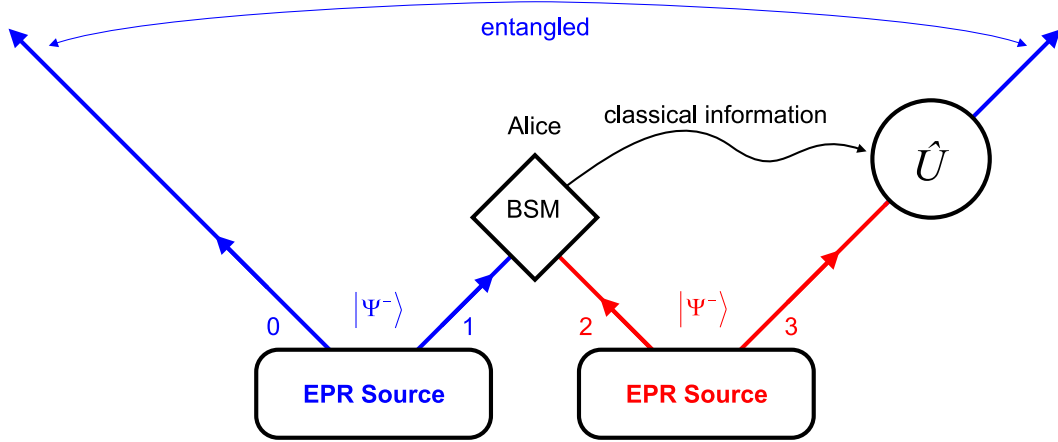
Figure 2.4.: Entanglement swapping scheme. Alice performs a Bell state measurement (BSM) on the two particles 1 and 2, that emerge from two different entangled states. After her measurement the particles 0 and 3, which can be at arbitrary distances, are entangled.

same quantum state as the initial particle 1. In the other cases Bob has to perform one out of three unitary transformation on his particle to reconstruct the original state. The information, which unitary transformation has to be performed is obtained from the result of Alice's Bell state measurement and sent to Bob. Thus, by sending two bits of classical information from Alice to Bob it is possible to realize the full transfer of an unknown quantum state onto a remote particle.

Entanglement swapping

An interesting extension of quantum teleportation is the entanglement swapping protocoll [34]. In this process, the initial particle 1 is now itself part of an entangled state. If we assume, that the particle initially emerges from the entangled state $|\Psi^-\rangle_{01}$ (see Fig. 2.4), the combined 4-particle system can be written as:

$$
\begin{aligned}
|\Psi\rangle_{0123} &= |\Psi^-\rangle_{01} \otimes |\Psi^-\rangle_{23} \\
&= \frac{1}{2} \big(|\Psi^+\rangle_{03} \otimes |\Psi^+\rangle_{12} - |\Psi^-\rangle_{03} \otimes |\Psi^-\rangle_{12} \\
&\quad - |\Phi^+\rangle_{03} \otimes |\Phi^+\rangle_{12} + |\Phi^-\rangle_{03} \otimes |\Phi^-\rangle_{12} \big).
\end{aligned}
\tag{2.26}
$$

If now Alice performs a Bell-state measurement on her particles 1 and 2, the remaining two particle 0 and 3 will be in one of the four entangled Bell states given by eqns (2.9-2.12), depending on Alice's measurement outcome. Using the same unitary operations as in the teleportation

protocol, the final entangled state $|\Psi_{03}\rangle$ is equal to the initial state $|\Psi_{01}\rangle$. In principle, the entanglement of the initial pair was teleported onto the final quantum state $|\Psi_{03}\rangle$. This scheme is important for many quantum communication applications, because it allows to entangle particles at arbitrary distance without the necessity of a direct interaction.

2.2. Generation of atom-photon entanglement

Entanglement is important for the analysis of fundamental physical questions about the nature of physical reality. Furthermore, it forms the main resource for many quantum information and quantum communication applications. Especially entanglement between different species as e.g. atoms and photons is important because it allows to form the interface between photonic quantum communication channels and atomic quantum memories [46, 43, 45, 41].

In our experiment, we generate an entangled state between a single ^{87}Rb atom and a single photon emitted in the spontaneous decay. Conservation of angular momentum thereby generates entanglement between the polarization of the emitted photon and the angular momentum of the atom. Therefore, this chapter gives a short introduction into the physics of spontaneous decay and the generation of entanglement in the case of multiple decay channels. In the last part, the dependence of the fidelity of the entangled atom-photon state on the collection efficiency of the spontaneously emitted photons is analyzed.

2.2.1. Spontaneous decay

In quantum theory of the electromagnetic field, the interaction of an atom in an excited state with the different radiation field modes of the vacuum state, i.e. the state with no excitations (photons), gives rise to the spontaneous decay of the atom, accompanied by the emission of a single photon into one of the vacuum modes. In most experiments, one is only interested in the state of the atom and the photonic degrees of freedom are ignored. Thus, the spontaneous emission gives rise to decoherence in the atomic system. Nonetheless, the combined atom-field system can be in an (entangled) coherent superposition state.

Decay in a two-level system

In order to calculate the properties of spontaneous emission, we consider a two-level atom (transition frequency ω_0) with the ground and excited states $|e\rangle$ and $|g\rangle$ interacting with the vacuum field. The Hamiltonian describing the interaction with the vacuum is given in the rotating wave approximation by (see chapter A.1)

$$\hat{H}_{ED} = i\hbar \sum_{\lambda,\mathbf{k}} \left(g_{\lambda\mathbf{k}}\hat{\pi}^{\dagger}\hat{a}_{\lambda\mathbf{k}}e^{-i(\omega_0-\omega_k)t} - g_{\lambda\mathbf{k}}^{*}\hat{\pi}\hat{a}_{\lambda\mathbf{k}}^{\dagger}e^{+i(\omega_0-\omega_k)t} \right), \tag{2.27}$$

where $\hat{a}^{\dagger}$ and $\hat{a}$ describe the creation and annihilation of a photon in the mode $\lambda\mathbf{k}$ with the two polarization states $\lambda = 1, 2$ and the wave vector $\mathbf{k}$. The operators $\hat{\pi}^{\dagger}$ and $\hat{\pi}$ describe the excitation and deexcitation of the atom, respectively. The coupling strength between the light

field and the atom is given by $g_{\lambda\mathbf{k}}$. The combined atom-field state is described by the state vector

$$|\Psi\rangle = c_e(t)\,|e\rangle\,|0\rangle + \sum_{\lambda,\mathbf{k}} c_{g,\lambda\mathbf{k}}(t)\,|g\rangle\,|1_{\lambda\mathbf{k}}\rangle\,, \tag{2.28}$$

where $c_e(t)$ is the amplitude of the excited state and $c_{g\lambda\mathbf{k}}(t)$ describes the amplitude of the combined state consisting of the atom in the ground state and a photon in the mode $\lambda\mathbf{k}$. The initial conditions are $c_e(0) = 1$ and $c_{g,\lambda\mathbf{k}}(0) = 0$ (atom in the excited state). From the Schrödinger equation of the system

$$\frac{\partial}{\partial t}\,|\Psi(t)\rangle = -\frac{i}{\hbar}\hat{H}_{ED}\,|\Psi(t)\rangle \tag{2.29}$$

one obtains the approximate evolution of the excited state amplitude [59]

$$\dot{c}_e(t) = -\frac{|d_{eg}|^2}{6\pi^2\epsilon_0\hbar c^3}\int_0^\infty d\omega_k\omega_k^3\int_0^t dt'\,e^{i(\omega_0-\omega_k)(t-t')}c_e(t'), \tag{2.30}$$

with the electric dipole matrix element $d_{eg} = \langle e|\hat{\mathbf{d}}|g\rangle$. From this equation one approximately obtains

$$\dot{c}_e(t) = -\frac{\Gamma}{2}c_e(t) \tag{2.31}$$

with the spontaneous decay rate

$$\Gamma = \frac{|d_{eg}|^2\omega_0^3}{3\pi\epsilon_0\hbar c^3}. \tag{2.32}$$

This equation describes the well known exponential decay of the excited state population $|c_e(t)|^2 = \exp(-\Gamma t)$ with the atomic lifetime $\tau = 1/\Gamma$. The combined atom-photon state in the limit $t \to \infty$ is given by

$$|\Psi(\infty)\rangle = |g\rangle \sum_{\lambda\mathbf{k}} g_{\lambda\mathbf{k}} e^{-i\mathbf{k}\mathbf{r}} \frac{1}{(\omega_k - \omega_0) + i\Gamma/2}\,|1_{\lambda\mathbf{k}}\rangle\,, \tag{2.33}$$

where the atom (located at $\mathbf{r} = 0$) fully decayed into the ground state $|g\rangle$ and a single photon was emitted. This state is a linear superposition of single photon states with different wavevectors $\mathbf{k}$. From the state vector $|\Psi(t)\rangle$ one can obtain the probability to detect the photon at time t at the position $\mathbf{r}$, which is given by the expression [59]

$$p_{det}(\mathbf{r},t) = \langle\psi_F|\,\mathbf{E}^-(\mathbf{r},t)\mathbf{E}^+(\mathbf{r},t)\,|\psi_F\rangle = \frac{|E_0|^2}{r^2}\Theta\left(t - \frac{r}{c}\right)e^{-\Gamma(t-r/c)} \tag{2.34}$$

where Θ is the unit step function and

$$E_0 = -\frac{\omega^2 d_{eg}\sin\eta}{4\pi\epsilon_0 c^2 r} \tag{2.35}$$

with the angle η between the observation direction $\mathbf{r}$ and the atomic dipole $\hat{\mathbf{d}}$. For $t = r/c$ (which defines the 'wavefront' of the emitted light field), eqn (2.34) gives the highest detection probability of the photon. For $t > r/c$ the detection probability drops exponentially with the atomic decay rate Γ.
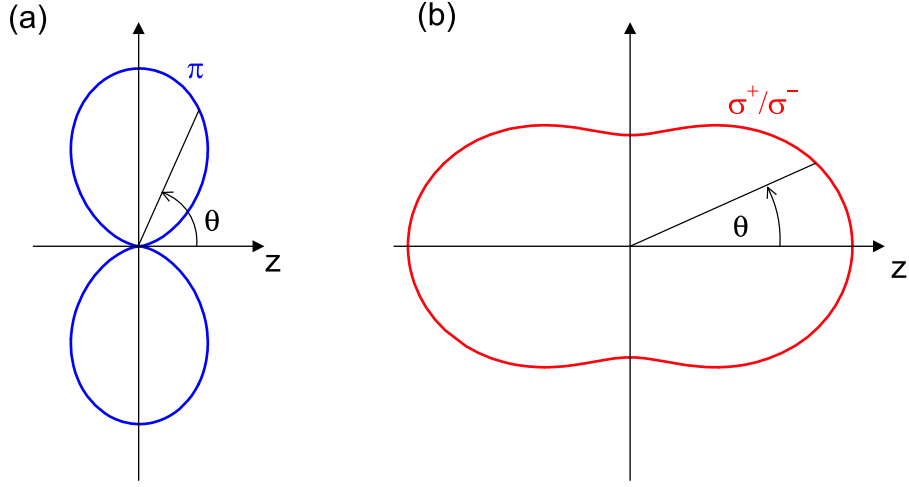
Figure 2.5.: Emission characteristics of (a) π- and (b) $\sigma^{\pm}$-polarized light. According to the transverse nature of electromagnetic radiation, π-polarized light can not be emitted along the direction $\theta = 0$.

2.2.2. Definition of the polarization modes

In general, an excited atomic state has multiple decay channels leading to different atomic ground states. The initial excited state as well as the final atomic ground states have well defined angular momenta. Therefore, conservation of angular momentum requires, that the spin of the emitted photon also is in a defined state. If we define a quantization axis for our system, we can decompose the angular momentum degrees of freedom of the atom and the photon into the eigenstates of this system. For the photon this decomposition yields the three states

$$
\begin{align}
|m = +1\rangle &= |\sigma^{+}\rangle \tag{2.36} \\
|m = 0\rangle &= |\pi\rangle \tag{2.37} \\
|m = -1\rangle &= |\sigma^{-}\rangle, \tag{2.38}
\end{align}
$$

where m defines the projection of the photonic spin on the quantization axis. The three spin eigenstates $|\sigma^{+}\rangle$, $|\pi\rangle$ and $|\sigma^{-}\rangle$ correspond to left circularly, linearly (parallel to the quantization axis) and right circularly polarized light (see chapter A.3). Since electromagnetic radiation is a transverse oscillating wave, the spatial modes of π- and $\sigma^{\pm}$-polarized light differ from each other (Fig. 2.5). The emission probability into the spatial mode is given by the emission

characteristics of dipole radiation [60]. Therefrom we obtain the three polarization modes

$$\left|\Sigma^{\pm}\right\rangle \quad = \quad \sqrt{\tfrac{3}{16\pi}}\sqrt{(1+\cos^2\theta)} \cdot \left|\sigma^{\pm}\right\rangle \otimes \sum_{\theta,\omega} g_\omega \left|\theta,\omega\right\rangle, \qquad (2.39)$$

$$\left|\Pi\right\rangle \quad = \quad \sqrt{\tfrac{3}{8\pi}}\sin\theta \cdot \left|\pi\right\rangle \otimes \sum_{\theta,\omega} g_\omega \left|\theta,\omega\right\rangle, \qquad (2.40)$$

where θ is the angle relative to the quantization axis and the first ket on the right hand side defines the polarization state and the second ket describes the spatial and frequency mode. According to eqns (2.39) and (2.40), π-polarized photons are not emitted along the quantization axis, whereas the emission of $\sigma^{\pm}$-polarized photons reaches its maximum probability along this direction.

2.2.3. Spontaneous decay in multilevel systems
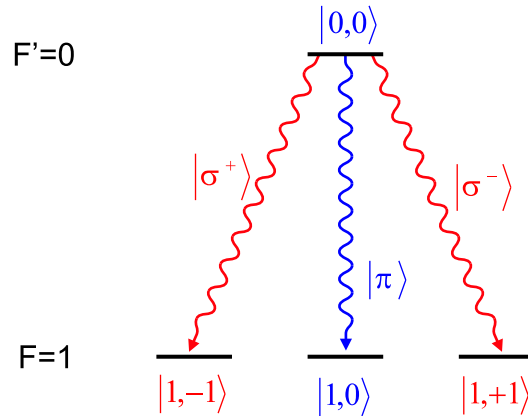
Figure 2.6.: Spontaneous decay of a single ^{87}Rb atom from the excited state $\left|0,0\right\rangle$ with angular momentum zero to the three possible ground states $\left|1,\pm 1\right\rangle$ and $\left|1,0\right\rangle$ with total angular momentum one and its projections $m_F = 0,\pm 1$ on the quantization axis.

Next we include the conservation of angular momentum in our consideration of the spontaneous decay. Suppose we have an atom in the excited state, with zero angular momentum. After spontaneous emission the atom is in the ground state with angular momentum $F = 1$

(see Fig. 2.6). In analogy to section 2.2.1 we obtain for the final state of the atom-light system

$$
\begin{aligned}
|\Psi(\infty)\rangle &= \tfrac{1}{\sqrt{3}} \left(\left|\Sigma^+\right\rangle |1,-1\rangle + |\Pi\rangle |1,0\rangle + \left|\Sigma^-\right\rangle |1,+1\rangle \right) \\
&= \sqrt{\tfrac{1}{8\pi}} \left[\sqrt{\tfrac{1}{2}(1+\cos^2\theta)} \left(\left|\sigma^+\right\rangle |1,-1\rangle + \left|\sigma^-\right\rangle |1,+1\rangle \right) + \sin\theta \, |\pi\rangle |1,0\rangle \right] \\
&\quad \otimes \sum_{\theta,\omega} g_\omega |\theta,\omega\rangle ,
\end{aligned} \tag{2.41}
$$

where, the three atomic ground states are labeled by $|1,\pm 1\rangle$ and $|1,0\rangle$. The first number in the kets describes the total angular momentum F of the state and the second number defines the projection m_F of the angular momentum on the quantization axis. The full atom-radiation state described by eqn (2.41) is a well defined quantum state, where the angular momenta of the atom and the photon are entangled. The phase relation of the different components of eqn (2.41) can be obtained from the Clebsch-Gordan coefficients of the involved angular momenta[1].

Equation (2.41) describes an entangled spin-1 state. However, the transverse nature of light makes the observation of the full state impossible. On the other hand, if the system is only analyzed along the quantization axis, the state in eqn (2.41) reduces to the entangled qubit state

$$
|\Psi\rangle = \frac{1}{\sqrt{2}} \left(\left|\sigma^+\right\rangle |1,-1\rangle + \left|\sigma^-\right\rangle |1,+1\rangle \right) . \tag{2.42}
$$

The selection of a single emission direction, thus allows the generation of a maximally entangled qubit state.

2.2.4. Experimental realization

For the experimental realization of atom-photon entanglement on needs a single localized atom, isolated from the environment. Therefore, we use a single ^{87}Rb atom stored in an optical dipole trap. In the decay of the $F' = 0$ hyperfine level of the excited state $5^2P_{3/2}$ to the ground state hyperfine level $5^2S_{1/2}$, $F = 1$, the entangled state defined by eqn (2.41) is generated. In order to collect the emitted photons, we use a microscope objective, where the optical axis of the collection optics defines the quantization axis of our system. Thus, the photons collected by the objective are in the entangled qubit state given in eqn (2.42).

Polarization of the collected photons

Due to the finite physical dimensions, the microscope does not only collect photons emitted along the quantization axis, but all photons emitted into a certain spherical angle defined by the numerical aperture (NA) of the objective. For a NA of 0.38 (used in our experiment), this corresponds to a collection efficiency of 2.5% of the $\sigma^\pm$-polarized and 0.1% of the π-polarized photons. Thus, approximately 2% of the collected photons originate from a decay connected with the emission of π-polarization which would reduce the fidelity of the entangled qubit state.

---

[1]The state was generated in the decay of a spin zero particle. Thus, the sum of the angular momenta of its constituents has to sum up to zero.
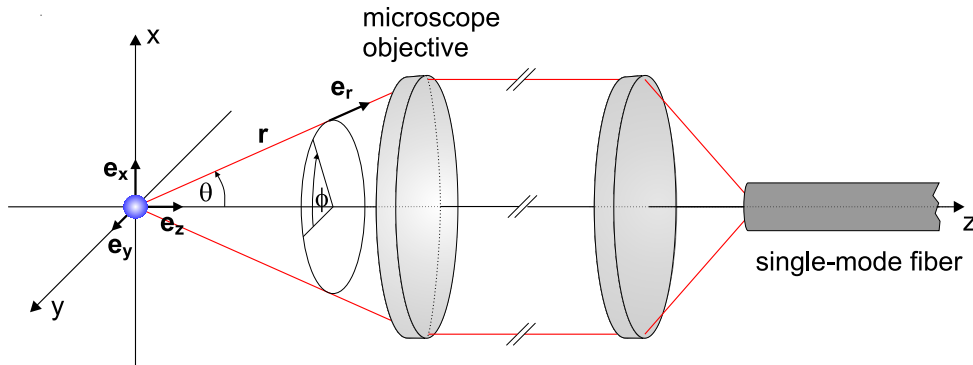
Figure 2.7.: Collection of fluorescence photons into a single-mode optical fiber. The emitted fluorescence light from the atom follows the classical dipole radiation pattern emitted from the three atomic dipoles arranged along $\mathbf{e_x}$, $\mathbf{e_y}$ and $\mathbf{e_z}$. In order to calculate the coupling efficiency into the single mode fiber, we evaluate the overlap of the emitted dipole radiation with the eigenmode of the optical single-mode fiber in the far field, where the emitted radiation can be described by a transversal electromagnetic wave.

However, in our experiment the collected fluorescence light is further coupled into a single-mode optical fiber with a well-defined spatial eigenmode, i.e. the TEM_{00} Gaussian eigenmode of the fiber. In order to calculate the coupling efficiency of the emitted photons into the optical fiber, we consider the atomic field modes that correspond to the radiation emitted from three atomic dipoles arranged along the unit vectors $\mathbf{e_x}$, $\mathbf{e_y}$ and $\mathbf{e_z}$ (see Fig. 2.7). Using the standard field decomposition into π and $\sigma^\pm$-polarization modes, the emitted field states are (see chapter A.3 and [60])

$$\mathbf{E_a^{\sigma^\pm}} = \frac{e^{ikr}}{r} E_a^\sigma \left[\mathbf{e_r} \times (\mathbf{e_x} \pm i\mathbf{e_y}) \right] \times \mathbf{e_r} \tag{2.43}$$

$$\mathbf{E_a^{\pi}} = \frac{e^{ikr}}{r} E_a^\pi \left[\mathbf{e_r} \times \mathbf{e_z} \right] \times \mathbf{e_r}, \tag{2.44}$$

with the normalization constants E_a^σ and E_a^π and the unit vector $\mathbf{e_r}$ pointing along the radial direction in the spherical coordinate system defined in Fig. 2.7. The angular dependence of the field is already included in the vector product and is equal to the dependence given in eqns (2.39) and (2.40). Now, we consider the mode field structure of the fluorescence light coupled into the optical single mode fiber, that together with the collection optics defines a Gaussian distribution of light with a beam waist w_0 at the position of the atom with the corresponding divergence angle $\theta_0 = \lambda/\pi w_0$. The light coupled into the fiber can be decomposed into the

two orthogonal polarizations σ^+ and σ^- with the corresponding field distributions $\mathbf{E_f}^{\sigma\pm}$ that for small divergence angles θ_0 are given by

$$\mathbf{E_f}^{\sigma\pm} = E_f \frac{e^{ikr}}{r} e^{-\theta^2/\theta_0^2} \left(\frac{(\mathbf{e_r} \times \mathbf{e_x}) \times \mathbf{e_r}}{|(\mathbf{e_r} \times \mathbf{e_x}) \times \mathbf{e_r}|} \pm i \frac{(\mathbf{e_r} \times \mathbf{e_y}) \times \mathbf{e_r}}{|(\mathbf{e_r} \times \mathbf{e_y}) \times \mathbf{e_r}|} \right) \qquad (2.45)$$

with the normalization constant E_f. The coupling efficiency of the different atomic field modes $\mathbf{E_a}$ into the Gaussian target modes $\mathbf{E_f}$ of the fiber can be calculated by evaluating the overlap of the two normalized modes over the half-sphere $(\theta = 0...\pi/2)$

$$p_{coupl} = \frac{1}{2} \left| \int_0^{2\pi} \int_0^{\pi/2} d\phi d\theta \sin\theta \, (\mathbf{E_f} \cdot \mathbf{E_a^*}) \right|^2 . \qquad (2.46)$$

Evaluation of eqn (2.46) shows that the coupling efficiency of π-polarized light into both fiber modes is zero as well as the coupling of $\sigma^\pm$-polarization into the (wrong) $\sigma^\mp$ fiber mode. This is due to the fact that in these cases the product $\mathbf{E_f} \cdot \mathbf{E_a^*}$ is an odd function with respect to ϕ and the corresponding integral is zero. Accordingly, the use of a single-mode fiber assures, that all photons coupled into the fiber originate from a decay generating the maximally entangled state in eqn (2.42), independent of the the collection angle of the microscope-fiber arrangement.

For the optical setup in our experiment, we measured a minimum waist of the fiber mode of $w_0 = 2.2 \ \mu$m at the position of the atom. This corresponds to a divergence angle of $\theta_0 = 6.5°$. Using eqn (2.46) we calculate a coupling efficiency $p_{coupl} = 0.94\%$ for $\sigma^\pm$-polarized light into the matching fiber mode. Averaging over all three emitted polarization modes this yields a mean photon coupling efficiency of 0.63% that together with the transmission losses and the detection efficiency of the single photon detectors gives rise a total detection probability of fluorescence photons of 0.1%.

To summarize, the coupling of the atomic fluorescence into a single-mode optical fiber assures that the detected photons belong to the same maximally entangled qubit state. Atom-photon entanglement is verified performing correlation measurements between the atomic and photonic spin state using a polarization measurement of the photon and an atomic superposition state detection process described in chapter 4. Both measurements are performed in the same spin-1/2 subspace of the spin-1 system generated in the spontaneous decay. Thus, the entangled atom-photon state should (in principle) be observable with fidelity one.

2.3. Summary

This chapter gave a short introduction into entangled states and their implications for the question if physical reality can be described by local realistic theories or not. Two applications of entanglement are presented: quantum teleportation and entanglement swapping, that form the basic steps in many quantum information and communication protocols. The second part of this chapter showed, that spontaneous decay is an excellent source for the generation of entanglement between the polarization of the emitted photon and the internal degree of freedom of the atom. Furthermore, using a single-mode optical fiber for the collection of the

atomic fluorescence assures that only photons originating from a maximally entangled state are detected. The experimental realization and observation of this state is the main goal of this thesis as it presents an important step towards the realization of quantum networks as well as for a final loophole-free test of Bell's inequality.

3. Setup and trap characteristics

Contents

The preparation and detection of entanglement between a single atom and a spontaneously emitted photon requires the faithfull manipulation and detection of internal atomic levels. Therefore, the basic ingredient of our experiment is a single atom isolated from the environment at a well defined position. In principle, atom-photon entanglement can be generated using ions or neutral atoms. With regard to applications in quantum communication which require the distribution of entanglement over large distances, the emitted photon should allow low-loss transport over large distances. Thus, neutral atoms with transition frequencies in the visible or near infrared are preferable to ions with transition frequencies mostly in the ultraviolet spectral region. A single neutral ^{87}Rb atom is an optimal choice for the generation of atom-photon entanglement due to its weak coupling to the environment and the optimal internal level structure. Furthermore, the first excited states – the D_1- (795 nm) and the D_2-line (780 nm) – can easily be addressed by commercially available laser diodes and the wavelength of

the emitted fluorescence photons allows long distance transport in standard optical fibers and an efficient detection of single photons.

The generation of atom-photon entanglement via spontaneous decay poses two restrictions on the possible trapping schemes of the atom. On the one hand, it is important to prepare and analyze internal atomic states, thus the trap should not rely on dissipative forces as e.g. radiation-pressure in magneto-optical traps (MOTs) [61, 62]. Furthermore, the trap must provide an attractive potential for the atomic ground state with identical potential depth for all magnetic sublevels, otherwise the different decay channels of the spontaneously emitted photons become spectrally distinguishable, thus reducing the fidelity of the entangled state. This restriction also excludes magnetic traps [63, 64], where the trapping potential relies on the orientation of the atomic magnetic dipole moment relative to the external magnetic field and thus depends on the magnetic sublevel of the atom. Another trapping mechanism is provided by optical dipole traps [65] where the trap potential depends on the interaction of the oscillating electric field of an incident light beam with the induced electric dipole moment of the atom. For far red-detuned linearly polarized light this results in a conservative trapping potential for the atom, independent of the ground state hyperfine and Zeeman structure. Furthermore, in tightly focused laser beams a blockade mechanism occurs, setting the maximum number of atoms inside these traps to one. Therefore, far off-resonant optical dipole traps provide a relative simple trapping scheme and together with the blockade mechanism they are a powerfull tool for experiments in quantum optics. Thus in our experiment, the trapping of a single atom is realized using an optical dipole trap.

The following chapter first gives a short introduction into the physics of optical dipole traps. Afterwards, the main setup of our experiment is presented including the dipole trap, the detection optics for the atomic fluorescence and the laser system necessary for cooling and detection of the atom. The presence of an atom inside the trap is verified by analyzing the temporal evolution of the collected fluorescence light. The fluorescence signal of the trapped atoms shows the presence of a blockade mechanism that sets the maximum atom number in the trap to one. Because this blockade effect would result in a considerably simpler experimental scheme we verified its presence by measuring the second order correlation function of the fluorescence light in a Hanbury-Brown Twiss setup. The observed photon anti-bunching verifies the presence of only single atoms in the trap. Another characteristic – important for interference experiments involving photons emitted from the atom – is the residual kinetic energy of the atom that gives rise to an incoherent broadening of the fluorescence spectrum. Therefore, a spectral analysis of the emitted fluorescence light is performed. From the spectral broadening of the fluorescence light relative to the exciting light field, we derive an estimation of the mean kinetic energy of the atom.

3.1. Optical dipole forces

The trapping of a single atom in an optical dipole trap represents an important step of our experiment. Therefore, this chapter gives a short introduction into the physics of optical dipole forces. In principle, these forces emerge from the interaction of the oscillatory electric field of an inhomogeneous light beam with the induced electric dipole moment of the atom. Averaged over one period of the rapidly oscillating light field this results in an attractive or repulsive

force on the atom, for a light field red respective blue detuned relative to the atomic transition. Using a red detuned focused Gaussian laser beam the attractive force generates a potential minimum at the beam focus. Thus, an optical dipole trap is generated, with the trap center at the position of the beam focus.

3.1.1. Classical oscillator model

Consider an atom placed in a laser light field with the electric field $\mathbf{E}$ oscillating at angular frequency ω. The oscillating electrical field induces the electric dipole moment $\mathbf{d} = \alpha(\omega)\mathbf{E}$ in the atom, oscillating with the same frequency as the driving light field. The value α is the complex polarizability of the atom that depends on the frequency of the electric field and the internal energy levels of the atom. The interaction of the induced dipole with the driving field results in the interaction potential

$$U_{\mathrm{dip}} = -\frac{1}{2}\langle \mathbf{dE} \rangle = -\frac{1}{2\epsilon_0 c}\mathrm{Re}(\alpha)\bar{I}, \tag{3.1}$$

where the brackets denote the time average over the rapid oscillatory terms and $\bar{I} = 2\epsilon_0 c E_0^2$ is the mean intensity of the driving field with amplitude E_0. The trapping potential U_{dip} is proportional to the intensity of the light field and the real part of the atomic polarizability that describes the component of the atomic dipole in phase with the driving field. The absorption respective scattering rate is given by the imaginary part of α by

$$\Gamma_{\mathrm{sc}} = \frac{P_{\mathrm{abs}}}{\hbar\omega} = -\frac{\langle \dot{\mathbf{d}}\mathbf{E} \rangle}{\hbar\omega} = -\frac{1}{\hbar\epsilon_0 c}\mathrm{Im}(\alpha)\bar{I}. \tag{3.2}$$

The polarizability α can be calculated from the classical Lorentz oscillator model and is given by [66]:

$$\alpha = 6\pi\epsilon_0 c^3 \frac{\Gamma/\omega_0^2}{\omega_0^2 - \omega^2 - i(\omega^3/\omega_0^2)\Gamma}. \tag{3.3}$$

Here ω_0 denotes the atomic resonance frequency and Γ is the on-resonance damping rate. In a semiclassical approach the atomic polarizability is calculated using a two-level atom interacting with a classical radiation field. When saturation effects can be neglected ($\Gamma_{\mathrm{sc}} \ll \Gamma$, which is usually the case for optical dipole traps) this model yields the same result as the classical Lorentz-oscillator approach. The damping rate Γ (corresponding to the spontaneous scattering rate of the excited state), thereby is given by

$$\Gamma = \frac{\omega_0^3}{3\pi\epsilon_0 \hbar c^3}|\langle e|\hat{\mathbf{d}}|g\rangle|^2, \tag{3.4}$$

where $\hat{\mathbf{d}}$ is the electric dipole operator connecting the atomic ground and excited states $|g\rangle$ and $|e\rangle$. From eqns (3.3) and (3.4) we can calculate the dipole potential and the atomic scattering rate [66]:

$$U_{\mathrm{dip}}(\mathbf{r}) = -\frac{3\pi c^2}{2\omega_0^3}\left(\frac{\Gamma}{\omega_0 - \omega} + \frac{\Gamma}{\omega_0 + \omega}\right)I(\mathbf{r}) \quad \approx \frac{3\pi c^2}{2\omega_0^3}\frac{\Gamma}{\Delta}I(\mathbf{r}) \tag{3.5}$$

$$\Gamma_{\mathrm{sc}}(\mathbf{r}) = \frac{3\pi c^2}{2\hbar\omega_0^3}\left(\frac{\omega}{\omega_0}\right)^3\left(\frac{\Gamma}{\omega_0 - \omega} + \frac{\Gamma}{\omega_0 + \omega}\right)^2 I(\mathbf{r}) \quad \approx \frac{3\pi c^2}{2\hbar\omega_0^3}\left(\frac{\Gamma}{\Delta}\right)^2 I(\mathbf{r}). \tag{3.6}$$

In these equations $\Delta = \omega - \omega_0$ is the detuning of the light field relative to the atomic resonance. On the righthand side of the above equations the rotating wave approximation has been applied (neglecting the fast oscillatory terms $\omega_0 + \omega$). The potential depth U_{dip} is proportional to the light intensity. Thus, for inhomogeneous light fields a dipole force occurs. Two possible cases exist: For red detuned light ($\Delta < 0$) U_{dip} is negative and an attractive potential towards the maximum field amplitude is created, whereas for blue detuned light ($\Delta > 0$) a repulsive potential occurs. Furthermore, the dipole potential is conservative which gives the important condition of a friction force for the loading of atoms into optical dipole traps.

The origin of the dipole force can be understood in the picture of a classical atomic oscillator. In the case of far red detuned light the atomic dipole follows the electric field (the phase difference between the atomic dipole and the exciting field is negligible) and therefore the dipole is oriented parallel to the electric field in order to minimize the potential energy resulting in an attractive force. Near resonance the atomic dipole follows the electric field with a phase difference of $\pi/2$ and above resonance the phase difference between the dipole and the electric field increases to π. This results in the maximum dipole energy and therefore gives rise to a repulsive potential.

3.1.2. Quantum mechanical approach
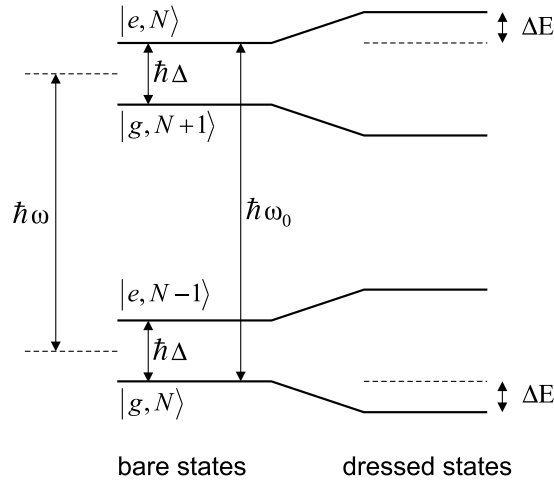

Figure 3.1.: Dressed state picture of a two-level atom with ground state $|g\rangle$, excited state $|e\rangle$ and transition frequency ω_0 interacting with a light field of frequency ω and photon number N. The interaction between the atom and the light gives rise to an energy shift ΔE (light shift) of the ground and excited states of the atom.

The consideration above gives the same result as the quantum mechanical approach for a two-level atom. In reality, the transitions in atoms have a complex structure which can not be described by a simple two-level model. For systems with a more difficult level structure this results in a dipole potential, that in general depends on the particular state of the atom. An accurate description can be obtained in the dressed state picture describing the combined system of the atom and the quantized electromagnetic field. The effect of the far-detuned light field on the atom can be treated as a second order perturbation in the electric field. The interaction of the atom with the light field (given by the interaction Hamiltonian $\hat{H}_{ED} = -\hat{\mathbf{d}}\hat{\mathbf{E}}$) leads for the non-degenerate atomic states $|i\rangle$ to an energy shift [66] ΔE_i of

$$\Delta E_i = \sum_{j \neq i} \frac{|\langle j|\hat{H}_{\mathrm{ED}}|i\rangle|^2}{\epsilon_i - \epsilon_j}, \tag{3.7}$$

where ϵ_i are the energies of the unperturbed states in the dressed state picture. If, e.g., the atom is in the ground state $|i\rangle$ and the light field consists of N photons with frequency ω, the unperturbed energy of the system is $\epsilon_g = N\hbar\omega$. On the other hand, if the atom is excited to the state $|j\rangle$ with energy $\hbar\omega_j$ by absorbing one photon, the unperturbed energy of the atom-photon system is given by $\epsilon_j = \hbar\omega_j + (N-1)\hbar\omega = -\hbar\Delta_j + N\hbar\omega$. For a two-level atom (see Fig. 3.1) eqn (3.7) reduces to

$$\Delta E_{g/e} = \pm\frac{|\langle e|\hat{\mathbf{d}}|g\rangle|^2}{\Delta}|E|^2 = \pm\frac{3\pi c^2}{2\omega_0^3}\frac{\Gamma}{\Delta}I \tag{3.8}$$

where $\Delta = \omega - \omega_0$ is the detuning of the light field relative to the atomic transition. The plus and the minus sign correspond to the shift of the ground and the excited state, respectively. In this picture the dipole potential is generated by an energy shift (the so-called *light shift*) of the ground state caused by the interaction of the light field with the atom. This shift is equal to the potential calculated from the classical approach in eqn (3.5). For the excited state the we obtain a shift of equal size but of opposite sign. In the interesting case of low saturation, the atom stays most of the time in the ground state and thus the light shift of the ground state is the relevant trapping potential.

Level substructure

For atoms with level substructure all possible dipole matrix elements $\mathbf{d}_{ij} = \langle g_i|\hat{\mathbf{d}}|e_j\rangle$ for transitions between specific atomic ground $|g_i\rangle$ and excited states $|e_j\rangle$ have to be taken into account. For a given transition these matrix elements reduce to

$$\mathbf{d}_{ij} = c_{ij}||\mathbf{d}||, \tag{3.9}$$

where $||\mathbf{d}||$ is the reduced dipole matrix element that depends only on the electronic orbital wavefunctions and therefore is directly related to the spontaneous decay rate of the transition. The coefficients c_{ij} are real parameters denoting the transition strength of the specific sublevels. They depend on the laser polarization and the electronic and nuclear angular momenta involved [67].

Rubidium 87

Rubidium 87 is an alkali atom with nuclear spin $I = 3/2$. The fine structure splitting of the first excited state ($5^2P_{1/2}$, $5^2P_{3/2}$) leads to the D-line doublet with transition wavelengths of 795 nm and 780 nm, respectively. Neglecting further excited states, eqn (3.7) allows to calculate the dipole potential of the atomic ground state $5^2S_{1/2}$ with total angular momentum F and magnetic quantum number m_F. For the case of small excited state hyperfine splitting compared to the detuning of the dipole laser field, we obtain [66]

$$U_{\mathrm{dip}} = \frac{\pi c^2 \Gamma}{2\omega_0^3} \left(\frac{2 + \wp g_F m_F}{\Delta_{2,F}} + \frac{1 - \wp g_f m_F}{\Delta_{1,F}} \right) \cdot I(\mathbf{r}), \tag{3.10}$$

where g_F is the atomic Landé factor, $\wp$ characterizes the light polarization ($\wp = 0, \pm 1$ for π- and $\sigma^\pm$-polarized light, respectively), and $\Delta_{1,F}$ and $\Delta_{2,F}$ refer to the detuning of the light field relative to the D_1 and D_2 line, respectively. In the case of very large detuning compared to the fine structure splitting ($\Delta_1 \approx \Delta_2 = \Delta$) eqn (3.10) reduces to the result obtained for a two level atom (see eqn (3.8)).

An important aspect of eqn (3.10) is the dependence of the dipole potential on the polarization of the light field. For circularly polarized light ($\sigma^\pm$), the degeneracy of the magnetic sublevels of the ground state is lifted and therefore the light shift of the different sublevels depends on the quantum number m_F. For the generation of atom-photon entanglement, this level shift is critical because (for deep trapping potentials) it gives rise to a spectral distinguishability of the transitions involved in the creation of the entanglement. Therefore, linearly polarized light is the best choice in order to maintain the degeneracy of the Zeeman sublevels of the ground state of a trapped atom.

In the case of linearly polarized light the inelastic scattering rate is given by the expression

$$\Gamma_{\mathrm{sc}} = \frac{\pi c^2 \Gamma^2}{2\hbar\omega_0^3} \left(\frac{2}{\Delta_{2,F}^2} + \frac{1}{\Delta_{1,F}^2} \right) \cdot I(\mathbf{r}), \tag{3.11}$$

and is independent of the magnetic quantum number.

The results derived here are valid for the ground state of an alkali atom with only one excited state. If one includes the additional excited states and takes also into account the Zeeman splitting, the above results for the atomic ground states are still qualitatively valid. The absolute light shift of the ground state changes about 10 percent due to coupling to higher excited levels but is still independent of the specific Zeeman sublevel (for a more detailed discussion see [68]).

3.1.3. Focused beam traps

The dipole potential described above allows to form a trap for neutral atoms using a red detuned Gaussian laser beam focused to a tight spot. The light shift of the atoms is maximal at the focus of the laser beam, thus a three dimensional confinement of the atoms is created. In detail, the intensity profile of a Gaussian laser beam propagating along z-direction is given by

$$I(r,z) = \frac{2P}{\pi w^2(z)} e^{-\frac{2r^2}{w^2(z)}}, \tag{3.12}$$
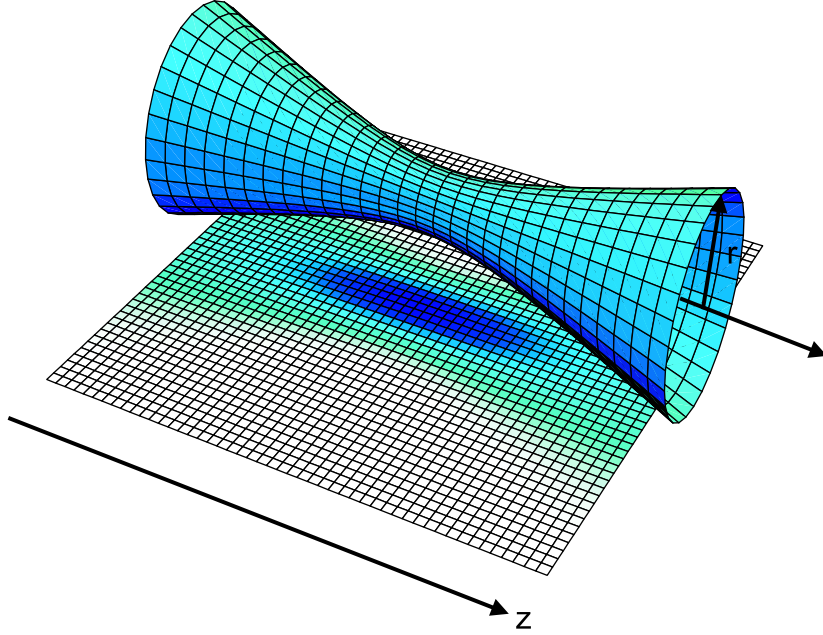
Figure 3.2.: The figure shows the $1/e^2$ beam radius $w(z)$ of a Gaussian laser beam in the focal region and a contour plot of the appropriate trapping potential.

where P is the power of the laser beam and r defines the distance from the optical axis. The $1/e^2$-radius $w(z)$ of the laser beam is defined by

$$w(z) = w_0\sqrt{1 + z^2/z_R^2} \tag{3.13}$$

with the Rayleigh length $z_R = \pi w_0^2/\lambda$, the minimum beam radius or beam waist w_0 and the wavelength λ of the light field. In the beam focus an ellipsoidal trapping region is formed with a potential that can be approximated near the center of the beam by the harmonic potential

$$U(r,z) \approx -U_0 \left[1 - 2\left(\frac{r}{w_0}\right)^2 - \left(\frac{z}{z_R}\right)^2 \right]. \tag{3.14}$$

The maximum trap depth U_0 for a two-level atom is

$$U_0 = \frac{3c^2}{\omega_0^3 w_0^2}\frac{\Gamma}{\Delta}P, \tag{3.15}$$

and the transversal and longitudinal trap frequencies are given by

$$\omega_r = \sqrt{\frac{4U_0}{mw_0^2}} \quad \text{and} \quad \omega_z = \sqrt{\frac{2U_0}{mz_R^2}}. \tag{3.16}$$

Summary

A Gaussian laser beam red-detuned to the atomic transition allows to trap atoms in the beam focus. The generated dipole trap has an elliptical shape with a tight confinement perpendicular to the laser beam with the trap frequency ω_r. Parallel to the beam direction the trap provides only a weak potential gradient with a relative small trap frequency ω_z due to the large Rayleigh length $z_R \gg w_0$ of Gaussian beams (see Fig. 3.2).

3.2. Single atom dipole trap

The main ingredient for the generation of atom-photon entanglement is a single trapped atom, with a trapping mechanism, independent of the Zeeman sublevel of the atomic ground state. For this purpose, we use an optical dipole trap, generated by the linearly polarized light field of a focused Gaussian laser beam, red-detuned to the transition to the first excited state. Due to the conservative nature and the small depth of the dipole potential, the ^{87}Rb atoms have to be cooled in a magneto-optical trap (MOT), that also provides an adjustable density of the background gas of cold atoms.

The fluorescence of the trapped atoms in the cooling light is collected in a confocal arrangement with the trapping beam and measured by Si-avalanche photo diodes. The presence of an atom in the dipole trap can directly be observed by the increase of the detected fluorescence. Analyzing the fluorescence light, we obtain a lifetime of atoms inside the trap of approximately two seconds. Furthermore, we observe only fluorescence corresponding to one or zero atoms in our dipole trap. This is caused by the small trapping beam waist of 3.5 μm, that greatly enhances the inelastic collision rate in the dipole trap and thus gives rise to a blockade effect that limits the maximum atom number in the trap to one [69, 70]. This blockade mechanism is an important aspect of our experiment because it assures that only single atoms are present and therefore allows much simpler experimental schemes.

3.2.1. Experimental setup

In our experiment the atoms are stored in an optical dipole trap which allows a typical potential depth of a few mK. Due to the shallow trapping potential, collisions with the background gas lead to an immediate loss of the atom from the trap. In order to surpress the collision rate, the experiment has to be performed in ultra high vacuum (UHV) conditions. The vacuum is maintained by an ion getter pump (Varian, Star Cell, 24 l/s) and the experimental area is defined by a commercial uncoated spectroscopy glass cell connected to the vacuum system by an indium gasket. A Rubidium dispenser constantly operating slightly above threshold (2.5 A) serves as source of ^{87}Rb atoms. Under these conditions we achieve a background gas pressure
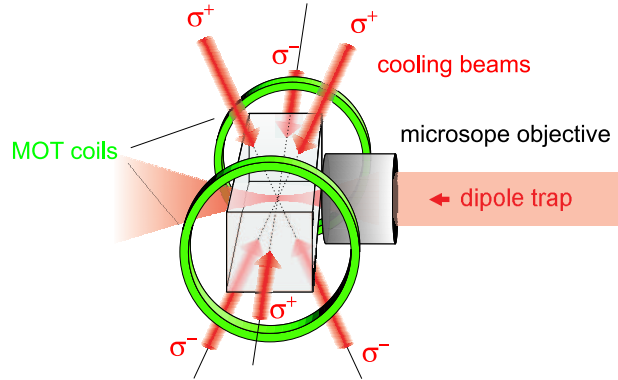
Figure 3.3.: Schematic setup of the magneto optical trap and dipole trap. Three counter-propagating beam pairs provide laser cooling. Together with the magnetic quadrupole field generated by two coils in anti-Helmholtz configuration, a magneto-optical trap is realized. The MOT provides a dissipative force towards the center of the quadrupole field that overlaps with the dipole trap. Due to restricted space around the vacuum chamber the two beams in the plane parallel to the dipole trap axis are not perpendicular but include a angle of $34°$.

inside the vacuum chamber of less than 10^{-10} mbar that should allow lifetimes of atoms in the dipole trap up to several seconds.

Laser cooling and magneto-optical trap

Optical dipole traps provide a shallow and conservative trapping potential. Thus, a friction force is necessary to load atoms into the trap. In our experiment the friction force is generated by three-dimensional laser cooling generating an optical molasses [71, 72, 73]. The optical cooling is performed using two laser systems. The cooling laser – red detuned to the transition $5^2S_{1/2}$, $F = 2$ to $5^2P_{3/2}$, $F' = 3$ by 5-6 linewidths (24-30 MHz) – provides the actual cooling mechanism. The repump laser – resonant to $5^2S_{1/2}$, $F = 1$ to $5^2P_{3/2}$, $F' = 2$ – is necessary to form a closed transition. Both laser systems consist of a grating stabilized laser diode locked to atomic transition via Doppler-free saturation spectroscopy [21]. With this method we obtain a long term frequency stability better than 2 MHz and a spectral line width of less than 700 MHz [21]. Fine tuning of the laser frequency and power is realized using acousto optical modulators (AOMs). Finally, the two beams are combined and guided to the actual experiment where the power of each beam (cooling and repump light) is monitored by a photo diode to realize a power stabilization of each light field. The light is split into three pairs of counterpropagating

orthogonally circular polarized beams intersecting at the position of the dipole trap (see Fig. 3.3). In the intersection region sub-Doppler cooling mechanisms should occur [74] cooling the atoms down to final temperatures below the Doppler limit of ^{87}Rb of 146 μK [75, 67].

Laser cooling is only possible for atoms with a temperature below a certain threshold of about 0.2 K. The atoms provided by the Rb-dispenser have a temperature of more than 800 K, thus, the fraction of atoms that can be cooled in the optical molasses is on the order of 10^{-6}. For a suitable lifetime of atoms in the dipole trap, a low background gas pressure is essential. This sets a limit on the density of cold atoms in the optical molasses, that would result in a minimum loading time of the dipole trap on the order of 10 seconds which is too small to ensure an efficient repetition rate of our experiments.

In order to provide a reservoir of cold Rubidium atoms with higher density we use a magneto-optical trap (MOT) formed by the cooling and repump beams together with a magnetic quadrupole field generated by two coils in an anti-Helmholtz configuration [67]. The magnetic field induces a position dependent frequency shift of the atomic Zeeman sublevels, that together with the cooling light leads to a dissipative force towards the MOT center (see chapter A.1.3). With the maximum current of 2 A in our experiment we can generate a magnetic field gradient up to $\partial B/dz = 11$ G/cm. Together with a waist of the cooling beams of 1 mm this allows to store typically 3×10^4 cold atoms inside the MOT (see Fig. 3.4). Changing the magnetic field gradient of the MOT we can adjust the number of cold atoms in the MOT cloud and thus the loading rate of atoms into the dipole trap from approximately 0.1 s^{-1} (for zero field) to more than one atom per second[1] for a field gradient of 2 G/cm (see [68]).

Figure 3.4.: CCD-image of the cloud of cold atoms in the magneto-optical trap (observation direction along the dipole trap axis). The vertical and horizontal lines show light scattered by hot background gas in the cooling beams. At the intersection region a cloud of approximately 3×10^4 cold atoms can be observed (the atom number was estimated from the measured fluorescence).
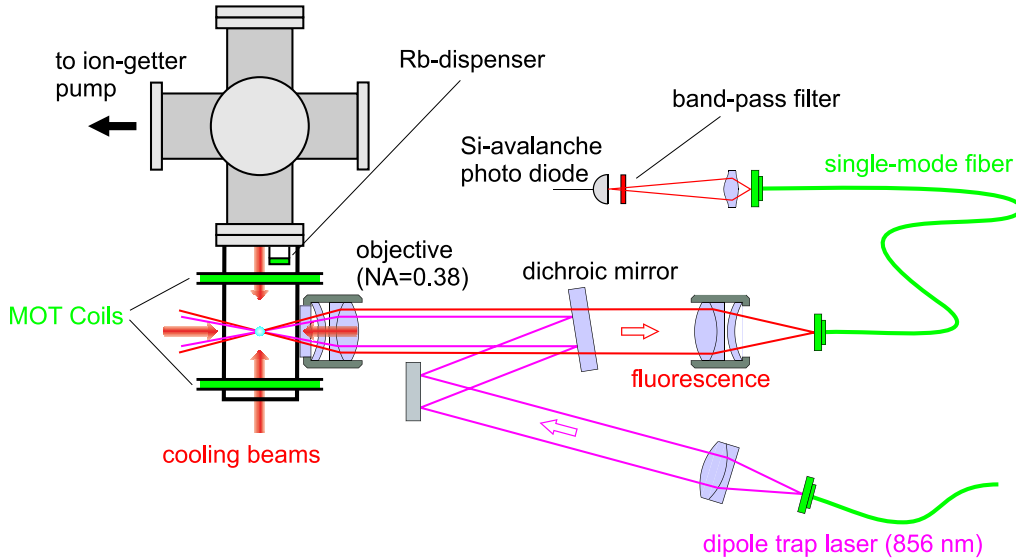
Figure 3.5.: Top view of the dipole trap and the detection optics. The dipole trap is generated by a single mode laser diode focused into the vacuum chamber at the center of the MOT. The fluorescence of the trapped atom is collected in a confocal arrangement with the dipole trap laser and coupled into a single mode optical fiber for spatial filtering. The photons are detected using a Si-avalanche photo diode.

Dipole trap and detection optics

The dipole trap is generated by a laser beam from a single mode laser diode with a peak power of 200 mW and a wavelength of 856 nm, far red-detuned to the first excited state of ^{87}Rb ($\lambda = 780$ and $\lambda = 795$ nm). A single-mode optical fiber guides the light to the experimental setup and ensures a Gaussian beam profile. In order to work only with a single atom, we make use of a blockade mechanism occurring for small optical dipole traps with a beam waist below $4~\mu$m (see next chapter and [69, 70]) that limits the maximum number of atoms inside the trap to one. For this purpose, the dipole trap light is focused to a waist of $w_0 = 3.5 \pm 0.2~\mu$m at the center of the MOT by a commercial microscope objective (NA 0.38) located outside the vacuum chamber (see Fig. 3.5). The intensity of the trapping light field is actively stabilized by monitoring the light transmitted through the glass cell with a photodiode and adjusting the dipole laser power with an AOM. We achieve typical laser powers of 30 mW at the trap region,

---

[1]In principle, our MOT parameters also allow a higher loading rate, but due to the blockade mechanism (see next chapter) this would result in a strong decrease of the lifetime of atoms in the dipole trap.

corresponding to a potential depth of approximately 860 μK with longitudinal and transversal trap frequencies of 1.4 kHz and 26 kHz, respectively, and a photon scattering rate from the trapping beam of 20 s^{-1}.

The fluorescence light from the dipole trap region is collected with the microscope objective and separated from the trapping beam by a dichroic mirror that is highly reflective for the trapping light and has a polarization independent transmission of 90% for the atomic fluorescence (see Fig. 3.5). In order to suppress stray light the collected fluorescence is coupled into a single mode optical fiber for spatial filtering. The fiber guides the light to silicon-avalanche photo diodes (Si-APDs) used for single photon detection. Band-pass filters (central wavelength: 780 nm, FWHM: 2 nm) in front of the APD further suppress stray light contributions from off resonant light.

In order to calculate the collection efficiency of the emitted photons, we consider the mode field structure of the fluorescence light coupled into the optical fiber, that together with the collection optics defines a spatial distribution of light with a beam waist of 2.2 ± 0.2 μm at the dipole trap center. Calculating the overlap of the Gaussian field mode of the fiber with the electrical field distribution emitted by the single atom, we obtain a total detection efficiency of emitted photons of approximately 0.1%, including transmission losses through the optical components and the quantum efficiency of the APDs (see chapter 2.2.4).

3.2.2. Observation of single atoms

In order to load an atom into the dipole trap, the cooling and repump light is turned on and the MOT field gradient is optimized to ensure a high loading rate without drastically decreasing the trap liftime. The fluorescence from the dipole trap region is measured on a single photon level with an APD. Every time an atom is cooled into the trap we observe an increase of the fluorescence count rate. With no atom in the trap a background count rate of 450 counts/s is detected due to dark counts of the detector and stray light from background gas. When an atom enters the trap the fluorescence increases to 1000-2300 counts/s depending on the intensity and detuning of the cooling laser. Figure 3.6 shows a fraction of a fluorescence measurement with a time resolution of 0.1 s. The presence of atoms inside the dipole trap can be observed in real time by the occurrence of distinct steps in the fluorescence count rate.

Sub-Poissonian loading statistics

Histogramming the number of occurrences of the detected count rates for a long time measurement we obtain two distinct peaks (Fig. 3.7). The first peak corresponds to the background count rate of the APD and the second one to the fluorescence detected from a single atom inside the trap. Assuming a Poissonian distribution of the number of trapped atoms, a third peak at twice the single atom count rate should appear but is not observed. The absence of this peak shows a sub-Poissonian occupation statistics of atoms in the dipole trap, i.e. the probability to trap two (or more) atoms can be neglected. This effect occurs in microscopic dipole traps and was first observed in [69, 70]. In detail, the blockade can be explained by cooling light induced inelastic two-body collisions between cold atoms and is caused by two physical processes [76, 77, 78]. On the one hand, if the two atoms are not in the absolute ground state, even the small amount of energy from the hyperfine splitting of the $F = 1$ and
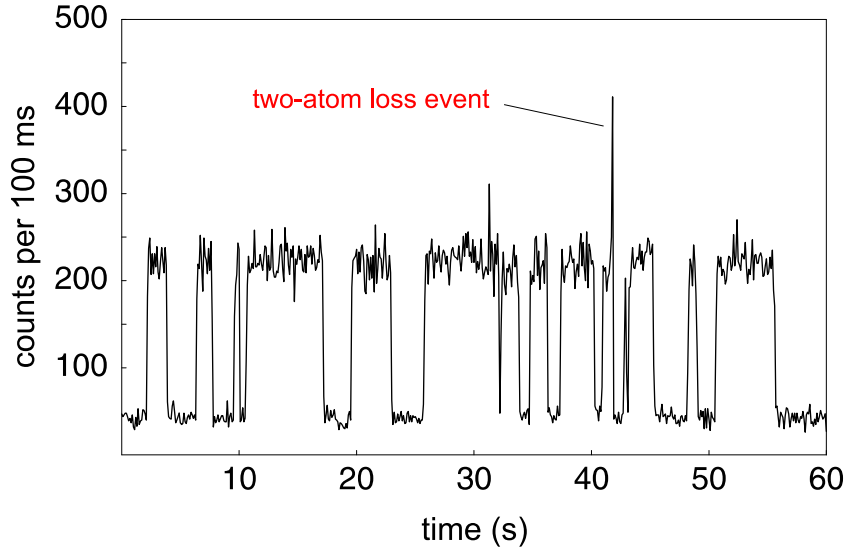
Figure 3.6.: Fluorescence counts per 100 ms observed from the dipole trap region. If no atom is inside the dipole trap we observe a background count rate of 450 s^{-1} and in case an atom enters the trap the count rate increases to 2200 counts per second. A blockade mechanism [69, 70] due to the small trap size ensures that only single atoms can be loaded into the trap.

$F = 2$ ground states, released in an inelastic collision, is enough to eject both atoms from the trap. Another loss effect occurs from collisions where one atom is in the excited state and a losely bound Rb$_2$ molecule is generated. The molecule dissociates due to spontaneous emission of a photon and both atoms are ejected from the trap. In the radiative decay process the molecule decays to the unbound ground state, whereas in fine structure changing collision the attractive potential of the $^2S_{1/2} -^2 P_{3/2}$ molecular state changes to the repulsive potential of the $^2S_{1/2} -^2 P_{1/2}$ state. In both processes the kinetic energy necessary to eject the atoms from the trap comes from the fact that the emitted photon has a lower energy than the photon absorbed from the cooling light during the formation of the molecule.

Due to the small size of the dipole trap the probability of these collisions is strongly increased and the loading of a second atom into the dipole trap leads to an allmost immediate loss of both atoms. Figure 3.6 shows an event which could be attributed to light-induced collisions. For a short time, fluorescence corresponding to two atoms is detected and in the following collision both atoms are lost from the trap and only the background count rate is observed.

Changing the magnetic field gradient of the MOT, it is in principle possible to increase the loading rate into the dipole trap until it is higher than the rate of inelastic two-body collision.
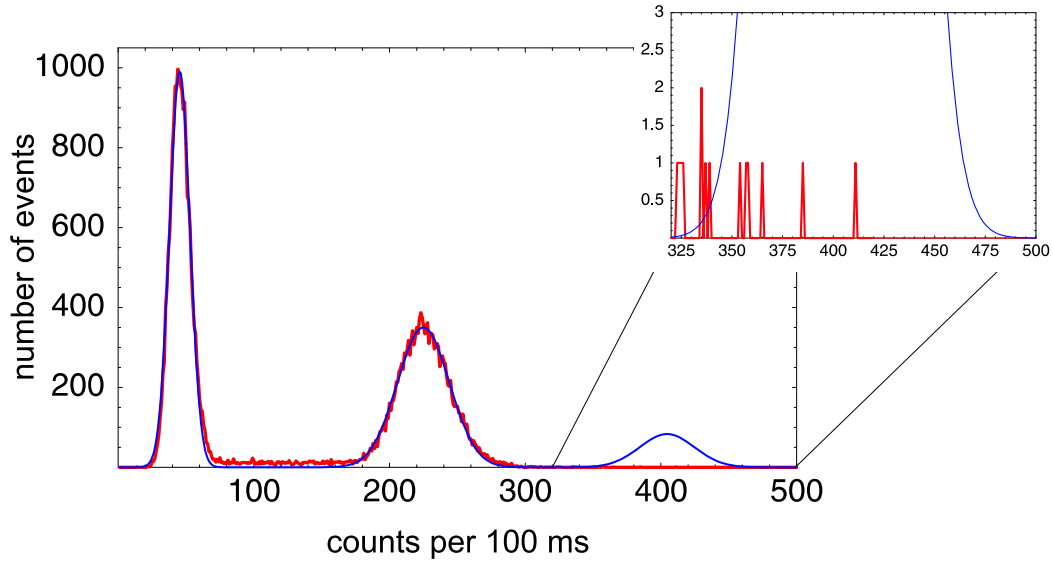
Figure 3.7.: Histogram of the fluorescence counts per 100 ms from a total measurement time of more than five hours. The red data corresponds to the measured number of occurrences of the respective count rate. The blue curve is a theoretical fit to the first two peaks assuming Poissonian occupation statistics of the dipole trap. The fluorescence events in the first peak are caused by the background count rate of the detector and the second and third peak correspond to the cases with one or two atoms inside the dipole trap. The inset shows a magnification of the region around the third peak. The probability to see two (or more) atoms inside the dipole trap is nearly zero and therefore clearly differs from a Poissonian distribution expected for non-interacting atoms.

Thus, it is possible to overcome the blockade and load more than one atom into the trap. But this regime only occurs for high densities of cold background gas and therefore at much higher field gradients of the MOT. Thus, it can easily be separated from the interesting regime where the blockade mechanism occurs and the loading rate is acceptably high. A more detailed discussion of the effects of the blockade mechanism for the occupation statistics of our dipole trap can be found in [68].

The collisional blockade mainly occurs in the presence of cooling light. Without optical cooling it is in principle possible to store more than one atom in the trap. However, in this case, loading of further atoms into the dipole trap is forbidden due to the conservative nature of the trapping potential. Therefore, the collisional blockade effect provides us with an elegant mechanism to ensure that only a single atom is present in the dipole trap, which is a crucial condition for the generation and verification of atom-photon entanglement.

Dipole trap lifetime
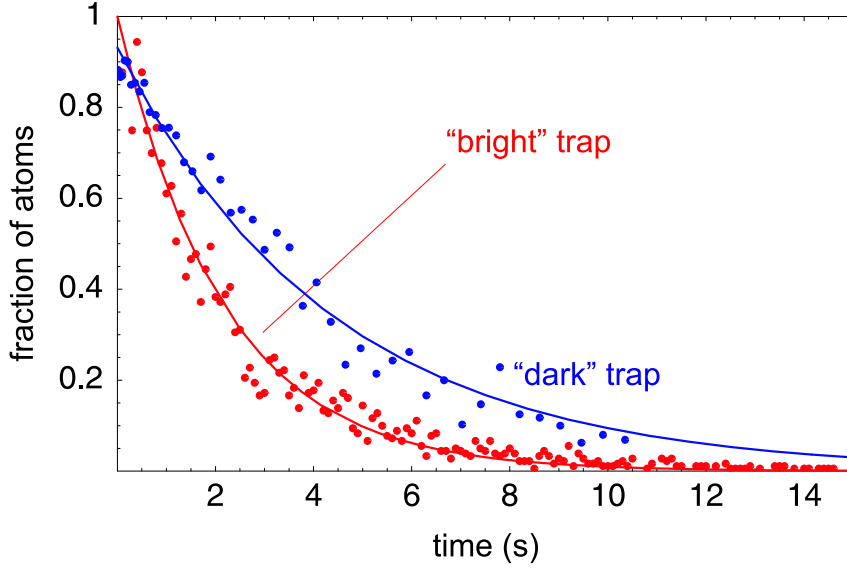
Figure 3.8.: Lifetime of the single atom inside the dipole trap in the presence of cooling light ("bright" trap, red data) and without cooling light ("dark trap", blue data). The solid lines are exponential fits to the measured data which yield a lifetime of 2.2 ± 0.2 s and 4.4 ± 0.2 s for the "bright" and the "dark" trap, respectively.

For most experiments the lifetime of the atom in the optical dipole trap is a crucial parameter. Due to the collisional blockade effect two interesting cases with different dipole trap lifetimes exist. In the case where no cooling light is present ("dark" trap), the lifetime is dominated by collisions of the trapped atom with the hot background gas and parametric heating from fluctuations of the dipole trap potential. In the presence of cooling light ("bright" trap) the blockade effect occurs and an additional loss channel is created: light induced inelastic collisions between two cold atoms. Therefore, we expect a shorter trap lifetime for the "bright" trap with its additional loss channel.

The lifetime of a single atom in the dipole trap in the presence of cooling light is calculated directly from the measured fluorescence traces (see Fig. 3.6), where a count rate above a certain threshold corresponds to the case where the atom is still inside the trap. For the "dark" trap, the lifetime is determined in the following way. First the cooling-light is switched on until an increase in fluorescence counts is detected, indicating the presence of a single atom. Then, the

cooling and repump light is switched off for a certain time Δt and then switched on again. Integrating the photon count rate in the final fluorescence detection process for 100 ms allows to distinguish if the atom is still in the trap or if it was lost. This measurement is repeated many times for different time delays Δt to obtain the fraction of atoms still present in the trap.

Figure 3.8 shows the fraction of atoms that survived inside the dipole trap after a certain time. From these curves we derive a $1/e$ lifetime of about two seconds for the "bright" and approximately four seconds for the "dark" trap[2], which shows the expected higher loss rate in the presence of cooling light. Both lifetimes are sufficiently high for our purpose because they are two orders of magnitudes larger than the typical timescale necessary for the generation and verification of atom-photon entanglement.

3.3. Photon statistics of the fluorescence light

The analysis of the counting statistics in the preceding chapter showed the evidence of a blockade mechanism that allows to store only single atoms in the optical dipole trap. Experiments that depend on single atoms would considerably benefit from such a mechanism. Thus, it is important to obtain a further prove for the single atom characteristic of the dipole trap. This can be derived by analyzing the statistical properties of the atomic fluorescence light. The properties of fluorescence scattered by a single atom differ from a system consisting of more than one emitter. In contrast to a system with many emitters, a single atom can emit only a single photon per time. Thus the second order correlation function of the single atom fluorescence light should show perfect photon-antibunching.

We performed a Hanbury-Brown Twiss (HBT) measurement [79] that allows to analyze the photon statistics of the atomic fluorescence light. Photon-antibunching in the measured second order correlation function shows that only a single atom is trapped and thus proves the collisional blockade indicated in the analysis of the fluorescence count rates. Furthermore, the measured second order correlation function contains a signature of the internal and external atomic dynamics and explicitly shows effects from the effective four level system coupled by the cooling and repump light fields.

3.3.1. Second order correlation function of atomic systems

The coherence properties of light are usually defined with the help of the first and second order correlation functions. Using the quantum mechanical field operators $\hat{\mathbf{E}}^+$ and $\hat{\mathbf{E}}^-$, the first order correlation function is given by

$$g^{(1)}(\tau) = \frac{\langle \hat{\mathbf{E}}^-(t)\hat{\mathbf{E}}^+(t+\tau)\rangle}{\langle \hat{\mathbf{E}}^-(t)\hat{\mathbf{E}}^+(t)\rangle}. \tag{3.17}$$

The brackets $\langle...\rangle$ define the mean value of the inclosed expression over time. This function describes the coherence properties of the light field typically observed in interferometric setups.

---

[2]The survival probability for the "dark" trap at time zero is less than one. This is due to our measurement scheme, where a non-negligible probability exists that the atom is lost during the initial or final fluorescence detection, which then gives the wrong result.

Intensity correlations of a given light field at the times t and $t + \tau$ are described by the second order correlation function $g^{(2)}(\tau)$ that is defined by

$$g^{(2)}(\tau) = \frac{\langle \hat{\mathbf{E}}^-(t)\hat{\mathbf{E}}^-(t+\tau)\hat{\mathbf{E}}^+(t+\tau)\hat{\mathbf{E}}^+(t)\rangle}{\langle \hat{\mathbf{E}}^-(t)\hat{\mathbf{E}}^+(t)\rangle^2}. \tag{3.18}$$

The correct order of the electric field operators in eqn (3.18) can be obtained from considering that the joint detection of a photon at time t and a second photon at time $t + \tau$ is described by the expression $|\langle n - 2|\hat{\mathbf{E}}^+(t+\tau)\hat{\mathbf{E}}^+(t)|n\rangle|^2$ where $|n\rangle$ describes the number of photons in a given mode [80].

In the photon picture the $g^{(2)}$-function can be interpreted as the probability of detecting a photon at time $t + \tau$ conditioned on a previous detection of a photon at time t, normalized by the probability of detecting a photon in steady state. While for classical fields the relation $\langle I(t)^2\rangle \geq \langle I(t)\rangle^2$ – derived from Cauchy's inequality – assures that $g^{(2)} \geq 1$ for all times τ, this is not true for a single quantum emitter (e.g. a single atom). Because it can only emit a single photon per time, the correlation function can take values of $g^{(2)}(\tau) < 1$, which is the so-called photon-antibunching.

Photon statistics of a two-level atom

Consider the case of a single two-level atom at position $\mathbf{r_0}$ in a monochromatic light field. The corresponding electric field consists of three contributions: the vacuum state, the exciting light field and the atomic fluorescence light. Analyzing the light field at position $\mathbf{r}$ – far away from the exciting laser beam – only the atomic fluorescence light contributes to the measured correlation function. In the far field, the electric field of the fluorescence light in the Heisenberg picture is given by the expression [80]

$$\hat{\mathbf{E}}^+(\mathbf{r}, t) = -\frac{e\omega_0^2 d_{eg}\sin\theta}{4\pi\epsilon_0 c^2|\mathbf{r} - \mathbf{r_0}|}\mathbf{e}\hat{\pi}\left(t - \frac{|\mathbf{r} - \mathbf{r_0}|}{c}\right), \tag{3.19}$$

where $d_{eg} = \langle e|\hat{\mathbf{d}}|g\rangle$ is the dipole matrix element of the atomic transition with the resonance frequency ω_0 and θ describes the angle between the atomic dipole $\hat{\mathbf{d}}$ and the observation direction. The operator $\hat{\pi}$ shifts the atom from the excited state to the ground state and $\hat{\pi}^\dagger$ describes the reverse process. In the far field, the scattered light is transversely polarized along the unit vector $\mathbf{e}$, given by the projection of $\hat{\mathbf{d}}$ onto the plane perpendicular to the observation direction. Using eqn (3.19) and restricting us to the case of one polarization the second order correlation function can be directly expressed by the atomic transition operators $\hat{\pi}$ and $\hat{\pi}^\dagger$:

$$g^{(2)}(\tau) = \frac{\langle \hat{\pi}^\dagger(t)\hat{\pi}^\dagger(t+\tau)\hat{\pi}(t+\tau)\hat{\pi}(t)\rangle}{\langle \hat{\pi}^\dagger(t)\hat{\pi}(t)\rangle^2}. \tag{3.20}$$

Because we are interested only in the steady state value of $g^{(2)}$, the time retardation $|\mathbf{r} - \mathbf{r_0}|/r$ is ignored. In order to calculate $g^{(2)}(\tau)$ one has to evaluate the two-time expectation value in the numerator of eqn (3.20) with the help of the quantum regression theorem [81]. From the calculation one obtains [59]

$$g^{(2)}(\tau) = \frac{\rho_{ee}(\tau)}{\rho_{ee}(\infty)}, \tag{3.21}$$
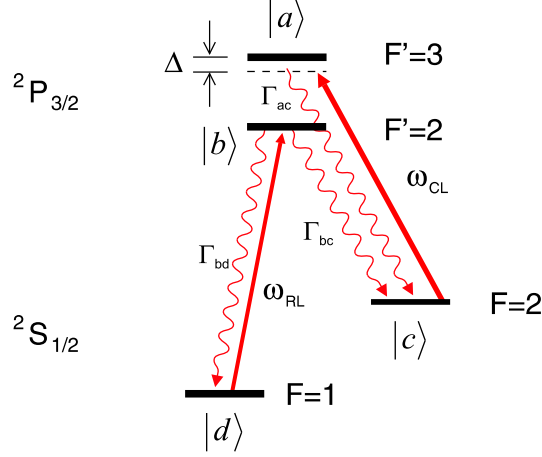
Figure 3.9.: Simplified levelscheme of the laser cooling process [68] (neglecting the Zeeman substructure), with the excited states $|a\rangle$ and $|b\rangle$ and the atomic ground states $|c\rangle$ and $|d\rangle$. The cooling transition $F = 2 \rightarrow F' = 3$ is driven by the cooling laser Ω_{ac} with 10 times the saturation intensity. Off-resonant excitation to the $F' = 2$ level (Ω_{bc}) gives rise to a decay channel to the $F = 1$ ground state. The repump laser (Ω_{db}) resonant to the transition $F = 1 \rightarrow F' = 2$ transfers population back from the $F = 1$ level into the cooling transition. The three possible decay channels are Γ_{ac}, Γ_{bc} and Γ_{bd}.

that only depends on the excited state population ρ_{ee} of the atom at time τ and in the steady state case ($\tau = \infty$). An intuitive interpretation of eqn (3.21) can be given in the photon picture where the possibility to detect a photon is proportional to the decay probability of the excited state of the atom and thus to the excited state population. For given experimental parameters the correlation function can easily be calculated using e.g. the optical Bloch equations with the initial condition, that at $\tau = 0$ the atom is in the ground state.

Photon statistics of a four level atom

In our experiment we analyze the photon statistics in a light configuration consisting of the cooling and repump light field. Thus, the above assumption of a two-level system is not valid and – ignoring off-resonant excitation of the repump laser – the incident light field couples four different hyperfine levels of ^{87}Rb (see Fig. 3.9). The complete description of the internal dynamics of a laser-cooled atom is quite difficult due to the complicated intensity and polarization pattern in space, created in the intersection region of the cooling and the repump

light. Due to the finite kinetic energy corresponding to a temperature of approximately 100 μK (see next chapter), the motion of the atom can be approximated by a classical oscillator with an amplitude of several optical wavelengths. During the oscillation, the atom experiences both, a change in intensity and polarization. This situation suggests to simplify the internal atomic dynamics by neglecting the Zeeman substructure of the atom and treating the exciting cooling and repump light fields as unpolarized. This allows to describe the atom by a four-level system and the incident light as unpolarized with a total intensity given by the sum of the three counterpropagating beam pairs. Using these assumptions one can solve the equation of motion for the 4×4 atomic density matrix ρ given by

$$\dot{\rho} = -\frac{i}{\hbar}[\hat{H}_{ED}, \rho] + R \tag{3.22}$$

with the Hamiltonian $\hat{H}_{ED}$ in the rotating wave approximation and the relaxation term R (see Appendix A.1.4). Analog to a two level atom (eqn (3.21)) the second order correlation function of the four-level system with the excited states $|a\rangle$ and $|b\rangle$ reduces to [82]

$$g^{(2)}(\tau) = \frac{\rho_{aa}(\tau) + \rho_{bb}(\tau)}{\rho_{aa}(\infty) + \rho_{bb}(\infty)}. \tag{3.23}$$

To obtain the $g^{(2)}(\tau)$ function we numerically solve the equation of motion for the atomic density matrix with the initial condition of an emitted photon at $\tau = 0$. Because we do not distinguish from which transition the first photon of a pair event was emitted, the initial atomic populations are calculated from the steady state solution. (For a more detailed discussion see [68].)

3.3.2. Hanbury-Brown Twiss measurement

The measurement of the second order correlation function requires the possibility to detect the difference of arrival times of the emitted photons. The avalanche photo diodes used for single photon detection have a dead time of about one μs. Thus, a direct measurement of the $g^{(2)}(\tau)$ function using only one APD is not possible at the interesting time region of the atomic lifetime (26 ns). This problem can be avoided using a Hanbury-Brown Twiss setup [79] (see Fig. 3.10) where the incoming fluorescence is sent on a 50/50 beamsplitter. An APD in each output port of the beamsplitter is used to detect the single photons and a storage oscilloscope measures the time difference $\tau = t_1 - t_2$ between detection events in each of the two detectors. For small time differences τ (much smaller than the mean time difference between two detection events) the normalized distribution of time differences obtained with this setup is equivalent to the second order correlation function $g^{(2)}(\tau)$ [83]. A detection event in APD$_1$ serves as a start event initializing the measurement and a detection event in APD$_2$ stops the measurement and the time difference τ is recorded into a histogram. To minimize background contributions coincidences are acquired only, when the fluorescence from the trap exceeds a threshold level of 1200 counts/s, indicating the presence of a single atom inside the trap.

Measurement results

The Hanbury-Brown Twiss measurement yields a histogram of time differences $\tau = t_1 - t_2$. Using the correct normalization factor n this histogram is equal to the second order correlation
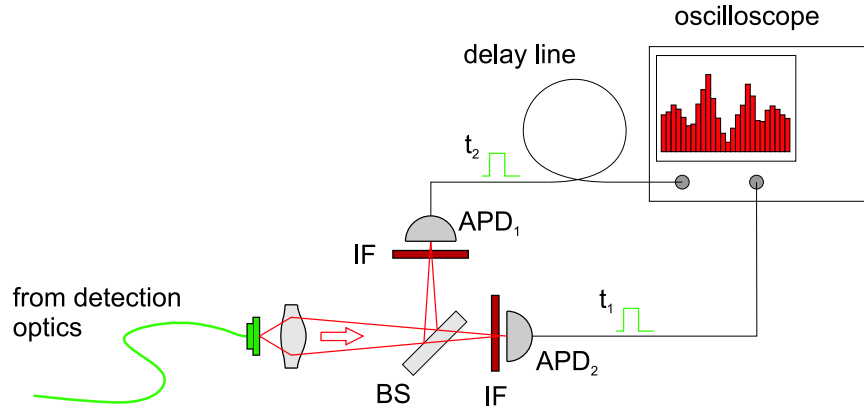
Figure 3.10.: Hanbury-Brown Twiss setup [79] for the measurement of the second order correlation function of the atomic fluorescence light. A 50/50 beamsplitter sends the incoming fluorescence onto two avalanche photo diodes. A storage oscilloscope histograms the differences of detection times $\tau = t_1 - t_2$ of photon pair events. Due to electronical reasons one of the two detection signals is delayed using a 70 ns delay line.

function [83]. The factor n can be calculated from the steady state probabilities of each detector to detect a photon in the time resolution window $\Delta\tau$ of the measurement apparatus and is given by

$$n = r_1 \times r_2 \times \Delta\tau \times T_{meas}, \tag{3.24}$$

where r_1 and r_2 are the mean count rates of two detectors and T_{meas} is the total measurement time of the experiment.

The measured pair correlation function $g^{(2)}(\tau)$ in Fig. 3.11 shows two interesting timescales. On a μs timescale the correlation function shows an exponential decay from the maximum value 1.24 at $\tau = 0$ to the large timescale value of 1 with a time constant of 1.8 μs (two orders of magnitude larger than the atom lifetime). The reason for this long time behavior is the diffusive motion of the atom in the intensity modulated light field at the intersection region of the three dimensional cooling beam configuration [84]. The combined field of the three retroreflected cooling beams gives rise to an optical grating superimposed to the "normal" cooling light field. In this grating, there is a higher probability for the atom to emit a photon when it is located at a node compared to the case where it is located at an antinode. Thus, the detection of a photon indicates the presence of the atom at a node of the light field and the probability to see a second photon shortly after the first detection is increased compared to the long time average. The decay time of this enhanced fluorescence probability corresponds to the diffusion time of the atom in the optical molasses, i.e. the time, after which the position of the atom – initially at the node of the grating – is distributed over a period of the optical grating.

On a short timescale, the correlation function shows a minimum value of $g^{(2)}(0) = 0.52\pm0.14$. Taking into account accidental coincidences due to the dark count rate of 300 s^{-1} of each
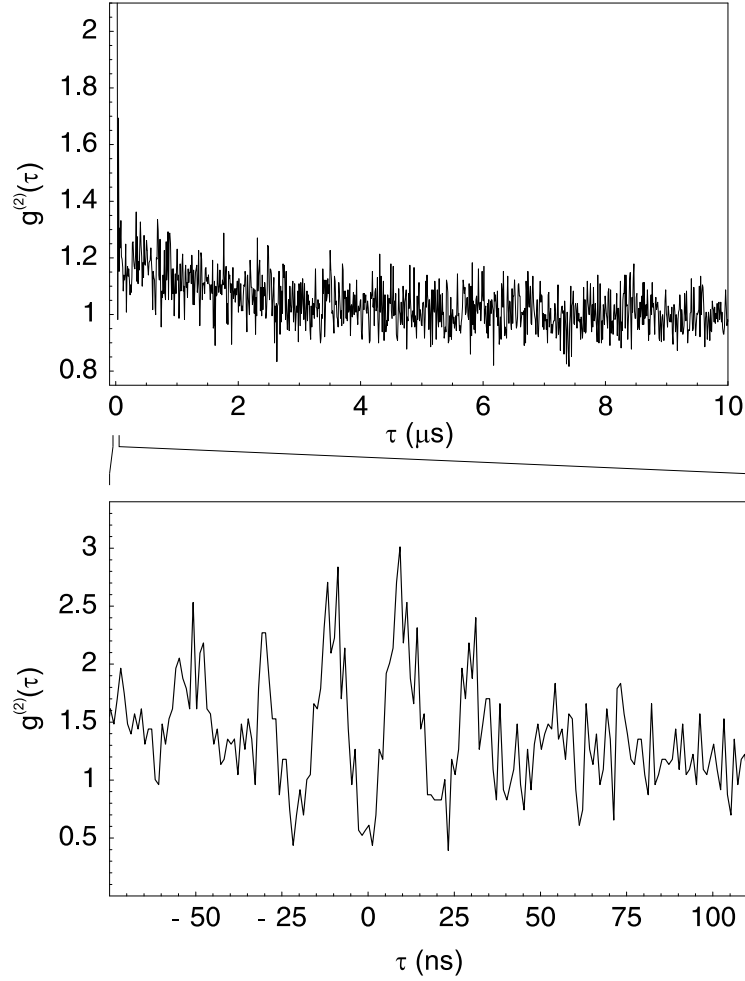
Figure 3.11.: Second order correlation function $g^{(2)}(\tau)$ measured for a dipole trap depth of 0.38 ± 0.04 mK and a cooling laser intensity and detuning of $I = 103$ mW/cm^2 (total intensity from all 6 cooling beams) and $\Delta = -31$ MHz, respectively. On a long timescale (upper picture) a small "bunching" effect can be seen which disappears exponentially with a time constant of $\tau = 1.8$ μs. On a short timescale $g^{(2)}(\tau)$ shows an oscillatory behavior caused by Rabi flopping of the atom with a decay time corresponding to the atomic lifetime. For $\tau = 0$ the correlation function shows a clear signal of photon antibunching.

detector, we derive a corrected minimum of 0.02 ± 0.14 compatible with perfect photon anti-bunching of the atomic fluorescence light. Therefore, only single photons are emitted from the trap region which proves that only a single atom can be present inside the dipole trap.

Furthermore, the oscillatory behavior of the $g^{(2)}$-function around $\tau = 0$ in the measurement in Fig. 3.11 is a signature of the Rabi-oscillations of the atom in the cooling light, where the frequency and damping rate are in good agreement with our experimental parameters (laser intensity and detuning). However, the amplitude of the oscillations is clearly above the maximally allowed value of 2 for a two level atom. Thus, we have to take into account all four atomic hyperfine levels coupled by the cooling laser system (see Fig. 3.9). In order to include the effects of the intensity variations of the light field, the calculated $g^{(2)}(\tau)$ function is multiplied by the expression $1 + Ae^{-k\tau}$ obtained from a fit to the measured correlation function on the μs timescale.

In order to compare the theoretical correlation function with the measured data we have to correct the measurement results for accidental coincident events caused by the background counts of the APDs. Splitting up the measured count rates $n_i = s_i + d_i$ of the two detectors $i = 1, 2$ into signal s_i (number of detected fluorescence photons per second) and dark count rates d_i, the background-corrected correlation function $g_c^{(2)}(\tau)$ is obtained from the measured function $g^{(2)}(\tau)$ by the transformation

$$g_c^{(2)}(\tau) = \frac{1}{s_1 s_2} \left(n_1 n_2 g^{(2)}(\tau) - d_1 d_2 - d_1 c_2 - c_1 d_2 \right). \tag{3.25}$$

The correlation function $g_c^{(2)}(\tau)$ obtained from this procedure is plotted in Fig. 3.12 together with the theoretical function derived from a numerical calculation for our experimental parameters. The calculated correlation function is in good agreement with the measured data while a simple two-level model with a maximum value of 2 can not explain the amplitude of the observed oscillations[3].

Analyzing the second order correlation function allowed us to gain information on the internal as well as the external atomic dynamics. Furthermore, the observation of perfect photon-antibunching provides a strong evidence for the collisional blockade effect and the single atom character of our dipole trap system, especially, if we take into account the measurements presented in chapter 3.2.2. Therefore, we can rely on the fact that the collisional blockade mechanism ensures that only single atoms are present in the optical dipole trap.

3.4. Kinetic energy of the single atom

The blockade effect and the resulting single atom characteristic of our dipole trap presented in the preceding chapter simplifies the generation of entanglement between a single atom and

---

[3]The observed fluorescence for the most part is emitted from the cooling transition. Off resonant excitation transfers population to the $F = 1$ ground state. Due to the small intensity of the repump light, the population of this level is only slowly transfered back into the cooling cycle. Thus, the presence of the $F = 1$ ground level reduces the long time average of the fluorescence rate while the short timescale fluorescence is dominated by scattering from the cooling light. Thus, we observe a higher value of the $g^{(2)}(\tau)$ correlation function around $\tau = 0$
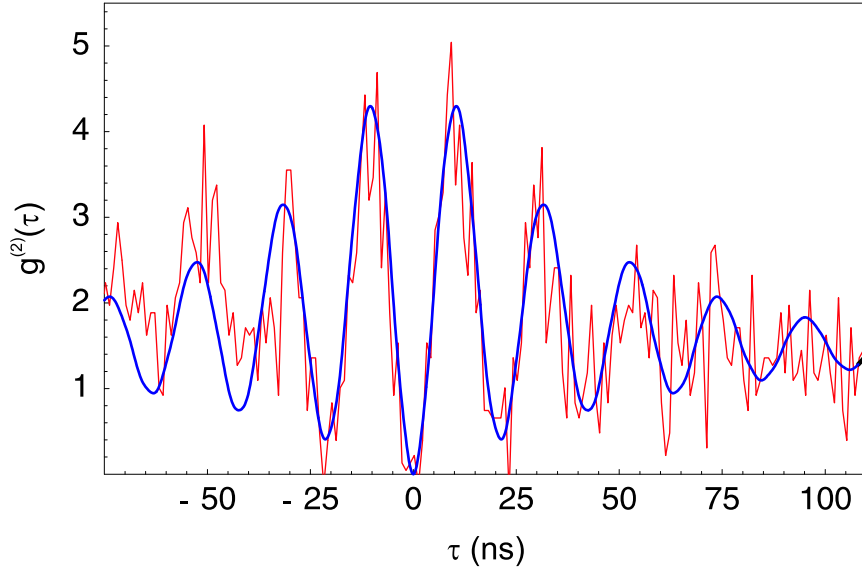
Figure 3.12.: Measured (red curve) and calculated (blue curve) second order correlation function. The theoretical correlation function was numerically calculated for a four level system with our experimental laser parameters [68]. For comparison, the measured data was background correct using the known dark count and signal rates of the photo detectors.

a single photon in an outstanding manner. However, another important characteristic for future experiments is the spectral distribution of the emitted light field, directly connected to the mean kinetic energy of the trapped atom. Depending on the position inside the dipole trap, the atom experiences different light shifts. Thus, an effective incoherent broadening of the spectrum of the spontaneously emitted photon is expected. Considering an interference experiment with two photons from two different atoms or emission processes, the finite atomic temperature results in different spectral distribution of the photons. This gives rise to the possibility to distinguish them and therefore reduces the contrast of two-photon interference experiments [85].

Analyzing the spectral properties of the light scattered by a single atom offers a powerfull way to infer effects of the atomic motion in the dipole trap and thus allows to estimate the kinetic energy of the atom. The resonance fluorescence spectrum has been investigated in a number of experiments analyzing either the fluorescence of neutral atoms in atomic beams [86, 87, 88, 89, 90], atomic clouds [91, 92] or single trapped ions [93, 94, 95], thereby verifying the so-called Mollow triplet [96] and the subnatural linewidth of elastic Rayleigh scattering.

In our experiment a single trapped ^{87}Rb atom is laser cooled resulting in a residual temperature on the order of the Doppler temperature of Rubidium of 146 μK [75]. Due to the Doppler effect the finite atomic temperature gives rise to a broadening of the scattered light. We measure the spectrum of the elastic component of the atomic fluorescence light with a

47

scanning Fabry-Perot resonator. Comparing the spectral width with the spectrum of the exciting cooling laser allows to determine the mean atomic velocity and thus the kinetic energy of the single atom.

3.4.1. Resonance fluorescence

A typical experiment analyzing the properties of resonance fluorescence starts with an atom inside a scattering region and a detector at a certain distance and angle, measuring the power spectrum of the scattered light field. In quantum mechanics the scattering of light is a second order process consisting of the absorption of a photon at frequency ω and the subsequent emission of a photon at frequency ω_{sc}. In general two possible types of processes occur. If the frequency of the emitted photon is equal to the frequency of the exciting light field ($\omega = \omega_{sc}$) the process is called elastic Rayleigh (coherent) scattering. Whereas the other type – inelastic (incoherent) scattering – includes all processes where the frequency of the scattered light field differs from the exciting light.

Coherent and incoherent scattering

In order to get an expression for the spectral distribution of the scattered light field of a two-level atom, it is convenient to divide the scattered light into a coherent and an incoherent contribution. Information on the first-order coherence of the scattered light is obtained by comparing the mean intensity of the scattered field and the square of the mean field. The ratio of the intensity of the first order coherently scattered light to the total intensity, can be described as [96]

$$R_{coh} = \frac{\bar{I}_{sc}^{coherent}}{\bar{I}_{sc}} = \frac{\langle \hat{\mathbf{E}}_{sc}^-(\mathbf{r},t)\rangle\langle \hat{\mathbf{E}}_{sc}^+(\mathbf{r},t)\rangle}{\langle \hat{\mathbf{E}}_{sc}^-(\mathbf{r},t)\hat{\mathbf{E}}_{sc}^+(\mathbf{r},t)\rangle}. \tag{3.26}$$

For purely coherent scattering this ratio reaches unity. Equation (3.19) connects this ratio to the occupation of the internal states of the scattering atom. Using the solutions of the optical Bloch equations for a two level atom we obtain in the steady state [96]

$$R_{coh} = |g^{(1)}(\infty)| = \frac{|\rho_{eg}(\infty)|^2}{\rho_{ee}(\infty)}, \tag{3.27}$$

where $\rho_{ij}(\infty)$ are the steady state elements of the atomic density matrix and $g^{(1)}(\tau)$ is the first order correlation function defined in eqn (3.17). From the steady state solutions in eqns (A.30) and (A.31) we obtain for the fraction of coherently scattered fluorescence light

$$R_{coh} = \frac{\Delta^2 + (\Gamma/2)^2}{\Delta^2 + (\Gamma/2)^2 + \Omega^2/2}, \tag{3.28}$$

where $\Delta = \omega_0 - \omega$ describes the detuning of the frequency ω of the driving field from the atomic resonance frequency ω_0. The values Γ and Ω are the transition linewidth and Rabi-frequency, respectively. For weak light fields $\Omega \ll \Gamma$ or large detuning $\Omega \ll |\Delta|$ the scattered light is mostly coherent. Only close to the atomic resonance the fraction of coherently scattered light gets smaller and a considerable part of the light is incoherent.
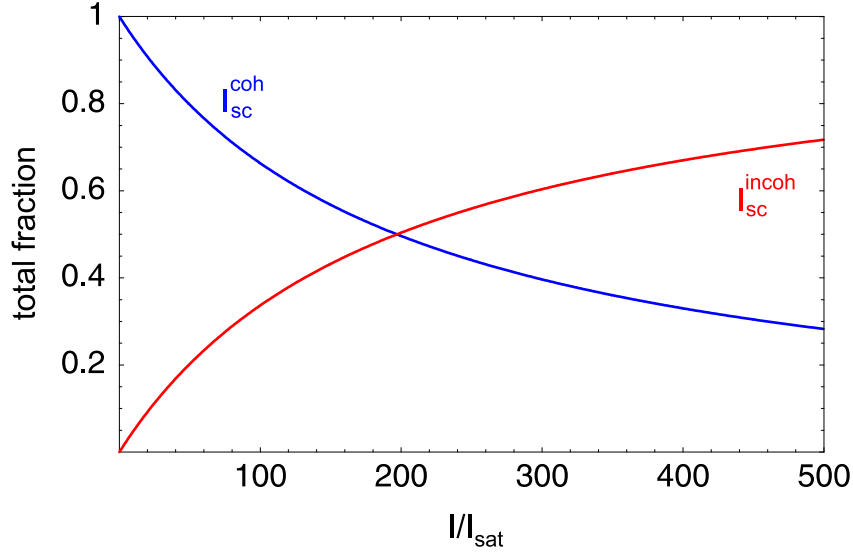
Figure 3.13.: Fraction of the coherent and incoherent part of the scattered light field as function of the intensity of the excitation light (in saturation intensities) for the approximate detuning of $\Delta = 7\Gamma$ inside the dipole trap. For small excitation intensities essentially all scattered light is coherent, whereas for high intensities incoherent scattering dominates.

Spectral properties of the scattered light

The coherent and incoherent part of the scattered light field differ in their spectral distribution. To compare their spectral distributions we need the power spectrum $f(\omega)$ of the fluorescence light that can be obtained from the first order correlation function by [96]

$$f(\omega_{sc}) = \frac{1}{2\pi} \int\limits_{-\infty}^{\infty} d\tau g^{(1)}(\tau) e^{-i\omega_{sc}\tau}. \tag{3.29}$$

The correlation function $g^{(1)}(\tau)$ can be separated into two contributions, describing the coherent and incoherent part of the light, respectively. The part corresponding to coherent scattering can (according to eqn (3.27)) be written as

$$g^{(1)}_{coh}(\tau) = e^{-i\omega\tau} g^{(1)}(\infty) = e^{-i\omega\tau} R_{coh} \tag{3.30}$$

and the corresponding Fourier transform is easily obtained. In order to obtain the full power spectrum including both, coherent and incoherent scattering, one can solve the optical Bloch
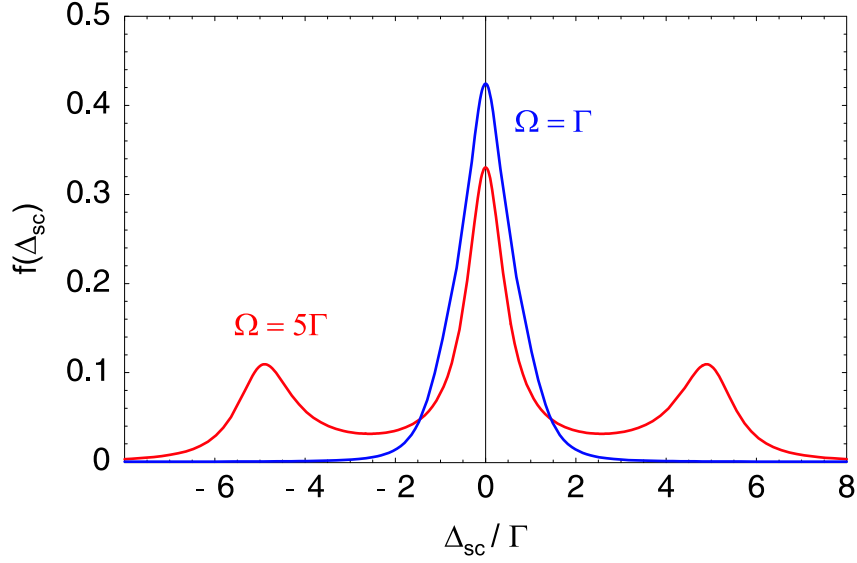
Figure 3.14.: Incoherent part of the fluorescence spectrum for resonant scattering ($\Delta = 0$) for two different Rabi frequencies $\Omega = \Gamma$ and $\Omega = 5\Gamma$. At low excitation power the spectrum consists only of a single peak centered at the laser wavelength. For stronger driving fields two side bands appear at the positions $\omega \pm \Omega$.

equations for a two-level atom and obtains [96, 88]

$$f(\omega_{sc}) = \quad R_{coh}\delta(\Delta_{sc}) + \frac{\Gamma\Omega^2\rho_{ee}^\infty}{2\pi} \frac{\Delta_{sc}^2 + \Omega^2/2 + \Gamma^2}{\Gamma^2[\Omega^2/(4\rho_{ee}^\infty) - 2\Delta_{sc}^2]^2 + \Delta_{sc}^2[\Omega^2 + \Delta^2 + \frac{5}{4}\Gamma^2 - \Delta_{sc}^2]^2}. \quad (3.31)$$

The frequency difference between the emitted photon with frequency ω_{sc} and the absorbed photon (frequency ω) is $\Delta_{sc} = \omega_{sc} - \omega$, and the steady state excited state population is given by

$$\rho_{ee}^\infty = \frac{\Omega^2/4}{\Omega^2/2 + \Delta^2 + \Gamma^2/4}. \quad (3.32)$$

In eqn (3.31) there are two distinct terms. The first term describes the power spectrum of fluorescence light that shows first-order coherence. The coherent part has the same frequency as the (monochromatic) exciting light field, and the spectrum is described by a δ-function. Therefore, this process is also referred to as elastic (Rayleigh) scattering. The spectral distribution of the incoherent part – given by the second term in the eqn (3.31) – differs from the driving frequency and thus is called inelastic. Figure 3.14 shows the inelastic spectrum for the case of resonant excitation. For high laser powers the inelastic spectrum consists of three peaks, one located at the laser frequency ω and two side-bands at the positions $\omega \pm \Omega$, the so-called Mollow-triplet.
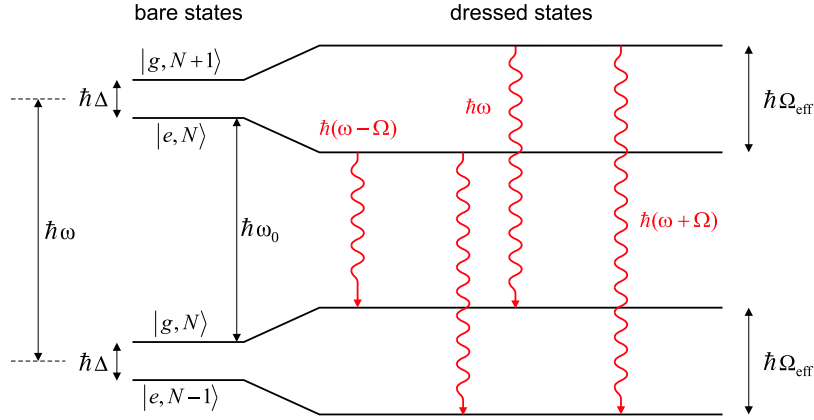
Figure 3.15.: Possible transitions of a two-level atom interacting with a quantized radiation field in the near resonant case $\Delta = \omega - \omega_0 \approx 0$. In the dressed state picture new energy eigenstates are formed which are superposition of the bare atomic ground and excited states $|g\rangle$ and $|e\rangle$ and the states of the light field with the photon numbers $|N\rangle$ and $|N \pm 1\rangle$. Four possible decay channels appear with the transition frequencies ω and $\omega \pm \Omega_{eff}$.

The occurrence of side-bands in the inelastic spectrum can be explained considering the possible decay channels in the combined physical system, consisting of the quantized monochromatic laser field and a two-level atom (see Fig. 3.15). In the dressed state picture eigenstates of the combined atom-photon Hamiltonian are products of the bare atomic states $|e\rangle$ and $|g\rangle$ and the photonic states $|N\rangle$ and $|N \pm 1\rangle$ (where N defines the mean photon number). If the frequency of the incident light is near resonant ($\Delta \approx 0$) the bare (undressed) states $|g, N + 1\rangle$ and $|e, N\rangle$ and the states $|g, N\rangle$ and $|e, N - 1\rangle$ are nearly degenerate and new eigenstates are generated, separated by the effective Rabi frequency $\Omega_{eff} = \sqrt{\Omega^2 + \Delta^2}$. Thus, the atom-field interaction generates four non-degenerate eigenstates with the possible transition frequencies ω and $\omega \pm \Omega_{eff}$.

3.4.2. Experimental setup

We analyze the spectral properties of the light scattered in the laser cooling process. The finite temperature of the atom gives rise to the Doppler effect, resulting in a spectral broadening of both, the elastically and inelastically scattered light. Due to its smaller spectral width, the Doppler broadening is most dominant for the elastically scattered part of the fluorescence light.

In our experiment the atom is excited by the cooling and repump laser field with a spectral width of approximately 700 kHz [21] – one order of magnitude smaller than the natural linewidth of the atomic transition (6 MHz). Thus, the subnatural linewidth of coherent scat-
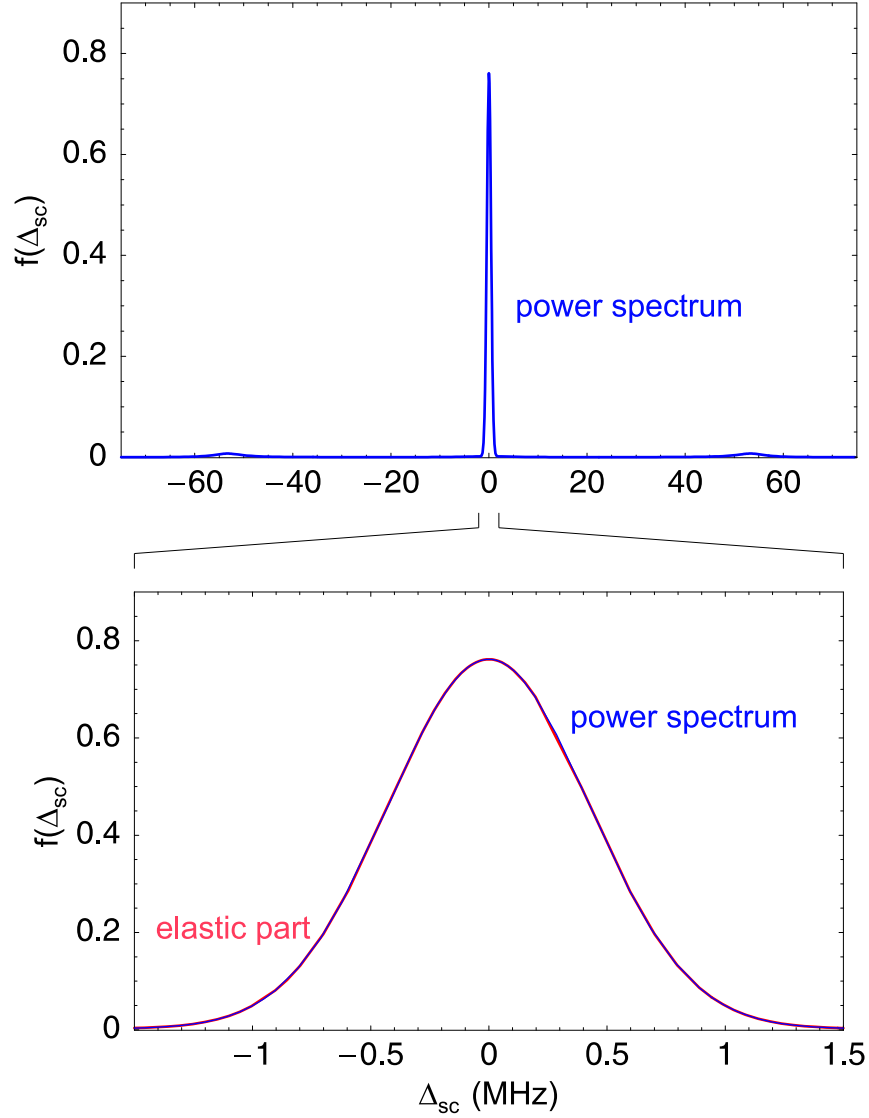
Figure 3.16.: Expected power spectrum for our experimental parameters ($\Delta = -19$ MHz, $I_{CL} = 87$ mW/cm^2, dipole trap depth 0.62 mK). The elastic part is plotted as a Gaussian function given by the convolution of the cooling laser spectrum with the experimental resolution of our spectrometer. The second plot shows the magnification of the central peak which is totally dominated by the elastically scattered light.

tering should be observable. Furthermore, the atomic power spectrum should be similar to the spectrum of a two-level atom, because most of the emitted photons are scattered from the cycling transition, driven by the cooling laser. For our experimental parameters (total detuning: 44 MHz, cooling laser intensity: 51 saturation intensities) 80% of the scattered light originates from coherent scattering (see eqn (3.28)). Therefore, the power spectrum – around the exciting laser frequency – is totally dominated by coherent (elastic) scattering and effects of inelastically scattered light can be neglected (see Fig. 3.14).

Scanning Fabry-Perot interferometer

Figure 3.17.: Setup for analyzing the spectral properties of the scattered light. A fraction of the cooling light (reference laser) and the atomic fluorescence are alternately analyzed with the same scanning Fabry-Perot interferometer with a length of 90 cm and a finesse of 375. A beamsplitter (BS) in front of the cavity reflects 50% of the incoming light onto an avalanche photo diode (APD$_1$) in order to restrict the measurement to the cases where an atom is present inside the dipole trap.

The power spectrum of the atomic fluorescence light is given by the spectrum of the cooling light with an additional broadening due to the Doppler effect. The power spectrum is measured during the laser cooling process, thus we expect a residual kinetic energy of the atom on the order of the Doppler temperature of Rubidium of 146 μK [75] and a corresponding spectral broadening of about 500 kHz. To obtain accurate measurement results, the spectrometer must have the capability to resolve this broadening. This condition can be fulfilled by a scanning Fabry-Perot interferometer (FPI). The small total scattering rate of about 1000 photons per

second gives high requirements on the transmission of the FPI that has to provide an adequate spectral resolution while at the same time a high transmission is necessary.

In the experiment, the FPI consists of two highly-reflective mirrors (radius of curvature 1000 mm, reflectivity 99.4%) with a spacing of $l = 90$ cm, resulting in a free spectral range of $\nu_{FSR} = 166$ MHz. One mirror is mounted on a piezo element to adjust the cavity length. The measured finesse $F = \nu_{FSR}/\Delta\nu = 375$ allows a spectral resolution of $\Delta\nu = 300$ kHz (FWHM). The on-resonance transmission of 44% is high enough to obtain the atomic fluorescence spectrum within a reasonable measurement time. The measurement accuracy strongly depends on the stability of the cavity length. Therefore, the cavity is mounted in an external tube for active temperature stabilization. During the measurement run, residual cavity length drifts are compensated in intervals of a few seconds.

For the spectral analysis, the photons scattered by the atom are collected by the microscope objective, coupled into the single-mode optical fiber and guided to the FPI. A 50/50 beam-splitter in front of the cavity reflects half of the photons onto an additional avalanche photo diode ($\mathrm{APD_1}$). An increase of the detected fluorescence on $\mathrm{APD_1}$ indicates the presence of a single atom inside the dipole trap and allows to restrict the measurement to the case where an atom is inside the trap.

In order to obtain the spectral broadening, the measured fluorescence spectrum has to be compared to the power spectrum of the incident cooling light. Therefore, a small part of the cooling light (reference beam) can be coupled into the optical fiber from the other side of the vacuum chamber (see Fig. 3.17). This allows to analyze both, the spectral properties of the cooling laser and the atomic fluorescence light with the same apparatus. Thus, no systematic errors due to different measurement techniques occur. Furthermore, the reference light allows to correct long time cavity length drifts.

3.4.3. Measurement process

Despite the temperature stabilization, still a non-negligible thermal drift in cavity length appears. In order to minimize the effect of these temperature drifts, the following measurement procedure is performed. First, a scan of the cavity length – using the reference beam – is performed to determine the position of cavity resonance. In the next step, the reference beam is switched off and the atomic fluorescence spectrum is measured by scanning the cavity across resonance. Finally, this procedure[4] is repeated to measure the reference beam spectrum in the same way.

Using this technique, systematic errors that occur from cavity length drifts between successive scans give the same contribution to both, the laser and the fluorescence spectrum. Because the calculation of the kinetic energy of the atom depends only on the frequency broadening of the atomic fluorescence it is insensitive to this error source. One experimental cycle therefore consists of four steps (determination of cavity resonance, fluorescence spectrum, determination of cavity resonance, laser spectrum) with a total cycle time of approximately 10 seconds. In order to obtain an adequate statistical error for the detected photon counts of the atomic fluorescence light we performed approximately 3000 measurement cycles.

---

[4]Determination of the cavity resonance and measurement of the power spectrum with the reference beam incident on the cavity.
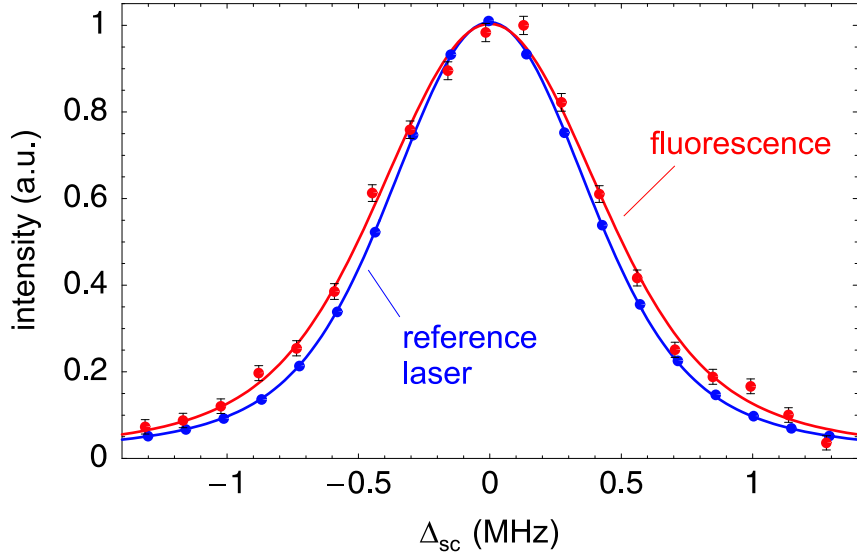
Figure 3.18.: Fluorescence (red) and cooling laser spectrum (blue). The figure shows the background corrected, normalized cavity transmission depending on the detuning Δ_{sc} of the cavity resonance from the cooling laser. The error bars show the statistical error of each data point. For the cooling laser spectrum this error is too small to be seen in this picture. The solid lines are fits of a Voigt profile to the measured data. The width (FWHM) of the fitted profile is 0.90 ± 0.01 for the cooling laser and 1.00 ± 0.02 for the atomic fluorescence, respectively.

The total fluorescence spectrum is obtained from the single measurement runs by adding up all measurement traces and normalizing each data point by the time an atom was present in the trap during the measurement. The cooling laser spectrum is obtained in a similar way, whereby each single run spectrum is independently normalized to ensure equal weighting. This procedure yields the data plotted in Fig. 3.18 showing the cooling laser and the atomic fluorescence spectrum. A clear broadening of the fluorescence spectrum compared to spectral distribution of the cooling light is observed.

3.4.4. Determination of the kinetic energy

The spectral broadening of the atomic fluorescence relative to the cooling light spectrum allows an estimation of the mean kinetic energy of the atom. The velocity distribution of the atom

in the dipole trap gives rise to a time dependent Doppler shift for the absorption and emission of a photon by the atom. For a quantitative estimation of this effect we assume an isotropic Gaussian velocity distribution of the atom[5] of

$$p(v) = \sqrt{\frac{m}{2\pi k_B T}} \exp\left(-\frac{mv^2}{2k_B T}\right), \tag{3.33}$$

where $p(v)$ is the probability to obtain the velocity v, k_B the Boltzmann constant and m and T correspond to the atomic mass and temperature, respectively. Due to the Doppler effect, a frequency shift $\Delta\nu = v/\lambda$ occurs during the absorption or emission of a photon. In general, the absorption (defined by the exciting laser beam) and emission direction (defined by the collection optics) are not perpendicular to each other but instead inclose an angle ϕ. Setting the the laser direction along the x-axis and the detection optics along the unit vector $\mathbf{e}_\phi = \cos\phi \cdot \mathbf{e_x} + \sin\phi \cdot \mathbf{e_y}$, the total frequency shift in an absorption-emission cycle is

$$\Delta\nu = \frac{\mathbf{e_x} \cdot \mathbf{v} + \mathbf{e}_\phi \cdot \mathbf{v}}{\lambda} = \frac{v_x(1 + \cos\phi) + v_y \sin\phi}{\lambda}, \tag{3.34}$$

where $\mathbf{e_x}$ and $\mathbf{e_y}$ are the unit vectors along the x-axis and y-axis with the corresponding atomic velocity components v_x and v_y, respectively. The probability distribution of the combined emission and absorption Doppler shifts $\Delta\nu$ can be calculated from integrating over all possible values of v_x and v_y yielding $\Delta\nu$ from which we obtain

$$p_\phi(\Delta\nu, T) = \sqrt{\frac{m\lambda^2}{4\pi(1 + \cos\phi)k_B T}} \exp\left(-\frac{m\lambda^2}{4k_B T(1 + \cos\phi)}\Delta\nu^2\right). \tag{3.35}$$

In our laser cooling configuration the atom is excited by light incident from three different directions. One beam is perpendicular to the detection axis while the other two are incident under an angle of 73° and 107°, respectively. The measured fluorescence consists of light scattered from the three light fields where the scattering from each beam gives rise to a different Doppler broadened spectrum. If we assume that the three beams have equal intensities at the position of the dipole trap, the atom should scatter an equal amount of photons from each beam. Thus, the resulting distribution of Doppler shifts is given by

$$p(\Delta\nu, T) = \tfrac{1}{3}\left[p_{0°}(\Delta\nu, T) + p_{73°}(\Delta\nu, T) + p_{107°}(\Delta\nu, T)\right]. \tag{3.36}$$

The atomic fluorescence spectrum can be described by the convolution of the power spectrum of the laser light with the distribution of Doppler shifts in eqn (3.36). In the measurement, the statistical error of the data points of the reference laser spectrum is two orders of magnitude smaller than the error for the fluorescence light. This allows to directly describe the fluorescence spectrum as the convolution

$$F(\Delta\nu, T) = \sum_i l_i \cdot p(\Delta\nu_i - \Delta\nu, T) \tag{3.37}$$

---

[5]We expect an atomic temperature on the order of the Doppler temperature of [87]Rb of 146 μK [75]. This is much larger than the energy difference between the dipole trap levels of approximately $k_B \cdot 0.9$ μK for the transversal and $k_B \cdot 0.05$ μK for the longitudinal trap axis. Therefore, the atomic motion can be treated classically and the kinetic energy distribution is given by the Boltzmann statistics.

of the measured and normalized laser spectrum with the distribution of Doppler shifts defined in eqn (3.36). Here the l_i define the measured spectral intensity at the detuning $\Delta\nu_i$ (relative to the cooling laser). The convolution $F(\Delta\nu, T)$ is fitted to the measured fluorescence spectrum with the atomic temperature T as a free parameter. From this fit we obtain the mean kinetic energy of the atom, which corresponds to a temperature of

$$T_{atom} = 105 \pm 25^{+15}_{-17}\mu\text{K}. \tag{3.38}$$

The first error in this equation includes the statistical error obtained from the fitting procedure ($\pm 12\ \mu\text{K}$) and the uncertainty in frequency calibration of the FPI ($\pm 13\ \mu\text{K}$). The other error is systematic and arises from the lack of knowledge how the scattering from each cooling beam contributes to the measured fluorescence spectrum. Because the exact intensity of the cooling beams at the position of the atom is not known exactly, and because each beam gives rise to a different Doppler broadening, a systematic error occurs in the calculation of the atomic temperature. To include this effect in the error consideration we calculated the maximum and minimum temperature in the extreme case where the atom scatters light from only one of the three beams. This procedure yields the last error in eqn (3.38).

The measured temperature of 105 μK is lower than the Doppler limit of ^{87}Rb of 146 μK [75], which is consistent with the cooling technique in our experiment, where in the presence of orthogonally circular polarized cooling beam pairs, sub-Doppler cooling mechanism should occur allowing final temperatures below the Doppler limit [74].

Implications on possible experiments

Spectral indistinguishability of photons is an important condition in many quantum interference experiments. Therefore, the mean kinetic energy is a crucial parameter because the finite atomic temperature gives rise to an incoherent broadening of the emitted light. In principle there are two broadening mechanisms. On the one hand, there is the direct broadening due to the Doppler effect (see eqn (3.34)) analyzed in our experiment. This broadening is small and can be ignored for most applications. A further broadening mechanism occurs in experiments requiring a deterministic emission of single photons. Therefore, the atomic population has to be transferred to the excited state by optical pulses shorter than the decay time of the atom. According to the uncertainty relation this gives rise to broad frequency spectrum of the incident light field. In this case the atom absorbs only frequency components resonant to the atomic transition and the spectrum of the fluorescence light is (in contrast to elastic scattering) defined by the absorption spectrum of the atom. Due to the position dependent light shift in optical dipole traps and the finite temperature of the atom, the atomic transition frequency changes over time which gives rise to an incoherent spectral broadening of the emitted light. Using the classical picture of a point-like atom oscillating in an harmonic potential, we obtain a distribution of atomic resonance frequencies with a spectral width of 4.4 MHz (FWHM) for the measured temperature of 105 μK. Hence, an effective incoherent line broadening occurs, one order of magnitude larger than the broadening due to the Doppler effect alone.

Now we consider the implications of this broadening on future applications as e.g. the generation of remote entangled atoms via entanglement swapping. In this process, two photons emitted from two different atoms are overlapped on a beam splitter. A coincidence detection of

one photon in each output mode corresponds to the detection of the photon Bell state $|\Psi^-\rangle$ and signifies the generation of entanglement between the atoms (see chapter 2.1.5). The incoherent broadening introduces the possibility to distinguish the photons by means of their spectrum and reduces the interference contrast and the fidelity of the generated entangled atom-atom state. However, for a time-resolved photon coincidence detection (duration of the photon "wavepacket" much larger than the time resolution of the detectors) it is still possible to retain perfect interference [85] by limiting the coincidence detection window to a certain delay time. Using the calculation outlined in [97] for the Lorentzian spectrum of the spontaneous decay and a Gaussian distribution of atomic resonance frequencies due to the finite temperature, a fidelity[6] of 99 % can be obtained for a coincidence window of 11 ns, however with the tradeoff of detecting only 34 % of the two-photon events.

3.5. Summary

This chapter described the setup of the optical dipole trap used for the storage of ^{87}Rb atoms. The detected fluorescence light shows the presence of a blockade mechanism that limits the maximum number of atoms in the trap to one. Measuring the second order correlation function of the atomic fluorescence in a Hanbury-Brown Twiss setup, we observed strong photon anti-bunching verifying the presence of only a single atom inside the trap. Furthermore, the measured correlation function shows effects of the internal and external dynamics of the atom in the cooling light field. The predictions of a four-level model were compared with the measured correlation function and within experimental errors we find good agreement of the calculated predictions with the measured data.

The measured power spectrum of the single atom resonance fluorescence is dominated by elastic Rayleigh-scattering. Due to the Doppler effect a broadening of the atomic fluorescence spectrum relative to the exciting cooling light is observed. From this broadening we determined the mean kinetic energy of the trapped atom corresponding to a temperature of 105 μK. For single photon emission, this finite temperature together with the inhomogeneous light shift of the dipole trap gives rise to an incoherent spectral broadening and thus to the possibility to distinguish photons from different emissions. If we perform a time resolved photon detection [85] this effect can be avoided by limiting the coincidence detection of the two photons to a time window of approximately 11 ns.

---

[6]Possibility to obtain the expected entangled atom-atom state, if a photon coincidence was detected.

4. Detection of atomic superposition states

Contents

Single atoms are a promising candidate for the storage of quantum information and allow the generation of an entangled state between defined Zeeman sublevels of the atom and the polarization of a spontaneously emitted single photon. While according to quantum mechanics the combined atom-photon state created in the spontaneous decay is entangled, this still remains to be verified. In order to show that the generated state is truly entangled, it is necessary to analyze correlations between the polarization of the emitted photon and the internal state of the atom in complementary measurement bases. While polarization measurements of photons can be performed in a straightforward way using polarizers aligned along certain axes, the measurement of the internal atomic state is more difficult. Analyzing the atomic state in different measurement bases requires the possibility to detect coherent superposition of specific atomic Zeeman sublevels. Therefore, an experimental scheme that allows the faithfull determination of the internal atomic superposition states is the crucial ingredient for the verification of atom-photon entanglement.

In our experiment the atomic state measurement is realized using a combination of coherent dark state projection together with a population transfer between the two hyperfine ground

levels of ^{87}Rb. Therefore, we make use of the so-called stimulated Raman adiabatic passage (STIRAP) technique that allows coherent population transfer between atomic levels by an adiabatic change of the intensity of the involved light fields [47, 48, 49, 50, 51, 52]. In the tripod-STIRAP scheme [98, 99, 100, 101] used in our experiment, the polarization of the STIRAP light fields determines which superposition of Zeeman sublevels will be transferred from the $F = 1$ to the $F = 2$ hyperfine ground level, thus defining the atomic measurement basis. In order to distinguish the two hyperfine levels, we use a hyperfine level detection scheme based on a variation of the shelving technique [102], that removes an atom in the $F = 2$ hyperfine ground level from the trap and, together with a final fluorescence detection, allows to read out the hyperfine level and thus the initial atomic superposition state.

The first part of this chapter describes the hyperfine level detection, that represents the basic detection scheme necessary for all atomic state measurements. The second part of the chapter gives a short introduction into dark states and coherent population trapping and their application in the STIRAP technique. The experimental realization of the population transfer is described and the conditions for high transfer accuracy are analyzed. The last part of this chapter describes an application of the superposition state detection scheme, where the STIRAP technique is used to observe the precession of the magnetic moment of a single atom in an external magnetic field.

4.1. Hyperfine level detection

The faithfull detection of hyperfine levels presents an essential part in the superposition state detection process, necessary for the verification of atom-photon entanglement. A method, widely used to determine the hyperfine level of trapped ions, is the so-called shelving technique [102]. There, the presence respective absence of resonance fluorescence gives information on the population of the various internal atomic states.

In our experiment shelving can not be applied for reasons discussed in the following chapter. Therefore, a different detection scheme is developed that circumvents the restrictions of the shelving technique for our experimental scheme. In this "two step detection" a projection laser acting as (atomic state selective) filter removes ^{87}Rb atoms in the $F = 2$ hyperfine ground level from the dipole trap. A subsequent fluorescence measurement provides the actual atomic state detection, yielding information about the initial hyperfine level population. This chapter describes the experimental realization of the hyperfine level detection process and its dependence on the intensity of the projection laser. Furthermore, the accuracy – i.e. the probability to correctly identify the atomic state – of this detection scheme is analyzed.

4.1.1. Two step detection scheme

The $5^2S_{1/2}$ ground level of ^{87}Rb consists of two hyperfine levels with total angular momentum $F = 1$ and $F = 2$. For circularly polarized light a closed transition from the $F = 2$, $m_F = 2$ Zeeman ground state to the excited state $5^2P_{3/2}$, $F' = 3$, $m_F = 3$ exists. In the standard shelving technique [102] light resonant to this transition is applied. An atom initially in a Zeeman sublevel of the $F = 2$ hyperfine ground level continuously scatters photons from this light field, whereas for an atom in the $F = 1$ ground level no coupling to the light field occurs

Figure 4.1.: ^{87}Rb term scheme for magnetic quantum numbers $m_F \geq 1$. (a) Cycling transition $|F = 2, m_F = 2\rangle \rightarrow |F' = 3, m_F = 3\rangle$ used for the fluorescence detection of the hyperfine ground level. An atom initially in the $F = 2$ level emits fluorescence light from the cycling transition, whereas no fluorescence is emitted if the atom is initially in the $F = 1$ ground level. (b) If the exciting laser light field is not perfectly circularly (σ^+) polarized, off-resonant excitation to the $F' = 2$ level will be possible and the atom can decay into dark $F = 1$ ground level.

and no fluorescence is emitted. Thus, the presence or absence of fluorescence light indicates wether the atom is in the $F = 2$ or $F = 1$ hyperfine ground level.

For an accurate hyperfine level detection, the atom must remain on the cycling transition during the whole detection process. Small polarization errors of the incident light field (or the precession of the atom in a residual magnetic field) lead to a non-vanishing probability of off-resonant excitation to the $5^2P_{3/2}$, $F' = 2$ level from which spontaneous decay into the $F = 1$ hyperfine ground level is possible (see Fig. 4.1). In this case the atom, initially in the "bright" (scattering) hyperfine level $F = 2$, is pumped into the $F = 1$ level and subsequently remains "dark".

In our experiment, the total detection efficiency for fluorescence photons is 0.1%. Thus, the atom would have to undergo 20,000 excitation-emission cycles (without decaying into the $F = 1$ ground level), to detect approximately 20 photons that are necessary to distinguish the atomic fluorescence from the background count rates of our detectors. Moreover, the incident shelving light has to be applied along one defined direction[1]. Hence, the scattering of photons

---

[1]Otherwise, non-circular polarization components would occur and the atom would not remain in the

gives rise to a radiation pressure force along the direction of the laser beam and a heating of the atomic velocity components perpendicular to direction of the shelving beam. For the shallow potential of optical dipole traps, this radiation pressure and heating mechanism lead to a loss of the atom from the trap [103]. Thus, the direct application of the shelving technique is not possible.

Two step detection

In order to circumvent the problems arising from the direct fluorescence detection we chose a different detection scheme. In this process the hyperfine level detection is realized in two steps (see Fig. 4.2):

1. A 6 μs long circularly polarized projection laser pulse – resonant to the cycling transition – is applied from one direction. An atom in the $F = 2$ hyperfine ground level scatters photons and acquires in average one additional photon momentum $\hbar\mathbf{k}_{photon}$ per scattering event. After approximately 50 scattering events the acquired linear momentum leads to a loss of the atom from the trap. The application of the projection pulse therefore corresponds to the use of a hyperfine level selective filter that gives two possible final results. Either, the atom is still in the trap and thus was initially in the $F = 1$ hyperfine level. Or the atom was removed from the trap by the projection pulse and thus was initially in the $F = 2$ ground level.

2. In order to distinguish the two possible outcomes (atom in the trap or not), the cooling and repump laser system of the MOT is switched on and the fluorescence from the dipole trap region is integrated for a certain time. If the number of detected fluorescence photons exceeds a certain threshold, this indicates the presence of an atom and allows to conclude that the initial hyperfine level was $F = 1$. If the observed fluorescence corresponds to the background rate of the APDs the atom was removed from the trap and thus was initially in the $F = 2$ ground level.

4.1.2. Experimental realization

In order to test the accuracy of the hyperfine level detection scheme, optical pumping prepares the atom in each of the two hyperfine ground levels $F = 1$ and $F = 2$ using an incident light field resonant to the transition $F = 2 \rightarrow F' = 1$ or $F = 1 \rightarrow F' = 1$, respectively (see Fig. 4.2). After the preparation, the hyperfine level detection is performed. Therefore, a projection laser pulse removes atoms in the $F = 2$ ground level from the trap and a subsequent fluorescence detection analyzes the presence of an atom in the trap. Figure 4.3 shows the distribution of the number of fluorescence photons measured in the second step of the detection process. The measurement shows two clearly distinguishable peaks for the cases in which the atom was prepared in the two different initial hyperfine levels. Defining a suitable threshold value of photon counts, we obtain the binary result "atom in the trap" or "no atom in the trap" and therefrom the information about the initial atomic hyperfine level $F = 1$ or $F = 2$, respectively.
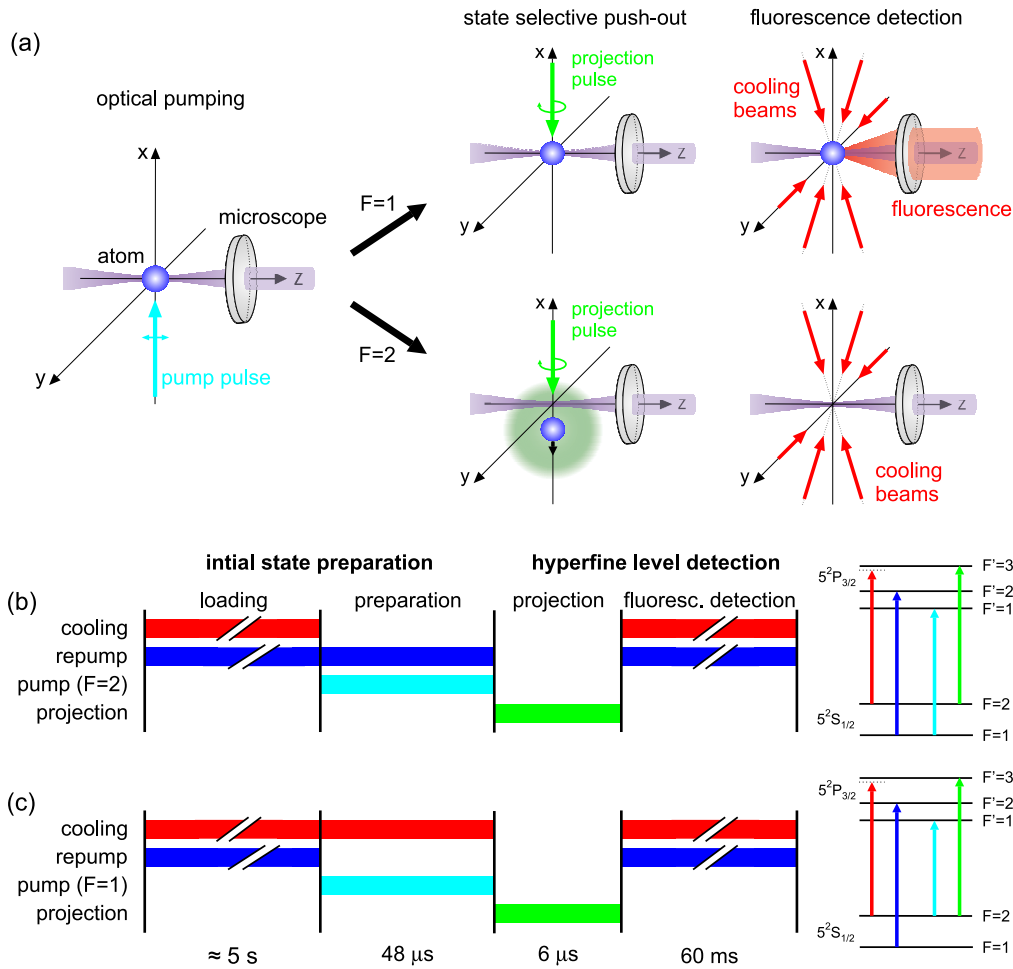
cycling transition (see Fig. 4.1).

Figure 4.2.: Laser system and timing sequence for the preparation and detection of hyperfine ground levels. (a) Arrangement and polarization of the incident laser beams. After the preparation of the atom in the initial hyperfine levels $F = 1$ and $F = 2$, a 6 μs circularly polarized projection pulse – resonant to the cycling transition $F = 2 \rightarrow F' = 3$ – removes atoms in the $F = 2$ ground state from the trap. In the final fluorescence detection stage, the cooling and repump lasers are switched on and the fluorescence is measured for 60 ms to decide if the atom is still in the trap or not. (b) and (c) Timing sequences of the experiment. (b) For the preparation of the initial hyperfine level $F = 2$, a 50 μs repump light pulse is applied together with a pump pulse resonant to the transition $F = 1 \rightarrow F' = 1$. (c) In order to prepare the atom in the $F = 1$ ground level another pump pulse – resonant to $F = 2 \rightarrow F' = 1$ – is used together with the cooling laser.
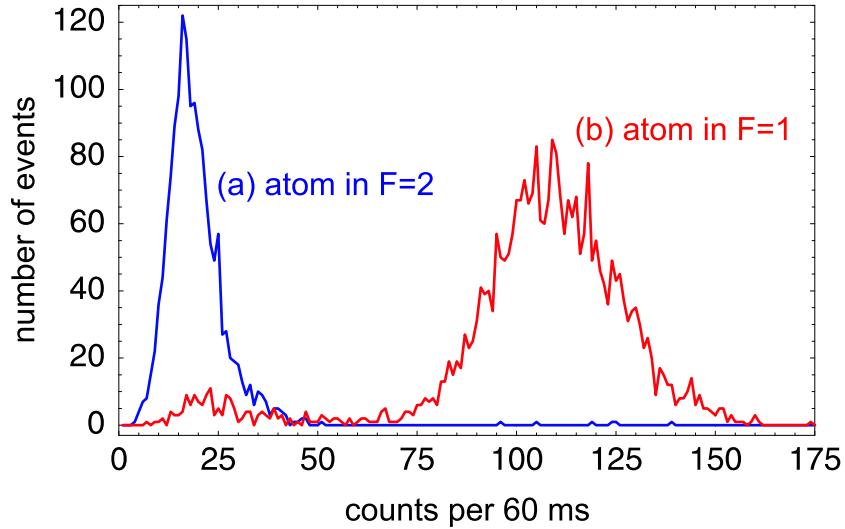
Figure 4.3.: Histogram of the measured fluorescence photons in the second step of the hyperfine level detection. (a) For atoms initially prepared in the $F = 2$ hyperfine level we observe fluorescence corresponding to the dark count rate of our photon detectors. (b) If the atom is prepared in the $F = 1$ hyperfine level, we observe fluorescence indicating the presence of an atom in the trap.

Parameters of the detection process

A crucial parameter in the atomic hyperfine level detection is the intensity of the projection light. For low intensities, the scattering rate is low and during the application of the projection pulse the atom does not acquire enough momentum to leave the trap. On the other hand, for high intensities power broadening of the atomic transition increases the probability of off-resonant excitation. Thus, optical pumping into the $F = 1$ hyperfine ground level gets more likely and the probability to remove the atom from the trap decreases. To optimize the light intensity, we measured the probability to detect the atom in the final fluorescence measurement as a function of the intensity of the projection light field for an atom initially prepared in the $F = 2$ hyperfine level (see Fig. 4.4). The probability to remove the atom from the trap is maximal for an intensity corresponding to approximately 20 saturation intensities, which therefore defines the optimal intensity for the projection pulse.
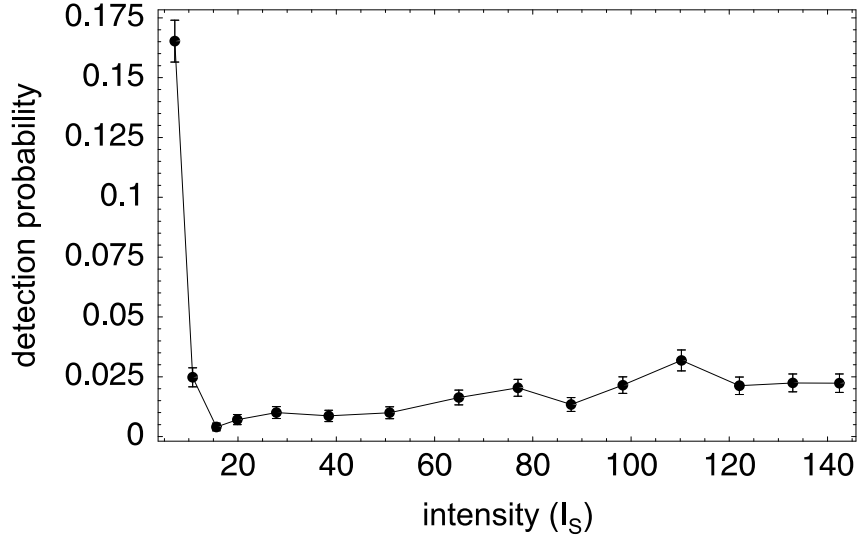
Figure 4.4.: Probability to detect the atom in the final fluorescence detection as a function of the projection laser intensity for atoms initially prepared in the $F = 2$ hyperfine level.

4.1.3. Accuracy of the detection process

For the verification of atom-photon entanglement, it is necessary to obtain a measure for the reliability of the hyperfine level detection. One way to quantify the quality of the detection process are the detection accuracies $a_{(F=1)}$ and $a_{(F=2)}$, i.e. the probabilities that the atomic hyperfine levels $F = 1$ and $F = 2$ are correctly identified. Therefore, we measured the detection probability of the atom in the final fluorescence detection with and without application of the projection pulse for an initial preparation in the $F = 2$ hyperfine level. Therefrom we derive the results in table 4.1.

		detection probability
1.	with projection pulse	$p_{det} = 0.70 \pm 0.2\%$
2.	without projection pulse	$p_0 = 96.3 \pm 0.2\%$

Table 4.1.: Probability to detect the atom (initially prepared in $F = 2$) in the final fluorescence measurement with (1) and without (2) application of the projection pulse.

In order to obtain the detection accuracy from these results we assume a simple model of the detection process. Initially, the atom is prepared in one of the two hyperfine levels with the success probability $p_{(F=1)}$ and $p_{(F=2)}$. After the preparation, the hyperfine level detection is performed with the two possible measurement outcomes:

1. The result *"no fluorescence"* is obtained if the atom was initially in $F = 2$ and was correctly identified in the detection process $(a_{(F=2)})$ or if the atom was initially in $F = 1$ and was incorrectly identified $(1 - a_{(F=1)})$, e.g. due to a collisional loss of the atom from the trap[2].

2. The result *"fluorescence detected"* is also obtained in two possible ways. Either, the atom was initially in the $F = 1$ hyperfine ground level and was correctly identified $(a_{(F=1)})$, or the atom was in $F = 2$ and was not removed from the detection beam $(1 - a_{(F=2)})$[3].

Using this model we can derive some lower bounds on the accuracy of the detection process. In the measurement without detection pulse the final detection probability is independent of the initial hyperfine level and the only loss mechanisms are collisions with background gas. Thus, we can directly calculate the detection accuracy $a_{(F=1)} = 96.3 \pm 0.2\%$ from the second measurement in table 4.1. The detection probability p_{det} in measurement 1 is given by the expression

$$p_{det} = p_{(F=1)}a_{(F=1)} + p_{(F=2)}(1 - a_{(F=2)}). \tag{4.1}$$

From this equation we can estimate the detection accuracy for the $F = 2$ hyperfine level: $a_{(F=2)} > 1 - p_{det} = 99.3 \pm 0.1\%$. Similar considerations also give a lower bound of the pump efficiency of $p_{(F=2)} > 99.3\%$. To summarize, the measured probabilities to correctly identify the hyperfine levels $F = 1$ and $F = 2$ are

$$a_{(F=1)} \quad > \quad 96.3 \pm 0.2\% \tag{4.2}$$
$$a_{(F=2)} \quad > \quad 99.3 \pm 0.1\%, \tag{4.3}$$

with an average accuracy of more than 97.8%.

The high accuracy in distinguishing atomic population in the two hyperfine levels $F = 1$ and $F = 2$ allows a highly reliable measurement of the population of the internal atomic levels. Therefore, this detection scheme provides us with an accurate and easy maintainable system for the analysis of atomic states. Especially for the detection of atomic superposition states, where it provides the mechanism for the read-out of the information about the atomic population.

4.2. Superposition state selective transfer

The hyperfine level detection in the preceding section provides a method to gain information about the population of atomic hyperfine levels. However, the verification of atom-photon

---

[2]This probability includes all possible trap loss mechanisms, including collisions or parametric heating due to power fluctuations of the trapping beam.

[3]This probability also includes events where e.g. a new atom enters the trap during fluorescence detection.

entanglement requires a measurement procedure that in principle allows to detect arbitrary superposition states of atomic Zeeman sublevels. A possibility to realize this is the combination of coherent dark state projection with the stimulated Raman adiabatic passage (STIRAP) technique [47, 48, 49, 50, 51, 52], that implements a superposition state selective population transfer between the atomic hyperfine levels. Together with the hyperfine level detection this allows the analysis of atomic superposition states in arbitrary measurement bases.

The following chapter gives a short introduction into coherent dark states and the STIRAP technique. Afterwards, the realization of a superposition state selective transfer using the tripod-STIRAP [98, 99, 100, 101] method is described. Here, the polarizations of the STIRAP light fields define which superposition of Zeeman sublevels will be transferred from the $F = 1$ to the $F = 2$ hyperfine ground level, thus defining the atomic measurement basis. In our experiment the STIRAP light fields are provided by two laser diodes, independently stabilized using Doppler-free saturation spectroscopy, from which we generate the STIRAP pulse sequence using AOMs. Finally, the transfer efficiency of defined superposition states for different STIRAP polarizations is analyzed and the accuracy of the superposition state detection is discussed.

4.2.1. Dark states and coherent population trapping

With the occurrence of lasers, (nearly) monochromatic light sources became available emitting light with coherence times from the nanosecond range up to several milliseconds. These coherent light sources offered the possibility to study many phenomena in atomic physics. One of these effects is the occurrence of dark states, which are internal atomic states that do not couple to an external light field. In principle different types of dark states exist. Negligible coupling can occur if the frequency of the external light is far off-resonant relative to possible atomic transitions or if the polarization of the incident light field is chosen such that selection rules of atomic dipole transitions are not fulfilled. Another important type of dark states is generated in the interaction with different light fields. If the incident light consists of two (or more) coherent field contributions, coherent dark states can be observed, where in spite of the incident light fields (even if they are resonant to an atomic transition) no excitation occurs.

Coherent dark states play an important role in the stimulated Raman adiabatic passage scheme that provides a robust method for the transfer of atomic populations from one internal atomic state to another [47, 48, 49, 50, 51, 52]. This technique can be extended to the so called tripod STIRAP scheme [98, 99, 100, 101] that allows the population transfer of coherent superposition states.

Coherent dark states

The most simple atomic system where various types of dark states occur consists of an excited state $|e\rangle$ and two atomic ground states $|a\rangle$ and $|b\rangle$. Two coherent light fields (Rabi-frequencies Ω_a and Ω_b) – nearly resonant to the transitions $|a\rangle \rightarrow |e\rangle$ and $|b\rangle \rightarrow |e\rangle$ with transition frequencies ω_a and ω_b – are incident on the atom (see Fig. 4.5).

In the case where only the field Ω_a is present, the atom is excited to the state $|e\rangle$ from which it can decay to both possible ground states. If the atom decays to the state $|a\rangle$ further excitation-emission processes will occur until the atom finally is pumped into the state $|b\rangle$.
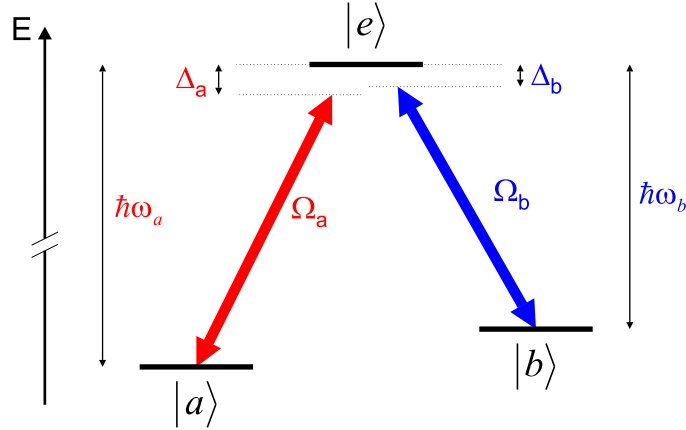
Figure 4.5.: Atomic system consisting of two stable ground states $|a\rangle$ and $|b\rangle$ and an excited state $|e\rangle$. Two light fields Ω_a and Ω_b – nearly resonant to the transitions $|a\rangle \rightarrow |e\rangle$ with frequency ω_a and $|b\rangle \rightarrow |e\rangle$ with frequency ω_b – are incident on the atom.

In this state no further coupling to the light field is possible and the atom remains "dark". Therefore, the state $|b\rangle$ is called a dark state with respect to the light field Ω_a.

Now we analyze the case in which both light fields are present. The atomic state is defined by

$$|\Psi(t)\rangle = c_a(t)\,|a\rangle + c_b(t)\,|b\rangle + c_e(t)\,|e\rangle \equiv \begin{pmatrix} c_a(t) \\ c_b(t) \\ c_e(t) \end{pmatrix} \tag{4.4}$$

with the time dependend amplitudes $c_a(t)$, $c_b(t)$ and $c_e(t)$. The Hamiltonian describing the interaction of the atomic system with the radiation field is in the interaction picture given by

$$\hat{H}_{ED} = -\frac{\hbar}{2} \begin{pmatrix} 0 & 0 & \Omega_a e^{-i\Delta_a} \\ 0 & 0 & \Omega_b e^{-i(\Delta_b+\phi)} \\ \Omega_a e^{i\Delta_a} & \Omega_b e^{i(\Delta_b+\phi)} & 0 \end{pmatrix}. \tag{4.5}$$

The Rabi-frequencies Ω_a and Ω_b are real and the initial phase difference of the two light fields is given by the phase ϕ. The detuning of the light fields relative to the transition $|a\rangle \rightarrow |e\rangle$ and $|b\rangle \rightarrow |e\rangle$ is described by Δ_a and Δ_b, respectively. From the Hamiltonian $\hat{H}_{ED}$ we can obtain three different eigenstates. One of these states consists only of contributions from the two ground states $|a\rangle$ and $|b\rangle$ and thus is stable against spontaneous decay. For equal detuning $\Delta_a = \Delta_b$ this eigenstate is given by

$$|\Psi_D(t)\rangle = \frac{\Omega_b}{\Omega_{eff}}\,|a\rangle - e^{i\phi}\frac{\Omega_a}{\Omega_{eff}}\,|b\rangle \tag{4.6}$$

with the effective Rabi-frequency

$$\Omega_{eff} = \sqrt{\Omega_a^2 + \Omega_b^2}. \tag{4.7}$$

The state in eqns (4.6) is an eigenstate of the interaction Hamiltonian and thus is stationary. Therefore, no coupling to the incident light fields occurs and the state is a dark state. The populations of the two contributing ground states depend on the ratio of the two Rabi-frequency Ω_a and Ω_b. Equation (4.6) defines the atomic dark state for any combination of Rabi frequencies of the two light fields, including the case where only one of the two light fields is present.

The reason for the occurrence of a dark state can be understood by analyzing the state in eqn (4.6) in the Schrödinger picture:

$$|\Psi_D(t)\rangle = e^{-i\omega_a t}\frac{\Omega_b}{\Omega_{eff}}|a\rangle - e^{-i(\omega_b - \phi)t}\frac{\Omega_a}{\Omega_{eff}}|b\rangle. \tag{4.8}$$

The coupling $|\Omega_a c_a| = |\Omega_b c_b|$ of each ground state $|a\rangle$ and $|b\rangle$ to the excited state $|e\rangle$ is equal. However, the relative phase of the two excitation amplitudes (given by the time evolution of the atomic states $|a\rangle$ and $|b\rangle$ and the relative phase of the incident light fields) is constant and of opposite sign. Thus, complete destructive interference of the two excitation possibilities occurs and no population is transferred. These kind of states are called coherent dark states because the existence of the dark state depends on a stable phase relation between the incident light fields.

In the above consideration spontaneous decay was neglected. A closer look at the system reveals that the spontaneous decay of the excited state $|e\rangle$ into the two ground states allows the preparation of the atomic system in the dark state via optical pumping. If both light fields are present the atom scatters light until it spontaneously decays into the state (4.6) and then remains dark. This process is often called coherent population trapping (CPT).

Degenerate coherent dark states

Coherent dark states are used in our experiment for the preparation and analysis of superposition states of the $5^2S_{1/2}$, $F = 1$ hyperfine ground level of ^{87}Rb. The $F = 1$ level consists of the three Zeeman sublevels $|1,\pm1\rangle$ and $|1,0\rangle$, where the first number corresponds to total angular momentum F of the hyperfine level and the second number defines the magnetic quantum number m_F of the Zeeman sublevel. An incident light field couples these states to the excited hyperfine level $5^2P_{1/2}$, $F' = 1$. In the absence of π-polarized light, a coherent dark state, consisting of the Zeeman sublevels $|1,\pm1\rangle$, will be generated. (see Fig. 4.6(a)).

In our experiment the energy difference between the two participating ground states $|1,\pm1\rangle$ is up to two orders of magnitude smaller than the linewidth of the atomic transition or the frequency distribution of the exciting light field. Thus, the two Zeeman sublevels are effectively degenerate. This simplifies the mathematical description because then also the incident light fields can be considered degenerate and can be described by a single field with the polarization vector

$$\mathbf{P} = \cos\alpha \cdot \boldsymbol{\sigma}^- + e^{i\phi}\sin\alpha \cdot \boldsymbol{\sigma}^+. \tag{4.9}$$

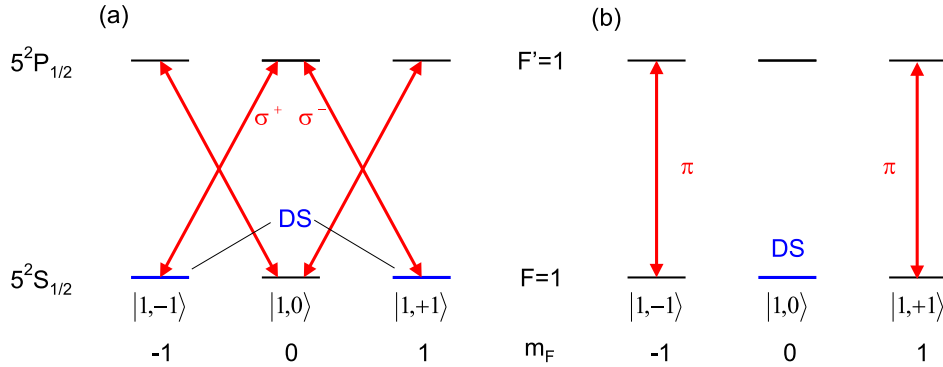Figure 4.6.: Term structure of ^{87}Rb used for the analysis of superposition states. (a) The (nearly degenerate) magnetic substates $|1, \pm 1\rangle$ of the $5^2S_{1/2}$, $F = 1$ ground level are coupled to the excited state by the $\sigma^\pm$-polarization components of the incident light field. A corresponding coherent dark state (DS) consisting of a superposition of the $|1, \pm 1\rangle$ ground states is generated. (b) The same situation in a different reference frame at an angle of 90° with respect to the situation in (a). In this system the incident light field is π-polarized and the dark state from (a) is the $|1, 0\rangle$ Zeeman sublevel.

The corresponding dark state is given by[4]

$$|\Psi_D\rangle = \cos\alpha\,|1, -1\rangle + e^{i\phi}\sin\alpha\,|1, +1\rangle . \tag{4.10}$$

In essence, the polarization of a single light field determines the coherent dark state consisting of a superposition of the two Zeeman sublevels. Choosing the appropriate polarization of the incident light field allows to prepare any possible superposition state by coherent population trapping.

Changing the reference frame allows a different interpretation of degenerate coherent dark states. If we assume equal intensity of both polarization components, rotating the reference frame by 90° transforms the superposition state in eqn (4.10) into the state $|1, 0\rangle$ (see eqn (A.48)) defined along the quantization axis of the new system (Fig. 4.6). In this reference frame, the incident light field is π-polarized and the existence of the dark state is caused by selection rules of atomic dipole transitions, that forbid the transition $F = 1$, $m_F = 0$ to $F' = 1$, $m_F = 0$.

---

[4]The relative phase of the two atomic Zeeman sublevels is defined by the phase difference of the polarization components **and** the Clebsch-Gordan coefficients of the involved transitions. For the transition $F = 1 \rightarrow F' = 1$ these coefficients give rise to an additional phase of π between the two possible transitions. Including this effect in our calculation we obtain eqn (4.10).

Therefore, rotating the reference frame allows a simpler description of degenerate coherent dark states, where the occurrence of the dark state originates from selection rules between the involved transitions. This transformation is possible if the external magnetic field is small, so that the inverse of the frequency splitting $\Delta\nu$ of the different atomic sublevels (due to the Zeeman effect), is smaller than the timescale necessary for the formation or analysis of the coherent dark state.

4.2.2. Stimulated Raman adiabatic passage (STIRAP)

Coherent atomic dark states are defined by the phase difference and the relative intensities of the involved light fields. A powerfull application of these dark states is the stimulated Raman adiabatic passage (STIRAP) technique, whereby an adiabatic change of the relative light intensities allows the complete population transfer between different atomic levels [47, 48, 49, 50, 51, 52].
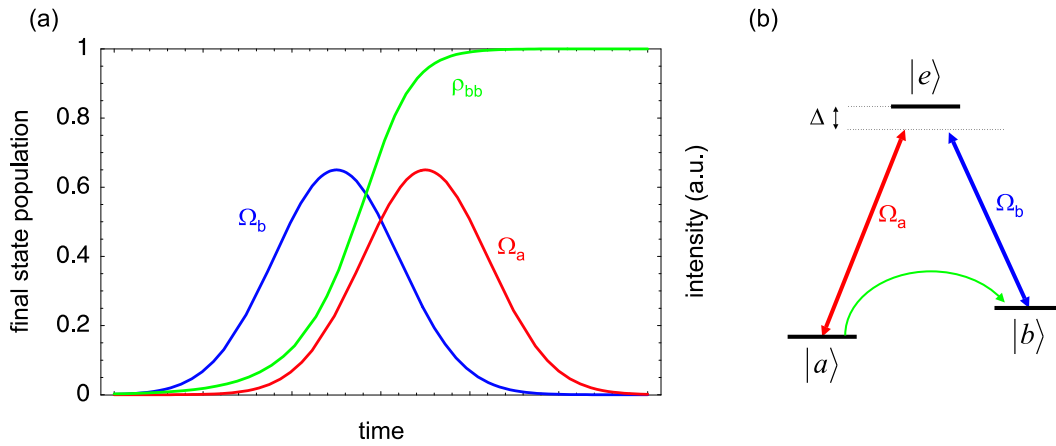

Figure 4.7.: (a) Typical pulse sequence of the STIRAP process and the corresponding population ρ_{bb} of the final state $|b\rangle$ and (b) corresponding level scheme. In order to transfer population from the initial state $|a\rangle$ to the final state $|b\rangle$, first the field Ω_b is incident on the atom followed by Ω_a. The population transfer occurs during the time when the two pulses overlap.

Adiabatic following in a three level system

Looking at the coherent dark state defined in eqn (4.6) one can ask the question what will happen, if the relative light intensity and thus the ratio of the Rabi frequencies $\Omega_a(t)$ and $\Omega_b(t)$

changes with time. Introducing the time dependent mixing angle θ by

$$\tan \theta(t) = \frac{\Omega_a(t)}{\Omega_b(t)}, \tag{4.11}$$

eqn (4.6) can be rewritten as

$$|\Psi_D\rangle = \cos \theta(t) |a\rangle - e^{i\phi} \sin \theta(t) |b\rangle . \tag{4.12}$$

As initial condition we choose the case where only the light field Ω_b is present ($\theta = 0$) and the atom is in the respective dark state $|\Psi_D\rangle = |a\rangle$. Increasing Ω_a while reducing Ω_b at the same time, the mixing angle θ changes until the light field Ω_b is switched off completely and the dark state becomes $|\Psi_D\rangle = |b\rangle$. For an adiabatic change of the light intensities, the atom stays in the time dependent dark state during the whole process. In essence all population – initially in the state $|a\rangle$ – is transfered to the state $|b\rangle$ without populating the excited state. Figure 4.7 shows the schematic pulse sequence of the STIRAP process and the change of the population ρ_{bb} of the final state $|b\rangle$.

Efficient population transfer requires that the atom remains in an eigenstate to the time dependent Hamiltonian during the whole transfer process. Otherwise, population transfer to the excited state $|e\rangle$ occurs, reducing the efficiency of the process. Non-adiabatic coupling between the different eigenstates of $\hat{H}_{ED}$ is small if the change of the mixing angle $d\theta/dt$ is small compared to the inverse of the frequency separation of the corresponding eigenvalues that for the case of zero detuning ($\Delta = 0$) is given by Ω_{eff} [48]. Thus, the condition for adiabaticity can be described by

$$\Omega_{eff} \cdot T \gg 1, \tag{4.13}$$

where T describes the interaction time of the atom with the two light fields.

Tripod STIRAP

The STIRAP technique allows the complete state transfer from an initial to a final atomic level. Including Zeeman sublevels in our consideration, the STIRAP scheme can be extended to the analysis or preparation of atomic superposition states [98, 99, 100, 101] by combining the occurrence of degenerate dark states (chapter 4.2.1) with the STIRAP technique.

In our experiment, the STIRAP light field Ω_1 – consisting of a certain superposition of σ^+ and σ^- polarization components – couples an initial superposition of the states $|1, -1\rangle$ and $|1, +1\rangle$ to the excited state $F' = 1$, $m_F = 0$ and the beam Ω_2 couples the excited state to the final hyperfine ground level $|F = 2\rangle$ of the process. The Zeeman sublevel of the final state $|F = 2\rangle$ depends on the polarization of Ω_2 and is not important for this consideration and thus ignored in the further discussion. Figure 4.8 shows the light fields and the atomic levels involved in this process and also clarifies the origin of the name "tripod STIRAP". Regarding the polarization of the light field Ω_1, a dark state $|\Psi_D\rangle$ and a bright superposition state $|\Psi_B\rangle$ (see eqn (4.10)), orthogonal to $|\Psi_D\rangle$, exist. The two states are given by

$$\begin{aligned}
|\Psi_D\rangle &= \cos \alpha |1, -1\rangle + \sin \alpha e^{+i\phi} |1, +1\rangle \tag{4.14} \\
|\Psi_B\rangle &= \sin \alpha |1, -1\rangle - \cos \alpha e^{+i\phi} |1, +1\rangle , \tag{4.15}
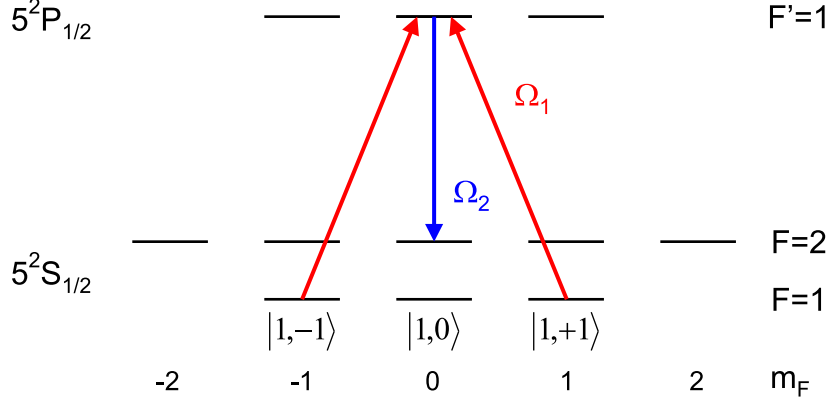\end{aligned}$$

Figure 4.8.: Tripod STIRAP scheme. The two polarization components of the light field Ω_1 couple to a certain superposition of Zeeman sublevels of the $F = 1$ hyperfine ground level. This superposition is transferred in the STIRAP process to the $F = 2$ hyperfine level, while the orthogonal superposition state remains in $F = 1$.

where the angles α and ϕ are defined by the polarization of the STIRAP light field Ω_1 (see eqn (4.9)). The state $|\Psi_D\rangle$ is a time independent dark state, whereas the state $|\Psi_B\rangle$ has a temporal evolution given by the coherent interaction with the STIRAP light fields. In analogy to eqn (4.12), the time evolution of the state is given by

$$|\Psi_B(t)\rangle \quad = \quad \cos\theta(t) \left[\sin\alpha \, |1,-1\rangle - \cos\alpha \, e^{i\phi} \, |1,+1\rangle \right] - e^{i\phi'} \sin\theta(t) \, |F=2\rangle , \quad (4.16)$$

where ϕ' is the phase difference of the two STIRAP light fields Ω_1 and Ω_2. The final state of the evolution is $|\Psi_B(\infty)\rangle = |F=2\rangle$. In essence, the polarization of Ω_1 defines which superposition $|\Psi_B\rangle$ of the states $|1,\pm1\rangle$ couples to the STIRAP light field and is transferred to the $F = 2$ hyperfine ground level, while the orthogonal superposition state $|\Psi_D\rangle$ remains unchanged and will not be transferred.

Together with the hyperfine level detection described in section 4.1, the tripod STIRAP technique allows to distinguish any superposition of the states $|1,\pm1\rangle$ by choosing a suitable polarization of the light field Ω_1. Compared to other detection schemes as e.g. Raman transition, the STIRAP scheme has the advantage of high insensitivity to changes of experimental parameters as long as the condition of adiabaticity is fulfilled. Therefore, the STIRAP technique is an ideal experimental technique for our purpose that can be used for the detection of internal atomic superposition states in any possible measurement basis.

4.2.3. Experimental realization of the state selective transfer

The verification of atom-photon entanglement requires correlation measurements between the photon polarization and the internal atomic Zeeman sublevels in different measurement bases. Therefore, the analysis of atomic superposition states represents a crucial step in our experimental scheme. This analysis is realized using the tripod STIRAP process, that transfers an initial superposition of the Zeeman sublevels $m_F = \pm 1$ of the $5^2S_{1/2}$, $F = 1$ ground level into a superposition of the two hyperfine ground levels $F = 1$ and $F = 2$. Together with the hyperfine level detection this allows the analysis of internal atomic levels in arbitrary measurement bases.

This section describes the generation of the STIRAP light fields using two laser diodes locked on atomic transitions via Doppler-free saturation spectroscopy. The pulse sequence is generated using AOMs allowing a minimum pulse width and transfer time down to 20 ns. Preparing a single atom in definite superposition states, we analyzed the dependence of the efficiency of the population transfer on the polarization of the STIRAP light field.
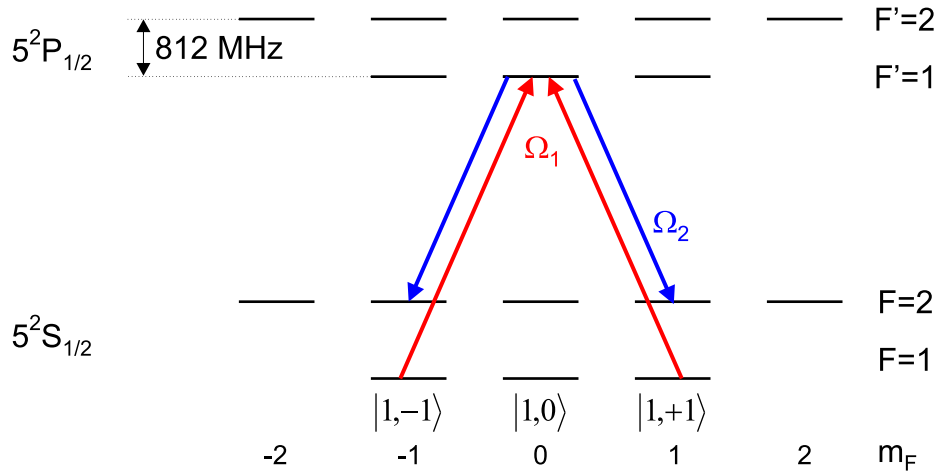

Figure 4.9.: STIRAP transition via the excited hyperfine level $5^2P_{1/2}$, $F' = 1$ in ^{87}Rb. In order to achieve a high detection accuracy (see section 4.2.4), both STIRAP light fields Ω_1 and Ω_2 – resonant to the transitions $F = 1 \rightarrow F' = 1$ and $F = 2 \rightarrow F' = 1$, respectively – consist of σ^- and σ^+ polarization components.

STIRAP transition

In the STIRAP transfer, the relative phase and amplitude of the σ^+ and σ^- polarization components define which superposition of the Zeeman sublevels $|1, \pm 1\rangle$ is transferred. Due to the transversal character of electromagnetic waves, this requires that the STIRAP light is incident along the quantization axis of our system, defined by the collection optics of the fluorescence light. In order to separate the STIRAP light from the atomic fluorescence ($\lambda = 780$ nm), the adiabatic transfer is accomplished using the D_1 line ($\lambda = 795$ nm) of ^{87}Rb (see Fig. 4.9). Furthermore, the level substructure of the $5^2 P_{1/2}$ excited state consists only of two hyperfine levels with a large frequency separation of 812 MHz. This reduces the possibility of off-resonant transfer that could result in a lower accuracy of the STIRAP process (see chapter 4.2.4).
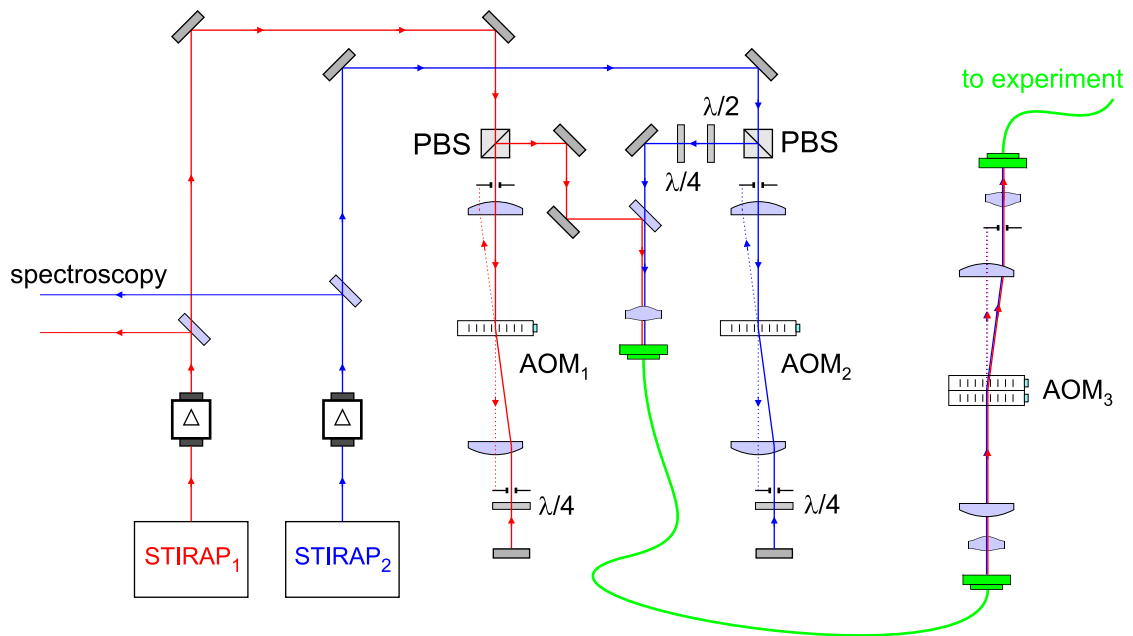

Figure 4.10.: Setup of the STIRAP laser system. The two beams are generated by two laser diodes, independently stabilized using Doppler-free saturation spectroscopy. AOMs in double-pass configuration generate the STIRAP pulse sequence. Afterwards, the two laser pulses are combined and coupled into a single mode fiber and sent to a second AOM stage improving the on/off-switching ratio for the STIRAP light.

Generation of the STIRAP sequence

According to the preceeding chapter, phase coherence of the two STIRAP light fields is essential for an effective population transfer. In our experiment a fast population transfer on the order of 50 ns has to be performed which is much shorter than the coherence time of our laser diodes [21]. Due to the uncertainty principle $\Delta t \cdot \Delta \nu < 1/2\pi$ the STIRAP pulse length corresponds to a spectral uncertainty of approximately 3 MHz which is larger than the long-time frequency drift of the laser diodes [103]. Thus, the short transfer time allows to fulfill the conditions of phase coherence and two-photon resonance using two independently stabilized laser diodes for the generation of the STIRAP pulse sequence.
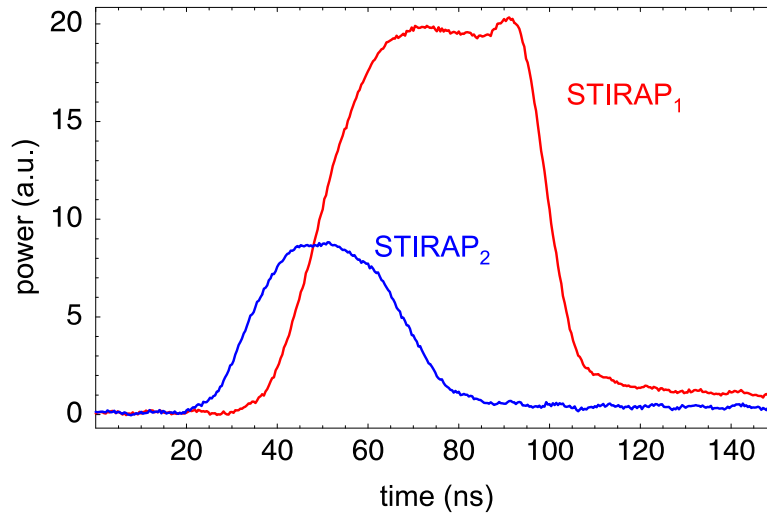

Figure 4.11.: Typical STIRAP pulse sequence with pulse widths of approximately 30 respective 40 ns. The population transfer is performed in the intersection region of the two pulses.

The diodes are frequency stabilized using Doppler-free saturation spectroscopy on the transitions $F = 1 \rightarrow F' = 1$ (STIRAP$_1$) and $F = 2 \rightarrow F' = 1$ (STIRAP$_2$) of the D$_1$-line. The STIRAP pulse sequence is generated by an AOM in a double pass configuration in each laser beam. With this setup we achieve a minimum pulse length down to 20 ns (FWHM) (Fig. 4.11). After adjusting the relative polarization of the light fields, the two beams are combined on a beam splitter and coupled into a single mode optical fiber (Fig. 4.10).

In order to fulfill the condition of adiabaticity for the STIRAP process, $10^4...10^5$ saturation intensities are necessary for the STIRAP light fields. This sets stringent conditions on the on/off-switching ratio of the AOMs. Therefore, the combined STIRAP light field is sent
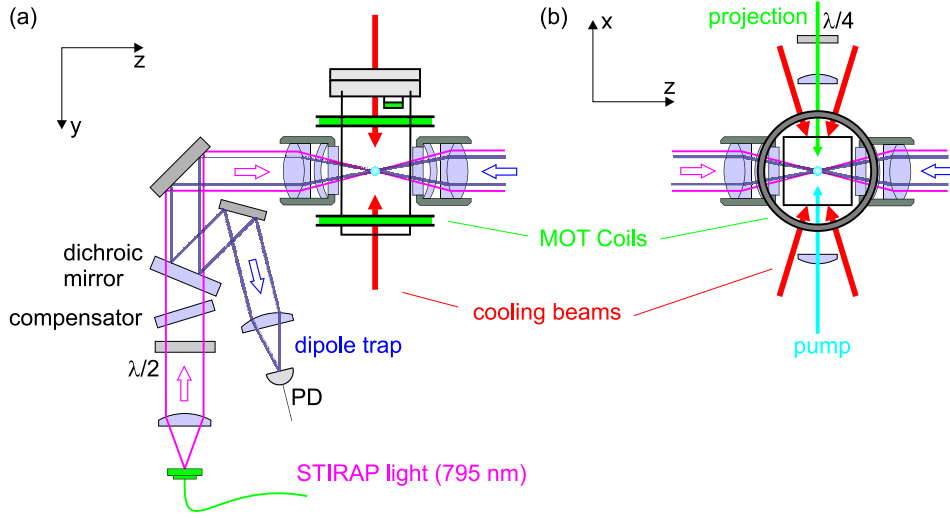
Figure 4.12.: Experimental setup of the atomic state analysis. (a) Top view: The STIRAP light from a single mode optical fiber passes a half- and quarterwave plate to adjust the light polarization and is focused to a waist of approximately 8 μm at the position of the atom in the dipole trap. A compensation crystal corrects the birefringence of the diverse optical components. To separate the dipole trap light from the STIRAP field a dichroic mirror is used. (b) Side view showing the vertical cooling beams, the projection laser and the pump beams.

through a second pair of AOMs increasing the total on/off-switching ratio of the light intensity to a value of better then 10^{10}.

Experimental setup

Figure 4.12 shows the optical setup around the vacuum cell, including all incident light beams. The STIRAP light for the atomic state detection is collimated from a single mode optical fiber and passes a half- and quarterwave plate to set the polarization. A dichroic mirror separates it from the dipole trap beam. In order to satisfy the condition of adiabaticity high STIRAP light intensities are necessary. Thus, the light (power up to 200 μW) is focused to a waist size of 8 μm at the position of the atom using a microscope objective. This way we achieve up to $3 \cdot 10^5$ saturation intensities. For a complete state analysis, i.e. to transfer any possible superposition state of the two atomic Zeeman sublevels $|1, \pm 1\rangle$, the light has to be aligned along the quantization axis defined by the collection optics for fluorescence detection. The STIRAP light is resonant to the D_1-line ($\lambda = 795$ nm) and is separated from the atomic fluorescence
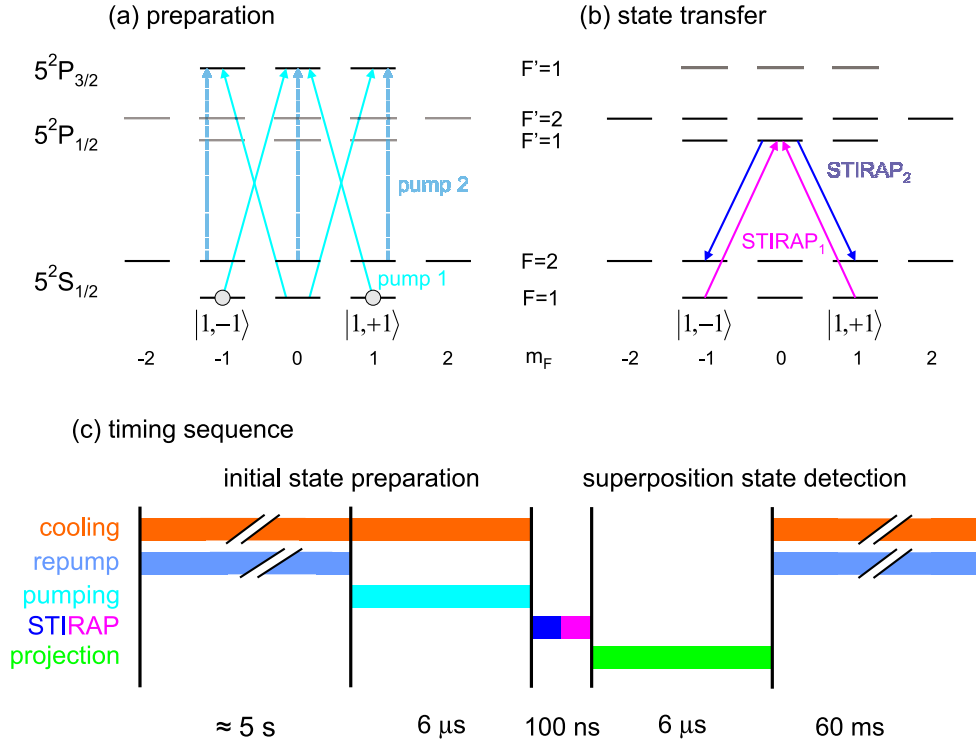
Figure 4.13.: Preparation and detection of atomic superposition states. (a) Linearly polarized pump light prepares the atom in a coherent dark state, i.e. a superposition of the two Zeeman sublevels $|1, \pm 1\rangle$. (b) After the preparation, the STIRAP sequence transfers a certain superpostion state to the $F = 2$ ground level. Finally, the hyperfine level detection reveals the initial atomic superposition state. (c) Timing sequence of the preparation and detection process.

(780 nm) using two interference filters with a bandwidth of 3 nm (FWHM) in front of the avalanche photo diodes.

Superposition state detection

In order to test the state selective STIRAP transfer, the preparation of definite initial superpositions of the Zeeman sublevels $|1, \pm 1\rangle$ is necessary. Therefore, coherent population trapping – using a linearly polarized $(\sigma^+ + \sigma^-)$ pump laser (see Fig. 4.13) resonant to the transition
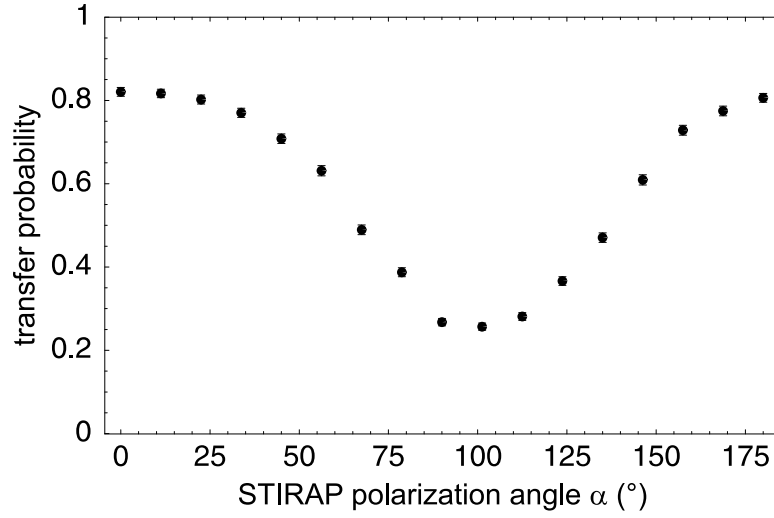
Figure 4.14.: Transfer probability of atomic population in the $F = 1$ ground level to the $F = 2$ hyperfine ground level as a function of the polarization of the STIRAP light field. For a vertically polarized light field Ω_1 ($\alpha = 0°$) most of the atomic population is transferred while for the orthogonal polarization ($\alpha = 90°$) the atom does not couple to the STIRAP light field and remains in the $F = 1$ ground level.

$5^2 S_{1/2}$, $F = 1 \to 5^2 P_{3/2}$, $F' = 1$ – is used to prepare the atom in the coherent dark state

$$|\Psi\rangle = \frac{1}{\sqrt{2}} \left(|1, -1\rangle + |1, +1\rangle \right). \tag{4.17}$$

A second beam (resonant to the transition $5^2 S_{1/2}$, $F = 2 \to 5^2 P_{3/2}$, $F' = 1$) together with the cooling light pumps residual population in the $F = 2$ hyperfine ground level back to $F = 1$. In order to achieve a high pump efficiency residual magnetic fields have to be compensated (see chapter 4.3 and [104, 68]).

After the preparation of the initial state defined in eqn (4.17) the atomic state detection is performed applying the STIRAP pulse sequence. Depending on the polarization of the STIRAP light a certain superposition of the atomic Zeeman sublevels $|1, \pm 1\rangle$ is transfered to the $F = 2$ ground level. For the initial state in eqn (4.17) optimal transfer efficiency is obtained for a vertically polarized light field Ω_1 ($\mathbf{V} = \boldsymbol{\sigma}^+ - \boldsymbol{\sigma}^-$). After the state transfer, the hyperfine level detection is performed to read out the atomic hyperfine ground level and to deduce the initial superposition state of the atom.

Figure 4.14 shows the measured probability to transfer the atomic population from the

superposition given by eqn (4.17) to the $F = 2$ hyperfine ground level as a function of the polarization of the STIRAP light field. For vertically polarized light ($\alpha = 0°$) maximum coupling of the STIRAP light to the initial superposition state occurs and most of the atomic population is transferred. Changing the polarization angle of the light field, the transfer efficiency decreases until for orthogonal polarization the initial superposition state is a dark state and we observe minimum transfer efficiency.

In the measurement in Fig. 4.14 we observe a visibility of 0.57 ± 0.01, which is mainly limited by the preparation efficiency of the initial superposition state. For the verification of atom-photon entanglement, a highly reliable atomic state detection is essential, thus it is inevitable to obtain a more quantitative statement of the accuracy of the atomic state detection process. Therefore, a more accurate initial state preparation is necessary overcoming the limits of our optical pumping technique.

4.2.4. Accuracy of the state detection process

A high accuracy of the superposition state detection is essential for its application in the verification of atom-photon entanglement. Thus, it is necessary to develop an experimental procedure that allows to estimate the accuracy of the state detection scheme. In the preceding chapter a test of the state detection was presented, but in the experimental procedure the detection accuracy was limited by the efficiency of the preparation of the initial superposition state.

In order to achieve a reliable measure for the transfer efficiency, the faithfull preparation of defined superposition states is required. Preparing the initial state by optical pumping techniques does not provide a sufficient preparation accuracy due to a large variety of error sources[5]. Thus, a different preparation scheme is used. In this scheme, the initial atomic superposition state is generated in the spontaneous decay of the excited hyperfine level $5^2P_{3/2}$, $F' = 0$. Together with post-selection of the polarization of the emitted photon, this provides an accurate preparation of the initial state and allows to measure the transfer efficiency with higher accuracy.

Preparation of the initial superposition state

The preparation of a definite initial superposition state can be realized using the spontaneous decay of the excited hyperfine level $5^2P_{3/2}$, $F' = 0$ (see chapter 2) where, depending on the polarization of the emitted photon, the final state of the atom is in a certain superposition of the Zeeman sublevels $|1, -1\rangle$ and $|1, +1\rangle$. Measuring the photon polarization in H/V-basis we obtain the following atomic superposition states

$$\text{H-polarization:} \quad |\Psi\rangle \quad = \frac{1}{\sqrt{2}} \left(|1, -1\rangle + |1, +1\rangle \right) \tag{4.18}$$

$$\text{V-polarization:} \quad |\Psi\rangle \quad = \frac{1}{\sqrt{2}} \left(|1, -1\rangle - |1, +1\rangle \right). \tag{4.19}$$

This preparation technique is less sensitive to experimental parameters, because for excitation to the $F' = 0$ hyperfine level, the probability to prepare wrong excited states is greatly reduced

---

[5]as e.g. polarization errors or misalignment of the magnetic field or the pump beam direction

(see chapter 5.1). Thus it allows the preparation of initial atomic superposition states with a high accuracy.

Polarization effects on the transfer efficiency

After the preparation, the superposition state detection is performed to read out the atomic state. Figure 4.15 (a) shows the measured transfer probability as a function of the STIRAP light intensity for both superposition states: the bright state (blue data) coupling to the STIRAP light field Ω_1 and the orthogonal dark state (red data). In the case where both STIRAP fields are parallel linearly polarized we observe the expected behavior: after a certain threshold intensity the transfer probability for the bright state increases and reaches the maximum value with a transfer probability of about 94% (including errors from the hyperfine level detection) while it stays low for the dark state.

In the measurement Fig. 4.15 (b) the atom was initially prepared in one of the two Zeeman sublevels $|1, -1\rangle$ and $|1, +1\rangle$ and both STIRAP light fields were σ^+-polarized. The transfer probability for the bright state shows the same behavior as before. However, after a certain threshold intensity, also for the dark state full population transfer occurs.

For a further investigation of the different behavior of the dark states in Fig. 4.15 (a) and (b), we must perform a full analysis of the STIRAP process. Because no magnetic guiding field is applied in our experiment, no preferred quantization axis exists. Thus, we can choose an appropriate coordinate system that simplifies the description of the atomic system. For the measurement with linearly polarized STIRAP light, we choose the system where the quantization axis is parallel to the polarization vector of the light field. In this system, the STIRAP light is π-polarized (see Appendix A.2.1) and the situation in Fig. 4.9 translates to the situation in Fig. 4.16 (a), where the dark state in the new system is given solely by the Zeeman sublevel $|1, 0\rangle$.

The short timescale of the transfer process (< 50 ns) results in a large spectral width of the STIRAP pulses. Together with the high intensity of the STIRAP light, off-resonant transfer of the dark state via the $F' = 2$ excited hyperfine level is possible. The level structure of ^{87}Rb allows to circumvent this effect by using an appropriate polarization of the STIRAP light field Ω_2. For parallel linear polarization of the two STIRAP fields, the transfer of the dark state via the $F' = 2$ intermediate state is forbidden due to selection rules of dipole transition and thus, both possible two-photon transitions share the same dark state (Fig. 4.16 (a)).

In the case of circularly polarized light (Fig. 4.16 (b)), we observe the opposite behavior. For parallel polarization, no combined dark state exists, while for orthogonal circular polarization, resonant and off-resonant transfer share the same dark state. This explains the significantly higher transfer probability of the dark state for parallel circularly polarized STIRAP light compared to horizontal polarization. Figure 4.17 shows the state transfer for orthogonal circular polarization of the STIRAP light field, where again a dark state for both transitions occurs[6]. The solid lines in Fig. 4.15 and 4.17 are obtained from numerical solutions of the optical Bloch equation (see chapter A.1.4) and are in good agreement with our experimental data and thus verify the validity of the above discussion.

---

[6]For high laser powers we again observe transfer of the dark state. This is due to polarization errors of the STIRAP light that again give rise to a non-zero transfer probability via the F'=2 excited state.
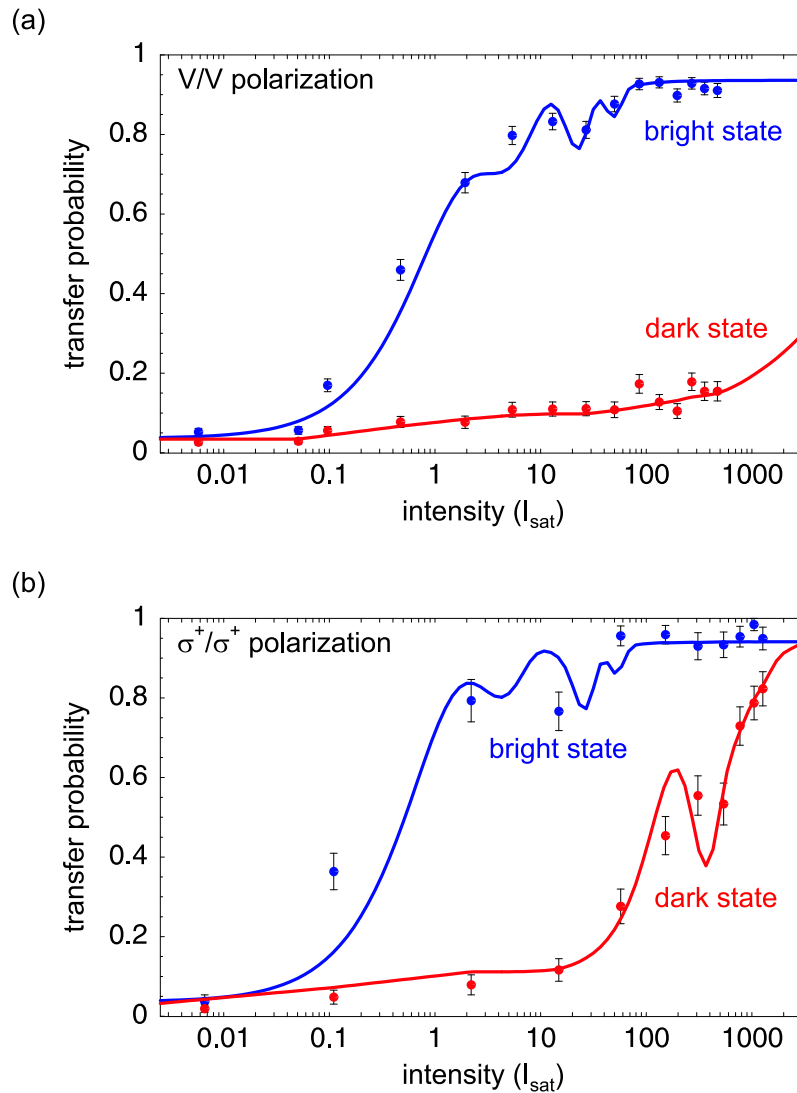
Figure 4.15.: Transfer efficiency for the bright (red points) and the dark state (blue points) as a function of the intensity of the STIRAP light (in saturation intensities) for (a) vertical and (b) σ^+-polarization of both STIRAP light fields. The solid lines are theoretical curves calculated from a numerical solution of the optical Bloch equations (including estimated polarization errors of the STIRAP fields). For a better fit the numerical solutions were corrected for the reduced visibility in the measurement.
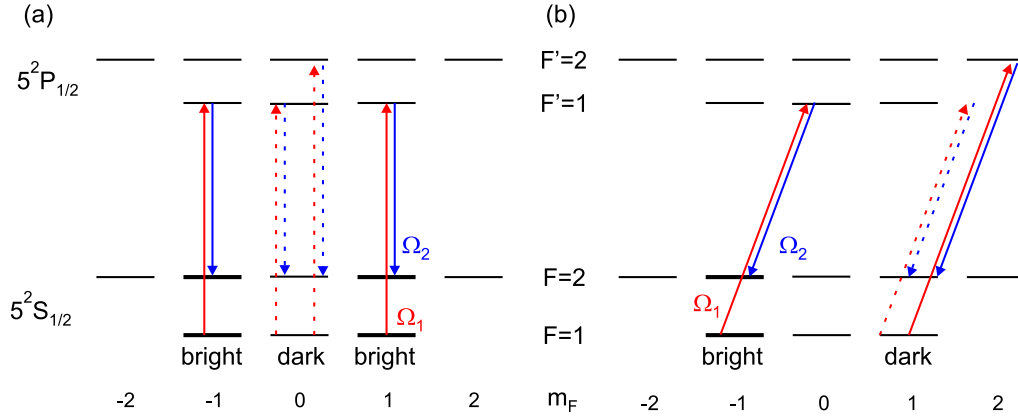
Figure 4.16.: Possible couplings (solid lines) and forbidden transitions (dashed lines) of the STIRAP light fields for both, "dark" and "bright" state in the appropriate reference frame. (a) For parallel linearly polarized STIRAP light, resonant (via $F' = 1$) and off-resonant transfer (via $F' = 2$) of the dark state is forbidden (the transitions $F = 1 \rightarrow F' = 1$, and $F = 2 \rightarrow F' = 2$ are forbidden for $\Delta m_F = 0$ due to selection rules of atomic dipole transitions). (b) For parallel σ^+ polarization, off-resonant transfer of the dark state via the $F' = 2$ excited state is possible.

Condition for a joint dark state

The presented results show that the supression of off-resonant STIRAP transfer via the excited state hyperfine level $F' = 2$ is important for an accurate atomic state detection. Choosing a suitable polarization of the STIRAP laser Ω_2, such that off-resonant transfer is forbidden by selection rules of atomic dipole transitions, a highly accurate atomic superposition state detection is possible. In order to get an expression for the necessary polarization of the light field Ω_2 in the general case, we assume that the STIRAP light Ω_1 is in the polarization state

$$\mathbf{P}_{STIRAP_1} = \cos\alpha \cdot \boldsymbol{\sigma}^+ + e^{i\phi} \sin\alpha \cdot \boldsymbol{\sigma}^-. \tag{4.20}$$

The corresponding atomic dark state for the transition $F = 1 \rightarrow F' = 1$ is given by

$$|\Psi_D\rangle = \cos\alpha \, |1, +1\rangle + e^{i\phi} \sin\alpha \, |1, -1\rangle. \tag{4.21}$$

For optimal distinguishability of the dark state $|\Psi_D\rangle$ from the orthogonal superposition state, off-resonant transfer of $|\Psi_D\rangle$ via the $F' = 2$ excited state has to be forbidden. Due to the higher number of degrees of freedom of the $F' = 2$ excited level (compared to the $F = 1$ ground level) no darkstate exists for the transfer $F = 1 \rightarrow F' = 2$. However, for the transition
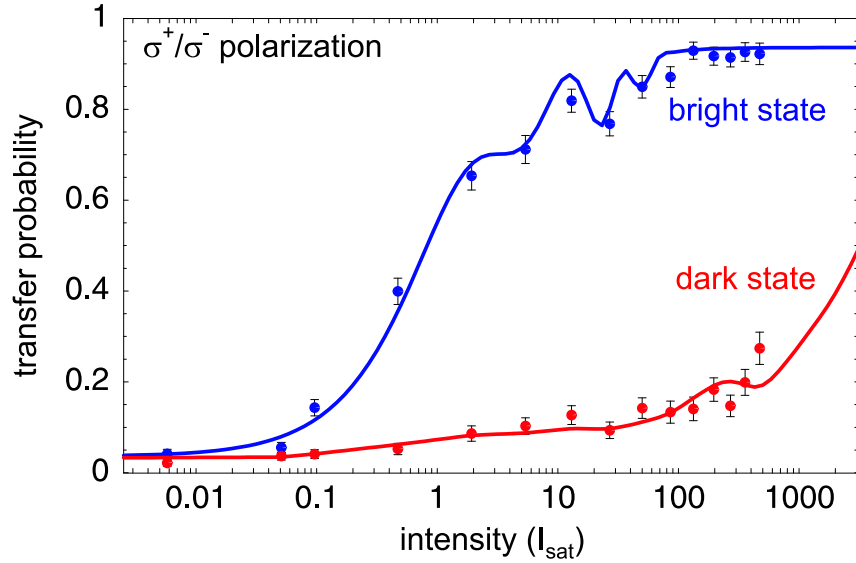
Figure 4.17.: Dependence of the transfer efficiency on the STIRAP intensity for $\sigma^+/\sigma-$ polarization and theoretical prediction (solid lines). In this case a common dark state for both, resonant and off-resonant transfer exists.

$F = 2 \rightarrow F' = 2$ a darkstate exists. Thus, a simultaneous dark state will occur, if the polarization of the STIRAP light field Ω_2 is chosen such, that for the initial state in eqn (4.21) the transition $F = 2 \rightarrow F' = 2$ is forbidden (see also Fig. 4.16). A calculation including the Clebsch-Gordan coefficients of all possible transitions between the different Zeeman sublevels yields for the necessary polarization vector of the STIRAP field Ω_2:

$$\mathbf{P}_{STIRAP_2} = \sin \alpha \cdot \boldsymbol{\sigma}^+ + e^{i\phi} \cos \alpha \cdot \boldsymbol{\sigma}^-. \tag{4.22}$$

Therefore, for maximum detection accuracy of the atomic superposition states, the two STIRAP light fields have to be polarized according to eqns (4.20) and (4.22). For the cases $\alpha = \pi/4$ and $\alpha = 0, \pi$ this yields the conditions of parallel linear and orthogonal circular polarization already discussed in the previous section.

Detection accuracy

For the application of the state detection it is necessary to obtain an accurate measure for the reliability of this detection method. In our setup, the preparation and analysis of well defined circular polarization requires more optical elements, thus more polarization errors are present

	dark state detection	bright state detection
APD dark counts	1.5%	1.5%
preparation of wrong excited states	0.5%	0.5%
hyperfine level detection	3.7%	0.7%
STIRAP polarization	1.0%	1.0%
off resonant transfer	0.5%	0.5%
total error	7.0%	4.2%

Table 4.2.: Origin and (estimated) value for the increase respective decrease of the transfer probability for the different error sources occurring in the superposition state detection of the dark and bright atomic state. The first two entries reduce the fidelity of the preparation of the initial superposition state and thus do not directly introduce errors into the detection scheme.

in this case[7]. Therefore, we limit the discussion of the detection accuracy to the case of linear polarization, where we can assure a better polarization control.

From a measurement similar to Fig. 4.15 but with higher resolution in the region of maximum contrast, we obtain for the transfer probability of the dark and the bright state

$$p_{darkstate} = \quad 9.1 \pm 1.0\% \tag{4.23}$$

$$p_{brightstate} = \quad 94.9 \pm 1.0\%. \tag{4.24}$$

Thereby, two types of errors contribute to the reduction of the detection accuracy. Dark counts of the avalanche photo diodes and preparation of the wrong excited state (see chapter 5.1) give rise to errors in the preparation of the initial superposition state. On the other hand, the limited accuracy of the hyperfine level detection and polarization errors in the STIRAP polarization and the corresponding possible off-resonant transfer directly reduce the accuracy of the superposition state detection. Table 4.2 shows the contributions of the different error sources to the detection of the dark and the bright state.

Taking into account table 4.2, we can explain the measured transfer probability of the dark and bright superposition states. The main contributions to the reduction respective increase of the transfer probability occur from dark counts of the single photon detector and the limited accuracy of the hyperfine level detection scheme (see chapter 4.1). To obtain the accuracy of the superposition state detection, i.e. the probability that the superposition state was correctly identified, we have to correct the measured transfer probabilities for errors in the preparation of the initial superposition states. This yields an detection accuracy of $a_D \approx 93\%$ and $a_B \approx 97\%$ for the dark and the bright state, respectively.

---

[7]This can be seen in in the measurements in Fig. 4.15 (a) and 4.17, that show a higher distinguishability of the dark and bright state for linearly polarized STIRAP light

Summary

Combining the spontaneous decay with post-selection on the polarization measurement outcome of the emitted photon allows to prepare initial atomic superposition states with a high fidelity. This gives the possibility to measure the detection accuracy of the atomic superposition states, which can be realized with a mean accuracy of 95 %. The high accuracy recommends the application of this process for the verification of atom-photon entanglement.

4.3. Larmor precession of the atomic angular momentum

The detection process presented in this chapter provides a powerfull tool for the analysis of internal atomic states. Choosing an appropriate STIRAP polarization allows to perform a projective measurement on any superposition state of the atomic qubit. The following section presents an application of the state detection scheme that allows the observation of Larmor-precession of a single atom in an external magnetic field.

In the experiment, the atom is initially prepared in a certain superposition state using optical pumping. The residual magnetic field gives rise to a Zeeman splitting of the atomic ground states that results in a time dependent phase shift, which is equivalent to the Larmor-precession of the atomic magnetic moment. Using the superposition state detection we are able to perform a time resolved observation of the precession process.

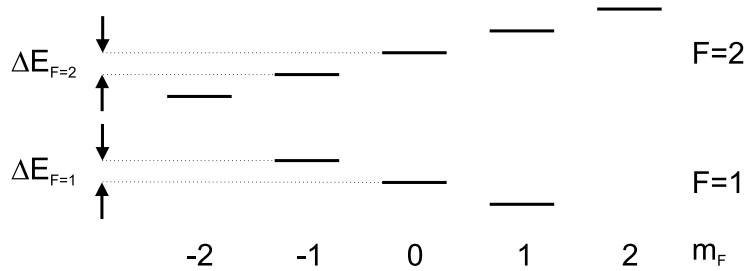## 4.3.1. Superposition of Zeeman sublevels in a magnetic field

Figure 4.18.: Shift of the Zeeman sublevels of the atomic hyperfine ground levels $F = 1$ and $F = 2$ in a magnetic field applied along the quantization axis.

In the following analysis we first assume the case, where a single atom is located at a position with a well defined magnetic field $B \cdot \mathbf{e}_z$ pointing along the quantization axis of the atom. For low field strengths the energy shift ΔE of the Zeeman sublevels is given by

$$\Delta E = g_F \mu_B m_F B, \tag{4.25}$$

where $\mu_B = e\hbar/2m_e$ is the Bohr magneton with the electron mass m_e, m_F is the projection of the angular momentum on the quantization axis and g_F is the Landé-factor, given by $g_F = -1/2$ and $g_F = 1/2$ for the $F = 1$ and $F = 2$ ground state hyperfine levels of ^{87}Rb [67] (Fig. 4.18). If the atom is initially in a pure Zeeman sublevel, i.e. in an eigenstate to the
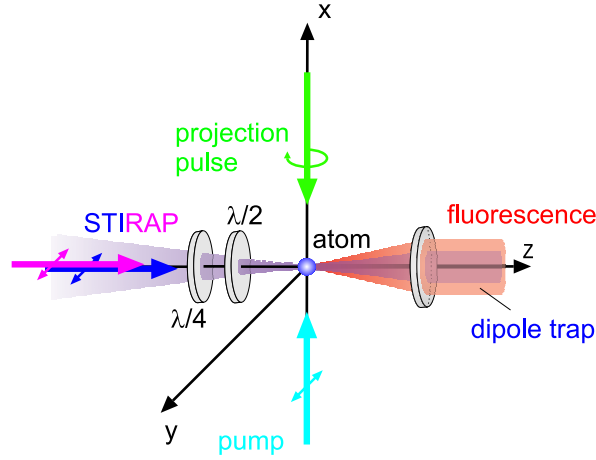
Figure 4.19.: Experimental setup and laboratory reference frame for the observation of Larmor precession. The quantization axis (z-axis) is defined by the collection optics of the atomic fluorescence and the STIRAP light field.

magnetic field, the energy shift will only give rise to a time dependent global phase with no observable effects.

Next, we consider the case, where the atom is initially in a superposition state of Zeeman sublevels as defined by eqn (4.17). The time evolution of each sublevel is determined by the expression $\exp(i\Delta E \cdot t/\hbar)$. Since both Zeeman sublevels shift by the same amount $|\Delta E|$, but with opposite sign, the state evolves according to

$$|\Psi(t)\rangle = \frac{1}{\sqrt{2}} \left(|1, +1\rangle + e^{2i\omega_L t} |1, -1\rangle \right) \tag{4.26}$$

with the Larmor-frequency $\omega_L = -eB/4m_e$. Due to the time-dependent phase shift $\phi(t) = 2\omega_L t$ the superposition state changes in time, which is equivalent to the so-called Larmor precession of the atomic magnetic moment in the external magnetic field B. The oscillation of the superposition state can be observed in our experiment as an oscillatory change in the transfer probability of a specific state, if the atomic state detection is applied after a well defined delay time.

Determination of the Larmor precession

For a full description of the Larmor precession, we have to analyze the evolution of all Zeeman sublevels of the atomic hyperfine ground level with the total angular momentum $F = 1$. In

general, three special coordinate systems exist. One system is defined by the initial atomic superposition state which in our experiment is

$$|\Psi_L(t=0)\rangle = \frac{1}{\sqrt{2}}\left(|1,-1\rangle + |1,+1\rangle\right). \tag{4.27}$$

This state is an angular momentum eigenstate $|1,0\rangle_y$ along the y-axis with $m_F = 0$ (see eqn (A.56)). The measurement basis of the atomic state detection and the orientation of the magnetic field define the other preferred coordinate systems. In the general case the quantization axes of the three reference frames are not parallel. To calculate the evolution of the initial superposition state $|\Psi_L(0)\rangle$, we set the quantization axis along the observation direction. In our experiment, the Larmor precession of $|\Psi_L(t)\rangle$ is analyzed by projecting the state onto the two superposition states $|\Psi_L(0)\rangle$ and

$$|\Psi_{L,\perp}\rangle = \frac{1}{\sqrt{2}}\left(|1,-1\rangle - |1,+1\rangle\right). \tag{4.28}$$

In order to obtain the evolution of the initial state eqn (4.28), it is expressed in terms of the energy eigenstates of the atomic system. For a magnetic field defined by

$$\mathbf{B} = |\mathbf{B}| \cdot \begin{pmatrix} \sqrt{1-z^2}\cos\phi \\ \sqrt{1-z^2}\sin\phi \\ z \end{pmatrix}, \tag{4.29}$$

the energy eigenstates are given by eqns (A.48)-(A.50), where $z\epsilon[-1,1]$ and ϕ are the cylindrical coordinates of the system in Fig. 4.19. In the eigensystem, the time evolution of $|\Psi_L(t)\rangle$ can directly be obtained from the evolution of the basis states. Therefrom, we calculate the overlap of $|\Psi_L(t)\rangle$ with the initial state $|\Psi_L(0)\rangle$ and the orthogonal superposition state $|\Psi_{L,\perp}\rangle$, which are given by:

$$\begin{aligned} |\langle\Psi_L(0)|\Psi_L(t)\rangle|^2 &= \frac{1}{4}\Big[(z^2-1)\cos 2\phi + (z^2+1)\cos\omega_L t - \\ &\qquad (z^2-1)(1+\cos\omega_L t \cdot \cos 2\phi)\Big]^2 \end{aligned} \tag{4.30}$$

$$|\langle\Psi_{L,\perp}|\Psi_L(t)\rangle|^2 = \left[\frac{(1-z^2)}{2}\sin 2\phi(1-\cos\omega_L t) + z\sin\omega_L t\right]^2. \tag{4.31}$$

Figure 4.20 shows the calculated overlap as function of time for a magnetic field approximately aligned along the z-direction. In the case where the magnetic field is parallel to the quantization axis ($z = 1$), a pure sinusoidal oscillation with the frequency $2\omega_L$ is observed (see eqn (4.26)) and we can obtain a simple interpretation of the precession process in which the initial state in $|\Psi_L(0)\rangle$ is an eigenstate along the y-axis of our system and the magnetic field gives rise to a precession of this eigenstate around the z-axis with frequency ω_L. Defining a reference frame that rotates around the z-axis with the same frequency allows a simple description of the precession process. In this description, the atom permanently stays in the eigenstate $|1,0\rangle$ defined in the time-dependent rotating frame. Figure 4.21 shows this rotating reference frame and the corresponding eigenstates.
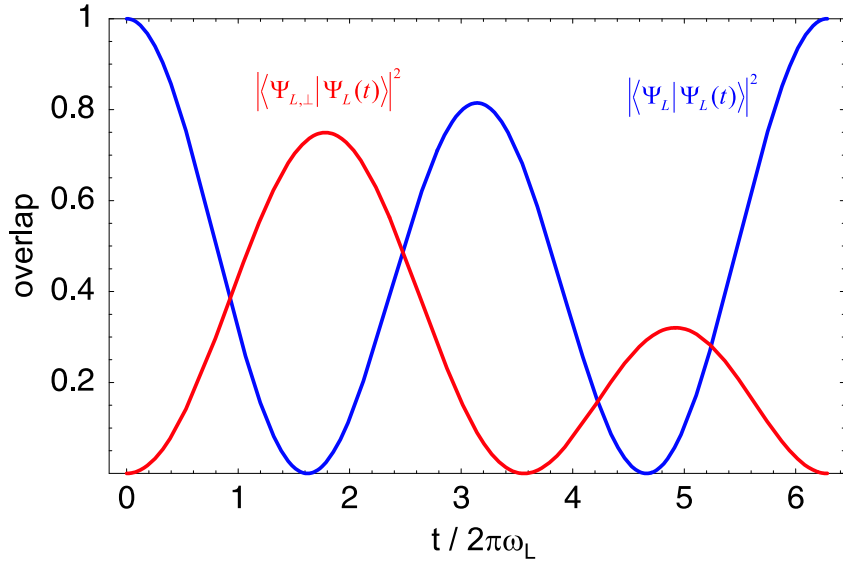
Figure 4.20.: Time dependend overlap of the precessing magnetic moment with the initially prepared superposition state $|\Psi_L\rangle$ (blue curve) and the orthogonal superposition state $|\Psi_{L,\perp}\rangle$ (red curve). The magnetic field direction is defined by $\phi = 0.1$, $z = 0.5$.

4.3.2. Observation of Larmor precession

In our experiment, we analyze the Larmor precession of the angular momentum of a single atom, that is initially prepared in the coherent dark state given by eqn (4.28). After a defined delay time the superposition state detection is performed. Thereby, the precession of atomic angular moment in the magnetic field can be observed as a time dependent change in the transfer efficiency of the atomic state in the STIRAP process.

Magnetic field compensation

For a high visibility of the Larmor-precession, the initial atomic state has to be prepared with high accuracy. In the experiment, the atom is optically pumped into the coherent dark state given by eqn (4.28). A residual magnetic field gives rise to a precession of the atomic states that counteracts the optical pumping process. In order to achieve a suitable pumping efficiency, the precession time has to be smaller than the timescale of the optical pumping process. Therefore, an initial compensation of the magnetic field is required.

For the compensation, we use the dependence of the pump efficiency on the magnetic field.
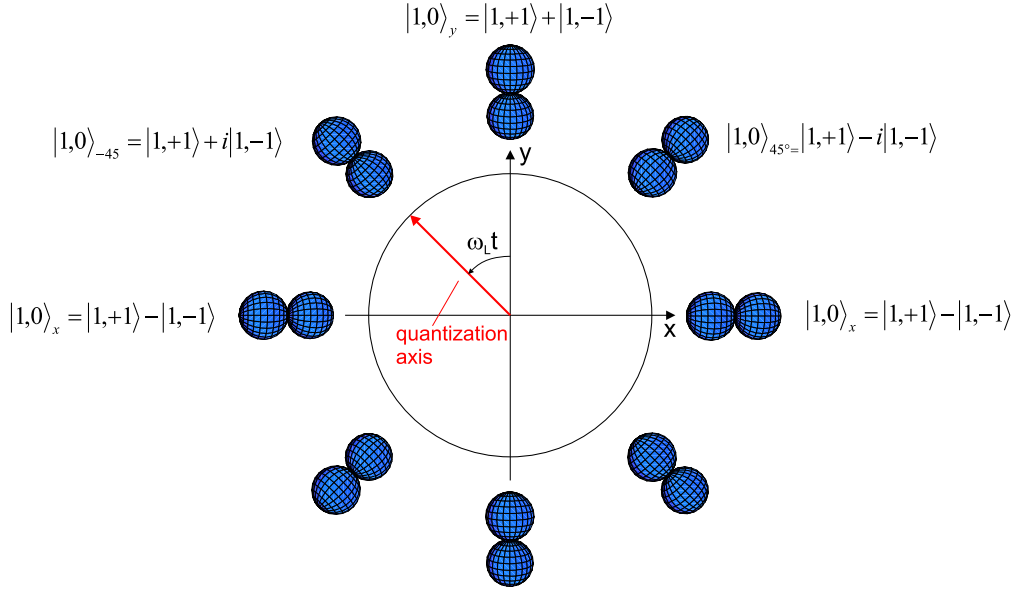
Figure 4.21.: Larmor precession of the state defined in eqn (4.28) in a magnetic field oriented along the quantization axis. In a rotating reference frame defined by the quantization axis at the angle $\omega_L t$, the atom stays in the $|1,0\rangle$ eigenstate. The figure shows the representation of the time dependent eigenstate in the laboratory reference frame, as well as the corresponding spin-1 orbital wavefunction.

Therefore, we apply pump light from one direction. The scattering of photons from the pump beam gives rise to a light pressure and a heating of the transversal velocity components of the atom, until it is lost from the trap or is transferred into the dark state. A residual magnetic field gives rise to a Larmor precession of the atom and therefore no stable dark state exists. In essence, higher magnetic fields result in a higher precession frequency and a higher scattering rate of photons, which leads to increased trap losses during the pump sequence. Measuring the survival probability of the atom as a function of the applied magnetic field allows to determine the external magnetic field at the position of the atom. Using different polarizations of the pump field all components of the magnetic field vector can be analyzed. Using these measurements, we were able to compensate the external magnetic field. In the end, we determined a residual magnetic field on the order of 150 mG, corresponding to a Larmor frequency of $\omega_L = 100$ kHz, low enough to allow efficient preparation of the initial superposition states. For a more detailed discussion of the magnetic field compensation see [104, 68].

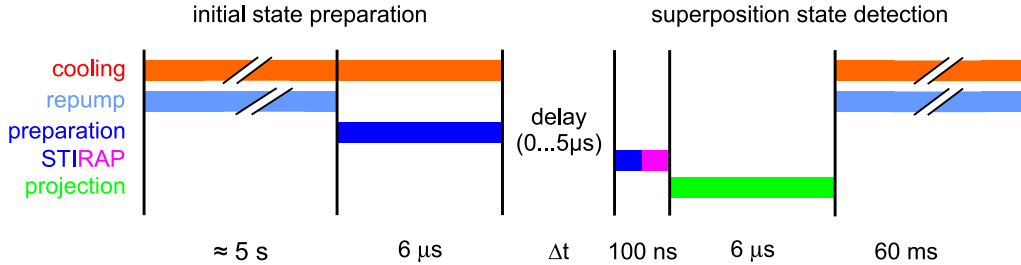**Experimental process and measurement results**

Figure 4.22.: Experimental process for the observation of Larmor precession. Two pump fields – resonant to the transitions $F = 1 \rightarrow F' = 1$ and $F = 2 \rightarrow F' = 1$ – together with the cooling laser, prepare the atom in the initial superposition state $|\Psi_L\rangle$ (see section 4.2.3). After the preparation, the magnetic moment undergoes Larmor precession until after a time delay $\Delta t = 0...5$ μs the superposition state detection projects the atom onto the two orthogonal states $|\Psi_L\rangle$ and $|\Psi_{L,\perp}\rangle$.

In the experiment, the initial state $|\Psi_L(0)\rangle$ is prepared using optical pumping. After the preparation, a variable time delay Δt is inserted before the superpostion state detection (Fig. 4.22). During the time Δt the magnetic moment of the atom undergoes Larmor precession in the external magnetic field. After the time delay the superposition state detection is performed for two different STIRAP polarizations projecting the atomic state onto $|\Psi_L(0)\rangle$ and the orthogonal superposition state $|\Psi_{L,\perp}\rangle$.

Figure 4.23 shows the measured transfer probability for both STIRAP light polarizations as a function of the time delay Δt. In each measurement, we observe an oscillation of the transfer efficiency for both STIRAP polarizations which is a clear signal of Larmor precession of the magnetic moment of the atom. The orientation of the magnetic field in our experiment is not exactly known, but in measurement (a) the z-component of the magnetic field dominates and the observed precession is similar to the theoretically expected behavior (Fig. 4.20). From the precession frequencies we determined the absolute magnetic field values. For the measurements presented in Fig. 4.23 we calculated an absolute magnetic field of (a) 142 mG, (b) 75 mG and (c) 62 mG, respectively.

The observation of the Larmor precession provides an accurate measure for the absolute value of the magnetic field at the position of the atom. Using different initial superposition states also the orientation of the magnetic field can be determined. Therefore, this analysis provides a highly sensitive procedure for the measurement (and compensation) of the magnetic fields in our experiment.
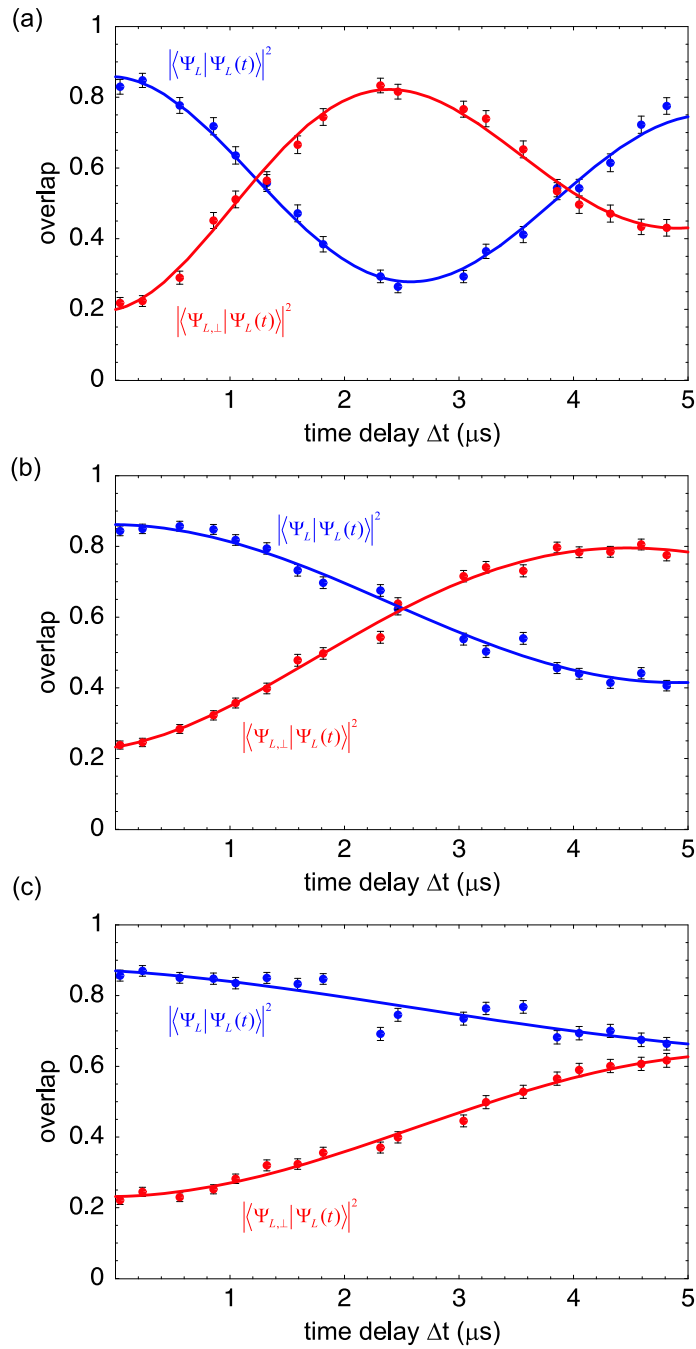
Figure 4.23.: Time dependent overlap of the precessing atomic state with the STIRAP eigenstates $|\Psi_L\rangle$ (blue curve) and $|\Psi_{L,\perp}\rangle$ (red curve) for three different magnetic fields.

4.4. Summary

This chapter described the realization of a detection scheme that allows to analyze coherent superpositions of internal atomic Zeeman levels by combining coherent dark state projection with the STIRAP technique. In essence, the polarization of the STIRAP light fields defines which superposition of the Zeeman sublevels $m_F = \pm 1$ of the $F = 1$ hyperfine ground level is transferred to the $F = 2$ ground level. Together with the hyperfine level detection, this scheme allows to analyze the atomic qubit in arbitrary measurement bases. The accuracy of the detection process was analyzed in detail. Therefrom we obtain a mean detection accuracy – the probability to correctly identify the atomic superposition state – of 95%. The high accuracy recommends the detection scheme for the application in the verification of atom-photon entanglement.

In the last part of this chapter we discussed an application of the state detection process, which allows to observe the precession of the magnetic moment of a single atom in an external magnetic field. The measured precession frequency provides a highly sensitive measure of the residual magnetic fields at the position of the atom and therefore can be used for an accurate compensation of magnetic bias fields.

5. Generation and verification of atom-photon entanglement

Contents

Entanglement is a key element for quantum communication and information applications [23]. For future applications like quantum networks or the quantum repeater [40] it is mandatory to achieve entanglement also between separated quantum systems. Therefore, entanglement between different quantum objects like atoms and photons [46] forms the interface between atomic quantum memories and photonic quantum communication channels [42, 43] and allows the distribution of quantum information over arbitrary distances. Furthermore, atom-photon entanglement allows the generation of entangled atoms at remote locations via entanglement swapping and therefore is the key element to a final loophole-free test of Bell's inequality [21, 22].

This chapter describes the generation of an entangled atom-photon state and the measurements necessary for the verification of entanglement. First, the single atom is prepared in the excited hyperfine level $5^2P_{3/2}$, $F' = 0$. Due to conservation of angular momentum in the subsequent spontaneous decay, entanglement between the polarization of the emitted photon and the angular momentum of the atom is generated. Next, in order to verify the entanglement, we use the superposition state detection described in chapter 4 to measure the internal atomic state in arbitrary measurement bases. Together with a polarization measurement of the emitted photon this allows to perform correlation measurements between the photon polarization and the internal atomic state in complementary measurement bases. With this technique we determined the density matrix of the combined atom-photon state. The results presented in this chapter, clearly show entanglement between the two particles and allow us to obtain the

entanglement fidelity of the generated state. Furthermore, we used the entangled state to test Bell's inequality in the CHSH-form [4], thereby observing a clear violation, which provides a further verification of entanglement between the two particles.

5.1. Generation of atom-photon entanglement

Atom-photon entanglement is generated due to conservation of angular momentum in the spontaneous decay of the excited hyperfine level $5^2P_{3/2}$, $F' = 0$. Thus, the faithfull preparation of the excited state and the time resolved detection of the emitted photon present crucial elements in the experimental realization of atom-photon entanglement.

   This chapter describes the advantages of the decay of the $5^2P_{3/2}$, $F' = 0$ excited state in comparison to other atomic transitions and presents the experimental scheme used to prepare the atom in the excited hyperfine level. The time resolved detection of the emitted photons allows to select the photons from the spontaneous emission and shows the expected exponential decay with the excited state lifetime of ^{87}Rb.

5.1.1. Properties of the excited state

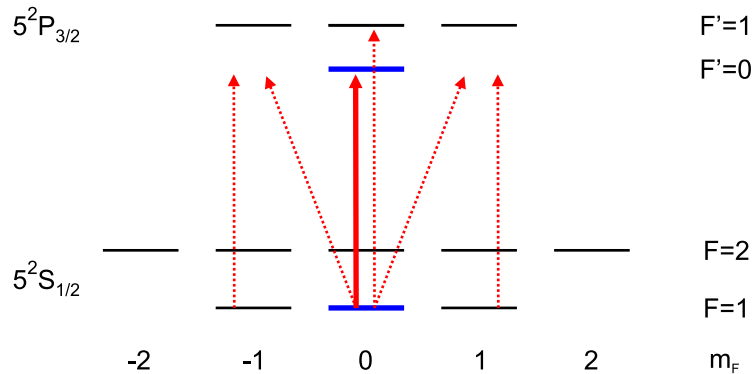
Figure 5.1.: Possible (straight line) and forbidden (dashed lines) transitions in the preparation of the excited hyperfine level $F' = 0$. Unwanted transitions, due to off-resonant excitation are not possible. Only off resonant excitation together with errors in polarization or optical pumping give rise to population transfer to the unwanted excited hyperfine states $F' = 1$, $m_F = \pm 1$.

   In order to create a maximally entangled atom-photon state in the spontaneous decay, the possible decay channels should form a Λ-type transition. In ^{87}Rb this can be realized in the

decay of the $5^2P_{3/2}$, $F' = 0$ excited state hyperfine level, if the emitted photons are collected along a well defined direction into a single mode fiber (see chapter 2).

An important advantage of the $F' = 0$ hyperfine level compared to other excited state hyperfine levels comes from the hyperfine and Zeeman substructure of the $5^2P_{3/2}$ level. Excitation to wrong Zeeman sublevels of the $F' = 0$ hyperfine level – due to inefficiencies in the optical pumping process or errors in the polarization of the excitation light pulse – are impossible, because no Zeeman substructure exists (see Fig. 5.1). Furthermore, due to selection rules of atomic dipole transitions, off-resonant excitation to the excited Zeeman sublevel $F' = 1$, $m_F = 0$ is forbidden. Therefore, only off-resonant excitation together with inefficiencies in the optical pumping or in combination with polarization errors of the excitation beam give rise to population in unwanted excited states. Thus, the preparation accuracy of the $F' = 0$ excited hyperfine level is very robust against variations in the experimental parameters. Small errors of experimental parameters only cause a reduced preparation efficiency (i.e. the probability to prepare the excited state). Nonetheless, the probability to prepare unwanted excited hyperfine levels remains negligible. Therefore, the $F' = 0$ hyperfine level is an optimal choice, that allows the generation of entangled atom-photon pairs with high accuracy.

5.1.2. Preparation of the excited state

In the experiment, the preparation of the excited hyperfine level $F' = 0$ is realized in two steps. First, optical pumping – using two light fields resonant to the transitions $F = 1 \rightarrow F' = 1$ and $F = 2 \rightarrow F' = 1$ – prepares the atom in the dark Zeeman ground state $F = 1$, $m_F = 0$ (see Fig. 5.2 (a)). To avoid populating an unwanted dark state in the $F = 2$ hyperfine level, we simultaneously use the cooling light of the MOT to redistribute the atomic population in the $F = 2$ ground level.

After the optical pumping, the atomic population is transferred to the excited state $F' = 0$ by a resonant optical π-pulse (see Fig. 5.2 (b)). A pulse length of approximately 20 ns assures a narrow frequency distribution of the exciting laser pulse, much smaller than the excited state hyperfine splitting of 72 MHz between the $F' = 0$ and $F' = 1$ hyperfine levels. This assures the faithfull addressing of the $F' = 0$ hyperfine level. Optimum transfer efficiency is achieved in the case where the atom undergoes half a Rabi-oscillation during the pulse duration and thus, all population is transferred to the excited state. In order to obtain the maximum excitation efficiency, we measured the probability to observe a photon from the spontaneous decay as a function of the intensity of the excitation light field (Fig. 5.4). While for small excitation power the detection probability is low, it reaches a maximum at a power of approximately 30 μW, when all atomic population is transferred to the excited state. For higher intensities the excitation efficiency reduces because the atomic population is transferred back to the ground state due to Rabi flopping.

The maximum probability to detect the photons from the spontaneous decay in Fig. 5.4 is 0.05%. Together with the (calculated) detection efficiency of fluorescence photons of 0.1% this yields a preparation efficiency of the excited state for the full process (optical pumping and excitation) of approximately 50%.
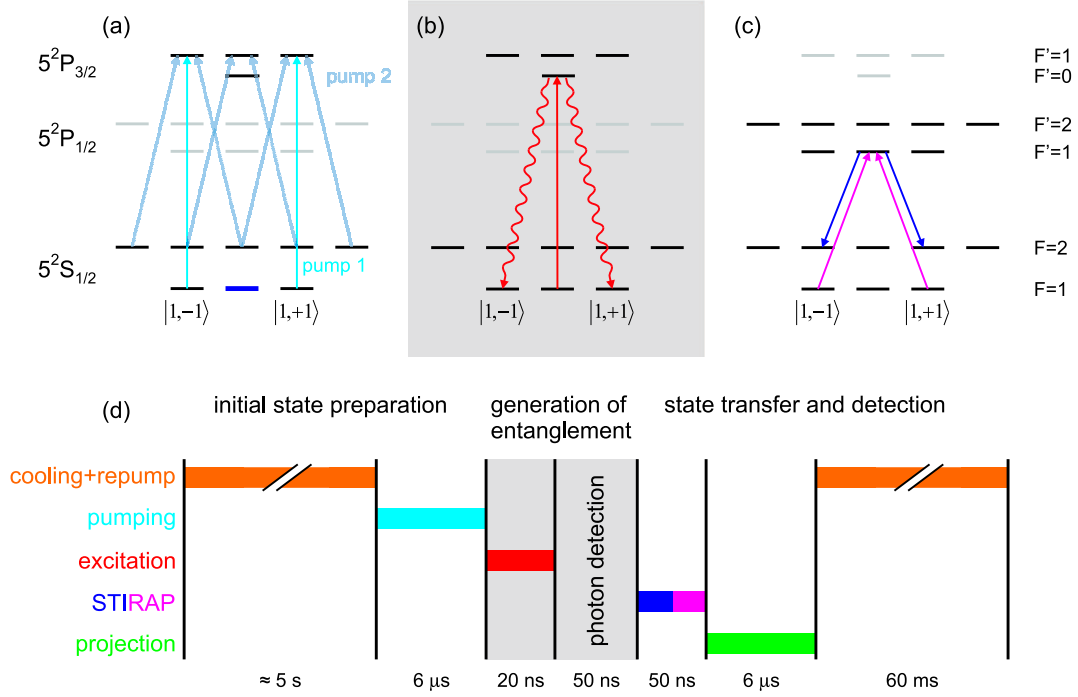
Figure 5.2.: Experimental scheme for the generation and verification of atom-photon entanglement. (a) Optical pumping using two light fields resonant to the transition $F = 1 \to F' = 1$ and $F = 2 \to F' = 1$ prepares the atom in the $F = 1$, $m_F = 0$ ground state. (b) After the optical pumping, a 20 ns optical π-pulse prepares the atom in the excited state hyperfine level $^2P_{3/2}$, $F' = 0$. In the following spontaneous decay, the polarization of the emitted photon is entangled with the magnetic sublevel $m_F = \pm 1$ of the $F = 1$ hyperfine level of the atomic ground state. (c) After the detection of the photon the atomic state detection is performed. Therefore, the STIRAP technique transfers a certain superposition state from the $F = 1$ to the $F = 2$ hyperfine level of the atomic ground state. Finally, the hyperfine level detection process determines the atomic hyperfine level which allows to deduce the initial atomic superposition state. (d) Timing sequence of the whole process (times not to scale).

5.1.3. Generation of entanglement

In the spontaneous decay from the $F' = 0$ excited state hyperfine level an entangled state between the polarization of the emitted photon and the angular momentum of the atom is
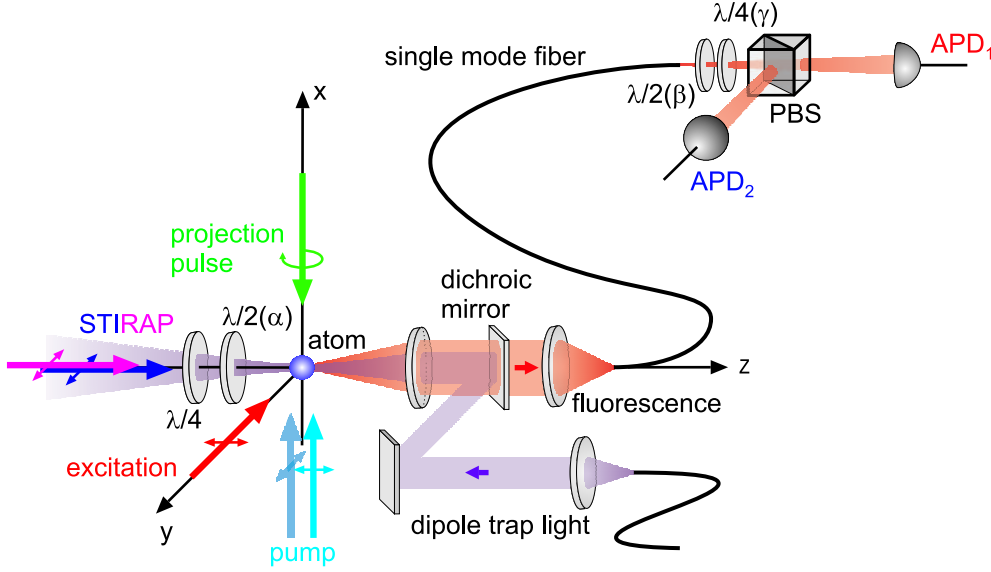
Figure 5.3.: Experimental setup for the generation and analysis of atom-photon entanglement. Optical pumping into the $F = 1$, $m_F = 0$ Zeeman sublevel and a subsequent excitation prepares the atom in the excited hyperfine level $5^2P_{3/2}$, $F' = 0$. In the following spontaneous decay, entanglement between the polarization of the emitted photon and the magnetic quantum number of the atom is created. The emitted photon is coupled into a single mode optical fiber. The fiber guides the light to the polarization analysis consisting of a quarter- and a halfwave plate to adjust the photon measurement basis and a polarizing beamsplitter with an APD in each output port. This allows both, the polarization measurement of the photon as well as the fluorescence detection of the single atom. After the photon detection, the STIRAP pulse sequence transfers a certain superposition of Zeemen sublevels to the $F = 2$ hyperfine ground level of the atom, followed by the hyperfine level detection scheme that allows to read out the atomic hyperfine level.

generated. Selecting only photons emitted along the z-direction (defined by our collection optics), the combined atom-photon state after the spontaneous emission reduces to (see chapter 2.2.4)

$$|\Psi\rangle = \frac{1}{\sqrt{2}} \left(|1, -1\rangle \left| \sigma^+ \right\rangle + |1, +1\rangle \left| \sigma^- \right\rangle \right). \tag{5.1}$$
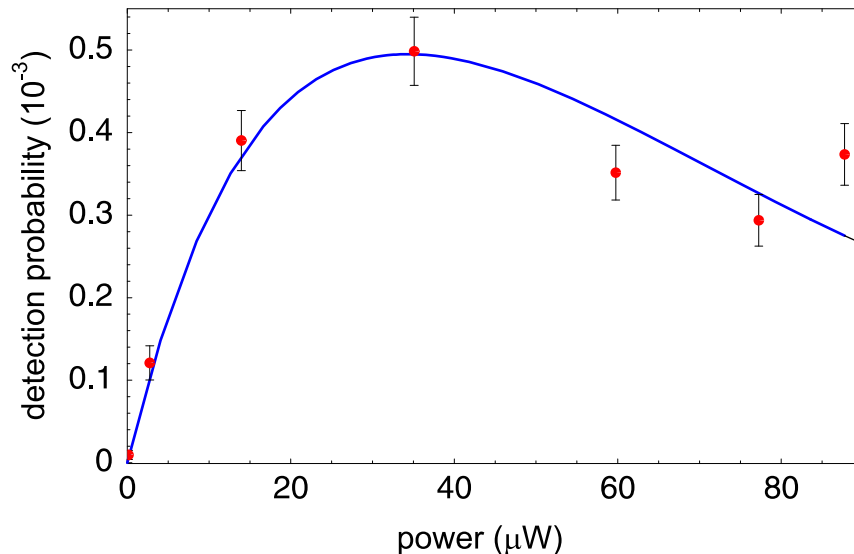
Figure 5.4.: Probability to detect a photon from the spontaneous decay as function of the power of the exciting laser pulse. For 30 μW the detection probability reaches a maximum of about 0.5% compatible with the collection and pump efficiency in our experiment [104]. The solid line represents a fit using a two-level model with the beam focus as free parameter.

The emitted photon is collected with a microscope objective and coupled into a single mode optical fiber guiding the light to our polarization analysis that consists of a rotatable quarter- and a halfwaveplate and a polarizing beamsplitter with an APD in each output port (Fig. 5.3). A homebuilt timestamp card (see appendix A.5.2) allows to detect the arrival time of photons with a time resolution of 2 ns. Integrating the measured single photon counts for approximately $1.4 \cdot 10^6$ measurement runs, yields the data presented in Fig. 5.5, showing the fluorescence observed in the optical pumping and the spontaneous decay. Fitting an exponential decay to the measurement data we obtain a decay time of 24 ± 2 ns. This is in good agreement with the excited state lifetime of ^{87}Rb of 26.2 ns.

Detecting a photon in one of the two APDs in a time window of approximately 80 ns (corresponding to three atomic lifetimes) indicates the generation of an entangled state and provides a polarization measurement of the photon. The generation of the entangled atom-photon state is probabilistic due to the limited total detection efficiency of the spontaneously emitted photons. In 0.05% of the preparation processes a photon is detected (see Fig. 5.4). Therefore, the pump-excitation cycle is repeated approximately 2000 times, until an emitted photons is detected[1].

---

[1]Repeating the optical pumping and excitation process leads to an increase of the kinetic energy of the atom. Therefore, a 200 μs optical cooling process is performed after 20 pump-excitation cycles.
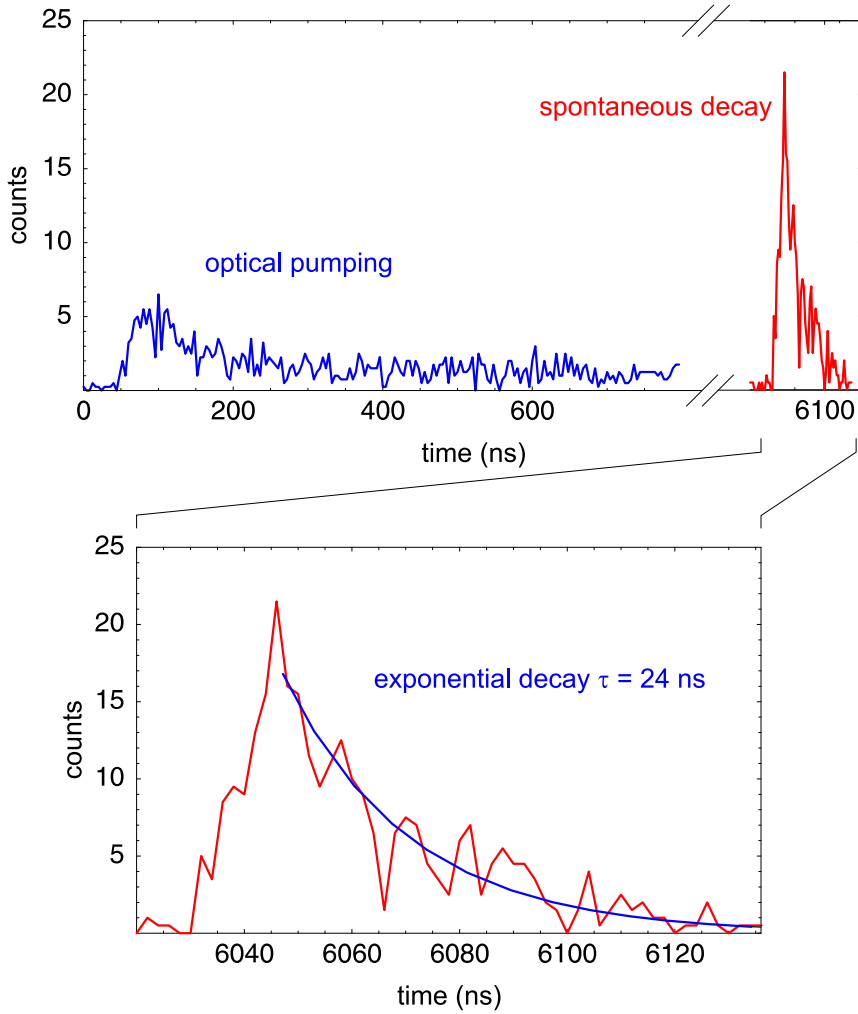
Figure 5.5.: Fluorescence observed from the optical pumping process (blue data) and the spontaneous decay of the excited state (red date). The photon detection events are collected from approximately $1.4 \cdot 10^6$ experimental cycles. The fluorescence observed from the optical pump process shows a maximum at the beginning of the pump sequence and decreases on a timescale of approximately 150 ns when the atom is pumped into the final Zeeman ground state $F = 1$, $m_F = 0$. After the excitation, the atomic population decays exponentially to the ground state (red curve). From a fit with an exponential decay we obtain a lifetime of 24 ± 2 ns which is in good agreement with the excited state lifetime of 26.2 ns.

5.2. Verification of entanglement

The spontaneous decay of the $5^2 P_{3/2}$, $F' = 0$ excited state hyperfine level generates entanglement between the polarization of the emitted photon and the spin degree of freedom of the single atom. In order to verify that the generated atom-photon state is truly entangled and not in a statistical mixture, we have to analyze spin correlations between the atom and the emitted photon. While the polarization measurement of the single photon can be performed in a straightforward way using polarizers aligned along suitable axes, the measurement of the atomic state has to be performed in a more sophisticated way using the superposition state detection presented in chapter 4. In this process, the polarization of the STIRAP transfer lasers defines the atomic measurement bases. Together with the polarization analysis of the photon, the atomic state detection enables a complete state tomography of the combined atom-photon state.

5.2.1. Atom-photon spin correlations

For the verification of entanglement it is necessary to analyse the combined atom-photon state in complementary measurement bases to rule out the possibility that quantum state consists of an incoherent mixture of separable states. Therefore, we analyzed correlations between the atomic spin state and the polarization of the photon for different photonic and atomic measurement bases.

Correlation for the atomic measurement bases $\hat{\sigma}_x$, $\hat{\sigma}_y$ and $\hat{\sigma}_z$

In order to verify entanglement, we measured correlations between the atomic angular momentum and the polarization of the photon for the three complementary atomic measurement bases $\hat{\sigma}_x$, $\hat{\sigma}_y$ and $\hat{\sigma}_z$, corresponding to a polarization of the STIRAP light field of H, $-45°$ and σ^+, respectively. Figure 5.6 shows the transfer probability of the STIRAP process as a function of the orientation of the photon polarization for the three different atomic measurement bases. In measurement (a) and (b) the halfwave plate in the photon polarization analysis is rotated by β and in measurement (c) the quarterwave plate was rotated by γ (see Fig. 5.3). Thus, the measured polarization states of the photon are

$$|\Psi_{ph}(\beta)\rangle = \frac{1}{\sqrt{2}} \left(|\sigma^+\rangle \pm e^{i4\beta} |\sigma^-\rangle \right) \tag{5.2}$$

$$|\Psi_{ph}(\gamma)\rangle = \cos(\gamma \pm \frac{\pi}{4}) |\sigma^+\rangle + \sin(\gamma \pm \frac{\pi}{4}) |\sigma^-\rangle, \tag{5.3}$$

where the $\pm$ sign correspond to the detection of the photon in APD$_1$ or APD$_2$, respectively. Using eqns (5.1), (5.2) and (5.3) we can calculate the corresponding states of the atom after the detection of the emitted photon:

$$|\Psi_{at}(\beta)\rangle = \frac{1}{\sqrt{2}} \left(|1,-1\rangle \pm e^{-4i\beta} |1,+1\rangle \right) \tag{5.4}$$

$$|\Psi_{at}(\gamma)\rangle = \cos(\gamma \pm \frac{\pi}{4}) |1,-1\rangle + \sin(\gamma \pm \frac{\pi}{4}) |1,+1\rangle. \tag{5.5}$$
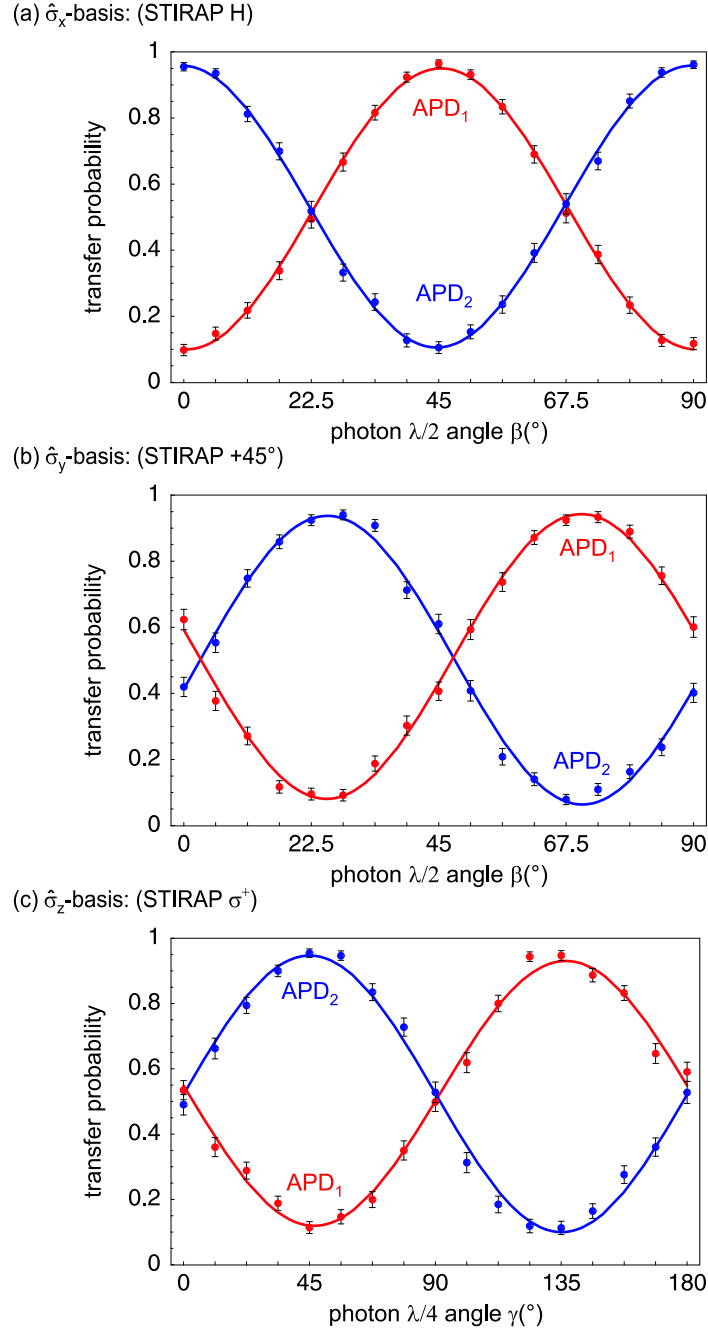
Figure 5.6.: Atom-photon spin correlations. The figure shows the transfer probability as a function of the photon analyzer setting, for an atomic state detection in (a) $\hat{\sigma}_x$-, (b) $\hat{\sigma}_y$- and (c) $\hat{\sigma}_z$-basis. The solid lines are sinusoidal fits to the measured data.

The polarization of the STIRAP light field defines which superposition of the atomic Zeeman sublevels $|1, \pm 1\rangle$ is transferred to the $F = 2$ hyperfine ground level and which superposition stays dark. Therefore, it defines the atomic measurement basis. For the measurements Fig. 5.6 (a)–(c) the STIRAP polarization H, $-45°$ and σ^+ corresponds to the atomic measurement basis $\hat{\sigma}_x$, $\hat{\sigma}_y$ and $\hat{\sigma}_z$, respectively, with the corresponding atomic dark states

$$|\Psi_D\rangle_H \quad = \quad \frac{1}{\sqrt{2}} \left(|1, -1\rangle + |1, +1\rangle \right) \tag{5.6}$$

$$|\Psi_D\rangle_{-45°} \quad = \quad \frac{1}{\sqrt{2}} \left(|1, -1\rangle - i\, |1, +1\rangle \right) \tag{5.7}$$

$$|\Psi_D\rangle_{\sigma^+} \quad = \quad |1, -1\rangle . \tag{5.8}$$

Therefore, after the photon detection we expect minimum (maximum) transfer probability if the atom is in a dark (bright) state relative to the STIRAP light field. The measurements in Fig. 5.6 (a), (b) and (c) show the expected behavior, where we observe minimum (maximum) transfer probability for $\beta = 0°$, $\beta = 22.5°$ and $\gamma = 45°$, respectively, after the detection of a photon in APD_1 (APD_2) corresponding to the presence of an atomic dark (bright) state.

The solid lines in the measurements are sinusoidal fits to the measured data. From the two fits of each measurement we obtain the visibilities (defined as peak to peak amplitude) $V_{\sigma_x} = 0.85 \pm 0.01$, $V_{\sigma_y} = 0.87 \pm 0.01$ and $V_{\sigma_z} = 0.83 \pm 0.01$ for measurement (a), (b) and (c), respectively. In the $\hat{\sigma}_z$ basis we observe a significantly smaller visibility. This is due to the higher degree of polarization errors present for this basis, because the atomic and photonic systems are analyzed using circular polarization.

The measured atom-photon correlations are in good agreement with the expected behavior and the occurrence of correlations in the three complementary measurement bases $\hat{\sigma}_x$, $\hat{\sigma}_y$ and $\hat{\sigma}_z$ is a clear signature of entanglement of the combined atom-photon state.

Correlation for variable atomic basis

For applications in quantum information and communication it is also interesting to perform atomic state measurements in bases that differ from the bases defined by the three Pauli-matrices $\hat{\sigma}_x$, $\hat{\sigma}_y$ and $\hat{\sigma}_z$. Therefore, we analyzed correlations for a fixed photon measurement basis ($\beta = \gamma = 0°$), and the atomic measurement basis was rotated in the x-y-plane by rotating the STIRAP polarization with a halfwave plate (angle α). The data obtained from this procedure (Fig. 5.7) shows maximum correlation for horizontal ($\alpha = 0°$) and vertical ($\alpha = \pm 45°$) STIRAP polarization, whereas no correlation is observed for an analysis in the complementary $\hat{\sigma}_y$-basis ($\alpha = \pm 22.5°$).

Summary

We analyzed the correlations between the polarization of the emitted photon from the spontaneous decay and the internal Zeeman sublevel of the atom for the three complementary atomic measurement bases $\hat{\sigma}_x$, $\hat{\sigma}_y$, and $\hat{\sigma}_z$ as wells as for a continuous variation of the atomic analyzer setting. The high visibility of these correlations in all measurement bases clearly shows, that the combined atom-photon state is entangled and is not a classical mixture of the possible decay channels.
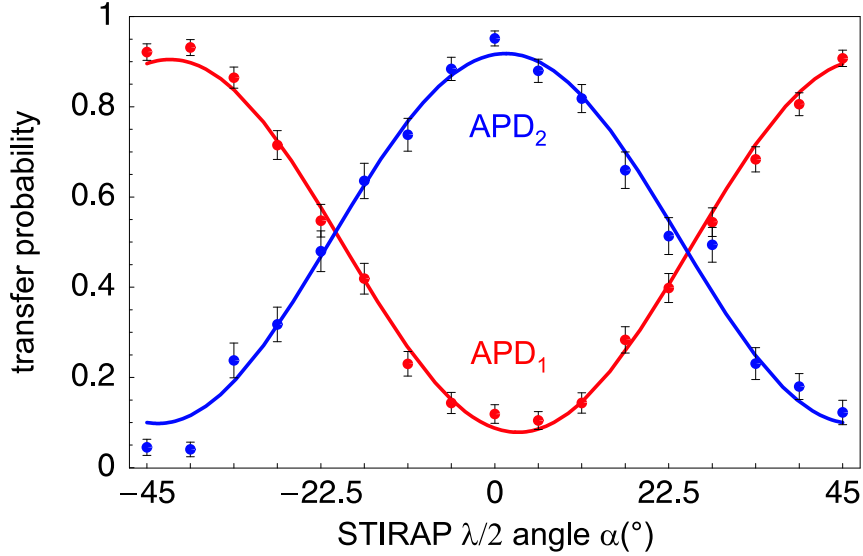
Figure 5.7.: Atom-photon spin correlations. The figure shows the transfer probability of the STIRAP process as a function of the setting of the halfwave plate defining the STIRAP polarization.

5.2.2. State tomography

The previous measurement results demonstrate that the combined atom-photon state is entangled. However, to verify that the generated state is similar to the theoretically expected state from spontaneous decay (eqn (5.1)) and to analyze the origin of the non-maximal visibility, a full state tomography has to be performed. From measuring spin-correlations for all combinations of the single particle measurement bases $\hat{\sigma}_x$, $\hat{\sigma}_y$ and $\hat{\sigma}_z$, we obtain the density matrix of the combined atom-photon state, which allows to identify the generated two-particle state and whether it is in a coherent superposition or an incoherent statistical mixture of the two decay channels.

Set of correlation measurements

The entangled atom-photon state is a two qubit state, therefore the corresponding density matrix ρ is a 4×4-matrix. Because ρ is Hermitian and normalized, the density matrix has 15 independent real parameters, that have to be obtained from the measurement. Therefore, we use the four single qubit operators $\hat{\sigma}_i = \hat{I}, \hat{\sigma}_x, \hat{\sigma}_y, \hat{\sigma}_z$ $(i = 0...3)$, that define a complete set of

orthogonal operators[2] for a single qubit state (where $\hat{I}$ is the identity). From these operators we obtain the 16 two-qubit operators $\hat{\sigma}_{ij} = \hat{\sigma}_i \otimes \hat{\sigma}_j$ that again form a complete orthogonal set for the four dimensional Hilbert space of the atom-photon state [105]. Therefore, any physical matrix can be expanded as sum of these operators and for the density matrix ρ the expansion yields

$$\rho = \frac{1}{4} \sum_{i,j=0}^{4} Tr(\rho \hat{\sigma}_{ij}) \hat{\sigma}_{ij} = \frac{1}{4} \sum_{i,j=0}^{4} \langle \hat{\sigma}_{ij} \rangle \hat{\sigma}_{ij} = \frac{1}{4} \sum_{i,j=0}^{4} \langle \hat{\sigma}_i \otimes \hat{\sigma}_j \rangle \hat{\sigma}_i \otimes \hat{\sigma}_j. \tag{5.9}$$

With the help of this expansion it is possible to obtain ρ experimentally from the measurement of the 16 spin correlations $\langle \hat{\sigma}_{ij} \rangle = \langle \hat{\sigma}_i \otimes \hat{\sigma}_j \rangle$. Defining the six single-qubit matrices $\hat{M}_i = \frac{1}{3} \pm \hat{\sigma}_x, \frac{1}{3} \pm \hat{\sigma}_y, \frac{1}{3} \pm \hat{\sigma}_z$, eqn (5.9) can be rearranged to

$$\rho = \sum_{i,j=1}^{6} c_{ij} \cdot \hat{M}_i \otimes \hat{M}_j, \tag{5.10}$$

where c_{ij} is directly the measured probability to obtain the joint result described by $\hat{M}_i$ and $\hat{M}_j$.

Atom-photon density matrix

In order to obtain the density matrix for the joint atom-photon state, we measured the two-qubit system in every combination of the three complementary bases $\hat{\sigma}_x$, $\hat{\sigma}_y$ and $\hat{\sigma}_z$ and using eqn (5.10) we obtained the atom-photon density matrix displayed in Fig. 5.8. This matrix is similar to the ideal density matrix of the pure entangled state in eqn (5.1), where the four central entries are equal to 0.5 and all other contributions are zero.

From the atom-photon density matrix we calculate the entanglement fidelity of the generated atom-photon state (defined as the overlap of the measured state ρ with the theoretical state in eqn (5.1)):

$$F = \langle \Psi | \rho | \Psi \rangle = \frac{1}{4} \left(1 + \sum_{i=1}^{3} \langle \Psi | \hat{\sigma}_i \otimes \hat{\sigma}_i | \Psi \rangle \right) = 0.87 \pm 0.01. \tag{5.11}$$

The fidelity agrees with the visibility observed in the correlation measurements in the preceeding chapter and shows the high degree of entanglement present in our system.

From the partial trace over the full atom-photon density matrix we can obtain the single particle density matrices $\rho_{ph} = \text{Tr}_{at}(\rho)$ of the single photon and $\rho_{at} = \text{Tr}_{ph}(\rho)$ of the single atom (see Fig. 5.9). For both cases, the off-diagonal elements vanish, corresponding to a complete statistical mixture. In contrast, the off-diagonal elements of the full atom-photon density matrix clearly show that the combined atom-photon state is in a coherent superposition of the possible decay channels and not in an incoherent mixture. This is expected according to quantum mechanics, where the single particles of an entangled pair are in no defined quantum state but in a maximal statistical mixture, in contrast to the entangled state itself, which is a well defined pure state.

---

[2]Two matrices are called orthogonal if $\text{Tr}(\sigma_i \sigma_j) = const \cdot \delta_{ij}$.
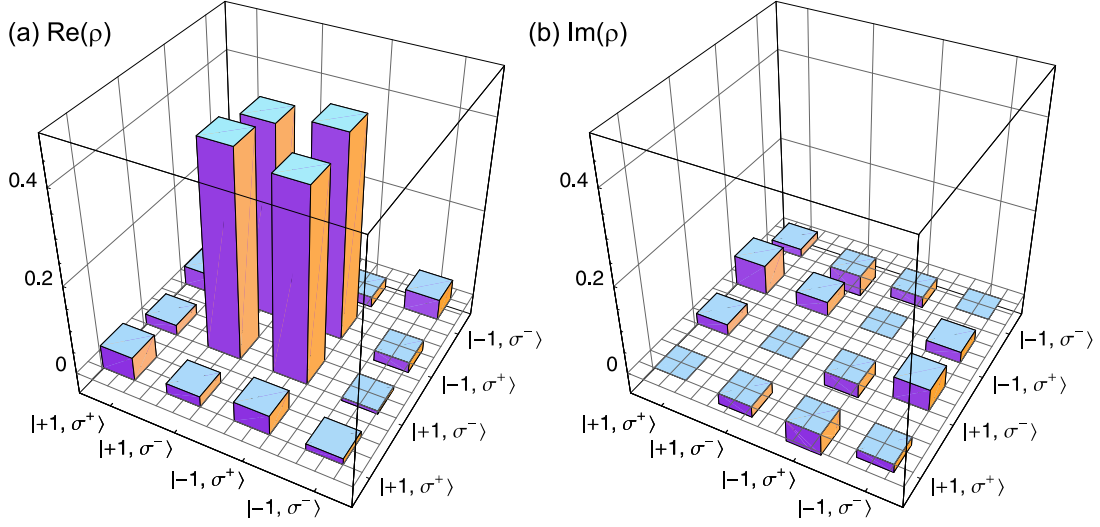
Figure 5.8.: Real and imaginary part of the density matrix ρ of the combined atom-photon state. The matrix is similar to the density matrix expected from the entangled state in eqn (5.1), where the real part of the four central values is 0.5, whereas all other contributions are zero.

5.2.3. Testing Bell's inequality

The observed correlations in complementary measurement bases as well as the full state tomography of the combined atom-photon state clearly verify, that the generated state is entangled. This allows to use the entangled state for certain applications as e.g. a test of Bell's inequality.

According to chapter 2, the predictions of local realistic theories disagree with the predictions of quantum mechanics for entangled states. This can be observed using Bell's inequality in the CHSH-form

$$S = |\langle \hat{\sigma}_\alpha \hat{\sigma}_\beta \rangle + \langle \hat{\sigma}_{\alpha'} \hat{\sigma}_\beta \rangle| + |\langle \hat{\sigma}_\alpha \hat{\sigma}_{\beta'} \rangle - \langle \hat{\sigma}_{\alpha'} \hat{\sigma}_{\beta'} \rangle| \leq 2, \tag{5.12}$$

which has to be fulfilled by local realistic theories, but is violated for a certain set of correlation measurements in quantum mechanics. Maximum violation is obtained for the STIRAP and photon analyzer settings of $\alpha = 0°$ and $\alpha' = 45°$ and $\beta = -22.5°$ and $\beta' = 22.5°$.

For each analyzer setting (α, β), we assign the values ± 1 to the binary measurement outcomes of the atomic state and photon polarization measurements. Thus, we obtain the four measurement quantities N_{++}, N_{+-}, N_{-+} and N_{--} from the total measurement number N, where the first and second subscript describes the result from the atomic and photonic state measurement, respectively. From these results we can calculate the two-particle expectation
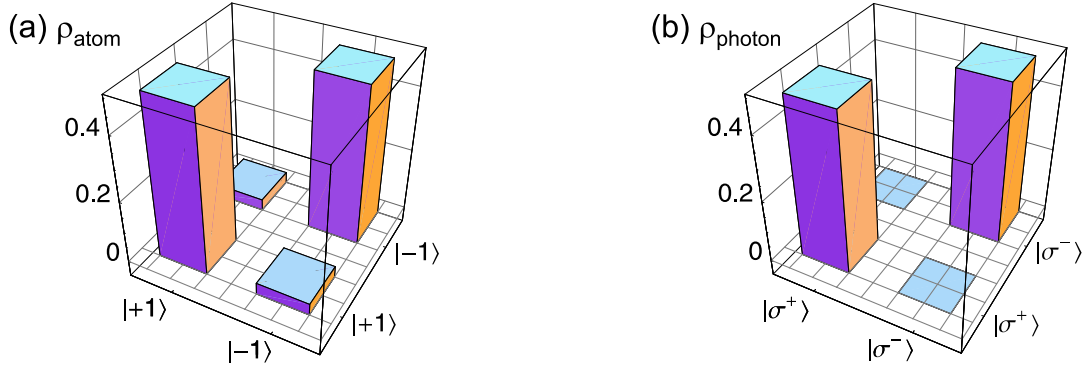
Figure 5.9.: Real part of the (a) atomic and (b) photonic single particle density matrix. Only vanishing off-diagonal elements can be observed corresponding to maximally mixed states.

values that are given by

$$\langle \sigma_\alpha \sigma_\beta \rangle = 2\frac{N_{++} + N_{--}}{N} - 1 = 1 - 2\frac{N_{+-} + N_{-+}}{N}. \tag{5.13}$$

| | result | $\beta = -22.5°$ | | $\beta' = 22.5°$ | |
		+1	−1	+1	−1
$\alpha = 0°$	+1	52	379	321	153
	−1	328	70	127	318
$\alpha' = 45°$	+1	389	87	420	49
	−1	99	331	65	389

Table 5.1.: Atom-photon correlation measurements. The entries in the table correspond to the number of detected atom-photon pairs with the respective measurement outcome.

Table 5.1 shows the number of atom-photon pairs that were detected with the respective measurement outcome for the different measurement bases α, α' and β, β'. Using eqn (5.12) and (5.13) we calculate

$$S = 2.44 \pm 0.05 \geq 2. \tag{5.14}$$

The measured value is larger than the maximum possible value of 2 for local realistic theories by 8.5 standard deviations, which clearly violates Bell's inequality and therefore contradicts

possible local realistic explanations. On the other hand, the violation of the inequality provides a further prove for the entangled nature of the combined atom-photon state and the measured violation is in good agreement with the visibility obtained from correlations measurements in chapter 5.2.1.

5.3. Summary

This chapter described the generation and verification of entanglement between a single atom and a single photon. Optical pumping, followed by a short excitation pulse prepared the atom in an excited state and conservation of angular momentum in the subsequent spontaneous decay generated entanglement between the polarization of the emitted photon and the angular momentum of the single atom.

Polarization measurements of the single photon and the atomic superposition state detection scheme described in chapter 4 allowed to measure correlations between the photon polarization and the internal atomic state. From correlation measurements in three complementary bases we obtain a mean visibility of better than 85% that clearly verifies that the generated state is entangled. A full state tomography of the combined atom-photon state has been performed, from which we derived the atom-photon density matrix and an entanglement fidelity of $F = 87\%$, i.e. the overlapp of the measured density matrix with the theoretically expected state from the spontaneous decay. The fidelity is consistent with our experimental errors and shows, that the state generated in the spontaneous decay is indeed in a coherent superposition of the two possible decay channels. The high fidelity of the entangled state allowed us to perform a test of Bell's inequality in the CHSH-form, where we obtained a value of $S = 2.44 \pm 0.05$ for the spin-correlation function, violating the CHSH-inequality by 8.5 standard devitations.

The measurement results presented in this chapter clearly prove, that the generated atom-photon state is truly entangled and indeed is the state we expect from spontaneous emission. This renders the entangled atom-photon state an ideal tool for many applications in quantum communication and information, where it allows to close the link between atomic quantum memories and photonic communication channels. Furthermore, it allows the generation of entangled atoms at remote locations via entanglement swapping. The high visibility observed in our experiment, should allow to generate an entangled state between two remote atoms with a degree of entanglement high enough to violate Bell's inequality. Together with the high efficiency of the atomic state detection, this would open up the possibility of a final loophole-free test of Bell's inequality.

6. Conclusion and Outlook

This thesis described the generation and verification of entanglement between the angular momentum of a single atom and the polarization of a spontaneously emitted single photon. A crucial step in the realization of atom-photon entanglement is the preparation of a single atom at a well defined position, isolated from the environment. Therefore, a far off-resonant optical dipole trap was set up, which allows to store a single ^{87}Rb atom up to several seconds. Due to the small volume of the trap a blockade mechanism occurs, limiting the maximum number of trapped atoms to one. Measuring the two-photon correlation function we observed strong photon antibunching which verifies the single atom characteristic of the dipole trap. In addition, the spectrum of the emitted resonance fluorescence was analyzed. Due to the Doppler effect, we observed a broadening of the single atom fluorescence spectrum from which we determined the mean kinetic energy of the trapped atom corresponding to a temperature of 105 μK.

Atom-photon entanglement is generated in the spontaneous decay from an excited hyperfine level to two possible atomic ground states that together form a Λ-type transition. For the verification of atom-photon entanglement it is necessary to analyze correlations between the polarization of the emitted photon and the internal state of the atom in complementary measurement bases. Therefore, we introduced a single atom state analysis using the STIRAP technique, where the polarization of the STIRAP light defines the atomic measurement basis. This detection method does not require additional atomic state manipulations and thus can be performed with increased fidelity and allowed us e.g. the observation of the Larmor precession of a single atom in a magnetic field.

Using the atomic state detection scheme, we measured spin correlations of the atom and the photon in complementary measurement bases. Furthermore, it allowed us to perform a full state tomography of the combined system from which we derived the density matrix of the atom-photon state. From these measurements we obtain a visibility of the spin correlations of better than 85% and an entanglement fidelity of 87%, which clearly show that the generated atom-photon state is entangled.

The atomic state detection method and the generation of high fidelity atom-photon entanglement form the basic elements in future quantum information experiments as e.g. the realization of an interface between atomic quantum computers and a photonic quantum communication channel [46, 42, 43]. Furthermore, the faithfull preparation of defined atomic superposition states is a crucial task of quantum information experiments. Quantum teleportation [33] of the state of a single photon onto the atom would allow the remote preparation of arbitrary states of an atomic quantum memory, by sending just two bits of classical information. A similar principle can be used in the "remote state preparation" protocol [106, 107]. Instead of teleporting the state of an external photon, an additional (spatial) degree of freedom is

imprinted onto the photon of the entangled atom-photon pair. A Bell-state measurement on the resulting two-qubit state of the single photon teleports its spatial degree of freedom onto the atom. Together with four defined unitary transformations, this allows the deterministic preparation of arbitrary atomic qubit states.
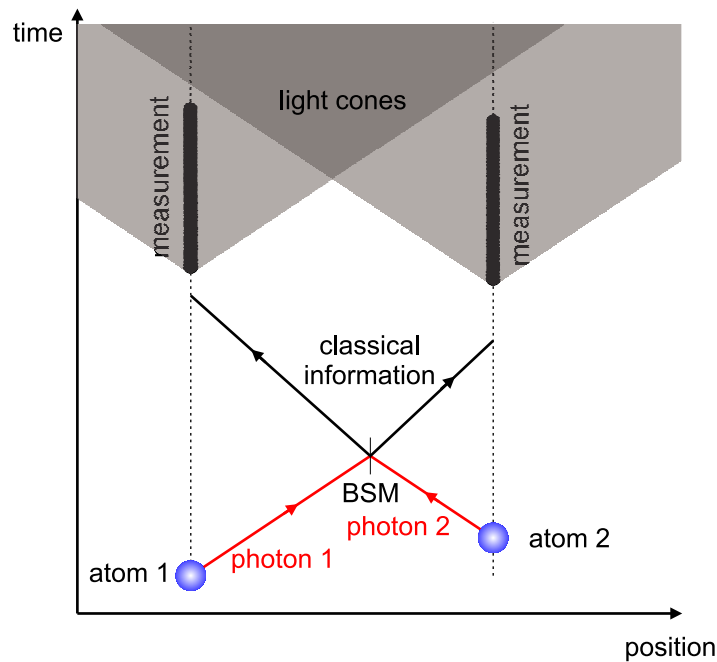
Loophole-free test of Bell's inequality

Figure 6.1.: Time-space diagram for the proposed loophole-free Bell test. The emitted photons travel to an intermediate location, where a Bell state measurement (BSM) projects the atoms onto an entangled state. The result of the BSM is sent back to the positions of the atoms and initiates the atomic state measurement, consisting of a random selection of the respective measurement basis and the atomic state detection. In order to close the locality loophole, the full measurement on the atomic states has to be finished, before information about the choice of measurement basis can arrive at the second observer. In this scheme, no fair sampling has to be applied, because every time a measurement of the entangled atom-atom state is performed, we obtain a result.

In addition, atom-photon entanglement is an important step towards a final, loophole-free test of Bell's inequality. Assuming we start with two atoms at remote locations and each of the atoms is entangled with a single photon. The photons propagate to an intermediate location, where a subsequent Bell-state measurement of the two photons projects the atoms into an entangled state [34, 22]. This would realize a so-called "event-ready scheme" [12, 20], where every time the Bell state analyzer gives a result one knows exactly that a pair of entangled atoms is present. Together with a detection efficiency of the internal atomic states of one – in the sense, that every state measurement of the atom yields a result (that however can be wrong) – and a space-like separation of the atoms relative to their measurement time, this would allow a final, loophole-free test of Bell's inequality (Fig. 6.1).

We can analyze the prospect of such a loophole-free Bell test with the experimental results obtained in this thesis. If we use the visibility observed in our experiment and extrapolate results of recent two-photon interference experiments[1] [108, 109, 85], we derive an expected atom-atom visibility of $V_{at-at} = V_{at-ph}^2 = 0.74 \pm 0.01$ [110]. Thus, the violation of a CHSH-type Bell inequality [4], which is achieved above the threshold visibility of 0.71, is feasible.

To close the locality loophole, the atoms have to be space-like separated with respect to the measurement time of the atomic states. Hence, the minimum distance of the atoms is determined by the duration of the whole measurement sequence, here mainly given by the atomic state detection. In detail, the atomic state is analyzed by scattering photons from the detection laser. Together with the STIRAP-process this yields an overall measurement time of less than 0.5 μs and requires a separation between the atoms of 150 m. This separation can easily be achieved since the transmission losses of photons at a wavelength of 780 nm in an optical fiber or air are low.

The generation of entangled atom-photon pairs is probabilistic with a success probability given by the total detection efficiency $\eta_{ph} = 0.05\%$ of the emitted photons. This also holds for the generation of entanglement between two distant atoms. The total success probability for the generation of atom-atom entanglement is given by $\frac{1}{4}\eta_{ph}^2 = 6 \cdot 10^{-8}$ where the factor 1/4 accounts for the case where only one of the four photon Bell-states is detected. The repetition rate of atom-photon entanglement is mainly determined by the preparation of the initial ground state, which should (according to the measured fluorescence data in Fig. 5.5) be possible in approximately 1 μs. Together with intermediate cooling cycles and the time duration of the entanglement swapping process, an average cycle time of approximately 2 μs should be possible. Including the limited lifetime of atoms in the dipole trap, this yields a generation rate of entangled atom-atom pairs of approximated 0.4 min^{-1}.

A loophole-free violation of e.g. a CHSH-type Bell's inequality by three standard deviations would require approximately 7000 atom pairs at the expected visibility of 0.74. From these estimations a loophole-free test should be feasible within a total measurement time of 12 days with (two times) the current setup.

---

[1]In comparison to related experiments [108, 109] using fiber beam splitters for a photon Bell-state analysis, we assume that the use of single-mode optical fibers together with the small bandwidth of the spontaneously emitted photons (possibly combined with a time resolved coincidence detection [85]) allows a fidelity of about 99% for the entanglement swapping process.

A. Appendix

Contents

A.1. Atom-light interaction

A.1.1. Quantization of the electromagnetic field

In order to obtain the quantum mechanical description of the electromagnetic field, one associates a harmonic oscillator with each mode $\lambda \mathbf{k}$ of the radiation field, where $\lambda = 1, 2$ corresponds

to the two orthogonal polarization modes and $\mathbf{k}$ is the wave vector of the light field. Using these definitions, one can define the annihilation and creation operators

$$\hat{a}_{\lambda,\mathbf{k}} |n_{\lambda\mathbf{k}}\rangle = \sqrt{n_{\lambda\mathbf{k}}} |n_{\lambda\mathbf{k}} - 1\rangle \tag{A.1}$$

$$\hat{a}_{\lambda,\mathbf{k}}^\dagger |n_{\lambda\mathbf{k}}\rangle = \sqrt{n_{\lambda\mathbf{k}} + 1} |n_{\lambda\mathbf{k}} + 1\rangle, \tag{A.2}$$

that destroy and create a photon of energy $\hbar\omega_k$ in the mode $|n_{\lambda\mathbf{k}}\rangle$, where $n_{\lambda\mathbf{k}}$ describes the number of photons in the respective mode. The electric field operator is given by

$$\hat{\mathbf{E}}(\mathbf{r}, t) = \hat{\mathbf{E}}^+(\mathbf{r}, t) + \hat{\mathbf{E}}^-(\mathbf{r}, t) \tag{A.3}$$

with

$$\hat{\mathbf{E}}^+(\mathbf{r}, t) = -i\sum_{\lambda,\mathbf{k}} \sqrt{\frac{\hbar\omega_k}{2\epsilon_0 V}} \mathbf{e}_{\lambda\mathbf{k}} \hat{a}_{\lambda,\mathbf{k}} e^{-i(\omega_k t - \mathbf{kr})} \tag{A.4}$$

$$\hat{\mathbf{E}}^-(\mathbf{r}, t) = +i\sum_{\lambda,\mathbf{k}} \sqrt{\frac{\hbar\omega_k}{2\epsilon_0 V}} \mathbf{e}_{\lambda\mathbf{k}} \hat{a}_{\lambda,\mathbf{k}}^\dagger e^{+i(\omega_k t - \mathbf{kr})}. \tag{A.5}$$

Here, $\mathbf{e}_{\lambda\mathbf{k}}$ is the unit vector along the field direction and V is the quantization volume.

Interaction Hamiltonian

Using the electric dipole approximation, the Hamiltonian $\hat{H}$ that describes a single atom interacting with a radiation field can be separated into three parts:

$$\hat{H} = \hat{H}_A + \hat{H}_R + \hat{H}_{ED} \tag{A.6}$$

where $\hat{H}_A$ and $\hat{H}_R$ are the Hamiltonians for the free atom and the radiation field which are given by

$$\hat{H}_A = \sum_i \hbar\omega_i |i\rangle\langle i| \tag{A.7}$$

$$\hat{H}_R = \sum_{\lambda,\mathbf{k}} \hbar\omega_k \left(\hat{a}_{\lambda,\mathbf{k}}^\dagger \hat{a}_{\lambda,\mathbf{k}} + \frac{1}{2} \right). \tag{A.8}$$

In eqn (A.7) $|i\rangle$ describes the internal atomic levels with energy $\hbar\omega_i$ and the radiation field is given by the operators $\hat{a}_{\lambda,\mathbf{k}}$ and $\hat{a}_{\lambda,\mathbf{k}}^\dagger$. The atom-light interaction Hamiltonian in the dipole approximation is given by

$$\begin{aligned} \hat{H}_{ED} &= \hat{\mathbf{d}} \cdot \hat{\mathbf{E}} \\ &= e \cdot i \sum_{\lambda,\mathbf{k}} \sum_{i,j} g_{ij\lambda\mathbf{k}} e^{i(\omega_i - \omega_j)t} \left(\hat{a}_{\lambda,\mathbf{k}} e^{-i\omega_k t} - \hat{a}_{\lambda,\mathbf{k}}^\dagger e^{+i\omega_k t} \right) |i\rangle\langle j| \end{aligned} \tag{A.9}$$

with the elementary charge e and the electric dipole operator $\hat{\mathbf{d}}$ consisting of the components $\mathbf{d}_{ij} = \langle i| \hat{\mathbf{d}} |j\rangle$ and the coupling coefficient

$$g_{ij\lambda\mathbf{k}} = \sqrt{\frac{\omega_k t}{2\hbar\epsilon_0 V}} \mathbf{e}_{\lambda\mathbf{k}} \mathbf{d}_{ij}. \tag{A.10}$$

Rotating wave approximation

For the following, we assume that the atomic energy levels $|i\rangle$ are sorted such that $\omega_j > \omega_i$ for $j > i$. Together with the fact that the dipole matrix elements $\hat{\mathbf{d}}_{\mathbf{ii}}$ vanish due to the odd parity of the electric dipole operator $\hat{\mathbf{d}}$, we can rearrange the terms in eqn (A.9) in the following way:

$$\hat{H}_{ED} = i\hbar \sum_{\lambda,\mathbf{k}} \sum_{j>i} \left(g_{ij\lambda\mathbf{k}} e^{+i\omega_{ji}t} |j\rangle\langle i| + g_{ij\lambda\mathbf{k}}^* e^{-i\omega_{ji}t} |j\rangle\langle i| \right) \left(\hat{a}_{\lambda,\mathbf{k}} e^{-i\omega_k t} - \hat{a}_{\lambda,\mathbf{k}}^\dagger e^{+i\omega_k t} \right), \quad \text{(A.11)}$$

where $\omega_{ji} = \omega_j - \omega_i$ are the atomic transition frequencies. Each summand in eqn (A.11) consists of four distinct terms. The term $|j\rangle\langle i| \cdot \hat{a}_{\lambda,\mathbf{k}}$ describes the excitation of the atom associated with the absorption of a photon while $|i\rangle\langle j| \cdot \hat{a}_{\lambda,\mathbf{k}}^\dagger$ describes the inverse process. The other two terms do not correspond to allowed absorption or emission events because they violate conservation of energy and therefore can be neglected. Using this approximation the interaction Hamiltonian is given by

$$\hat{H}_{ED} = i\hbar \sum_{\lambda,\mathbf{k}} \sum_{j>i} \left(g_{ij\lambda\mathbf{k}} |j\rangle\langle i| \hat{a}_{\lambda,\mathbf{k}} e^{-i\Delta\omega_{ijk}t} - g_{ij\lambda\mathbf{k}}^* |i\rangle\langle j| \hat{a}_{\lambda,\mathbf{k}}^\dagger e^{+i\Delta\omega_{ijk}t} \right) \quad \text{(A.12)}$$

where $\Delta\omega_{ijk} = \omega_{ij} - \omega_k$ is the detuning of the light relative to the atomic transition. The above approximation – the so-called rotating-wave approximation (RWA) – can also be derived in the semiclassical description with a quantum mechanical atom in a classical electromagnetic field by neglecting the rapid oscillatory terms.

A.1.2. Optical Bloch equations

In the interaction picture the time evolution of the density matrix σ of the combined atom-radiation state is described by the equation

$$\frac{d}{dt}\sigma(t) = -\frac{i}{\hbar}[\hat{H}_{ED}(t), \sigma(t)] \quad \text{(A.13)}$$

Recursive integration of this equation yields the expression

$$\begin{aligned}
\Delta\sigma(t) &= -i\hbar \int_t^{t+\Delta t} dt' [\hat{H}_{ED}(t'), \sigma(t)] + \\
&\quad + (-i\hbar)^2 \int_t^{t+\Delta t} dt' \int_t^{t'} dt'' [\hat{H}_{ED}(t'), [\hat{H}_{ED}(t''), \sigma(t'')]]
\end{aligned} \quad \text{(A.14)}$$

with

$$\Delta\sigma(t) = \sigma(t + \Delta t) - \sigma(t) \quad \text{(A.15)}$$

If the interaction H_{ED} is sufficiently small and Δt is short compared to the evolution time T of the atomic part ρ of the density matrix, $\sigma(t'')$ in eqn (A.14) one can approximately be replaced by $\sigma(t)$. The density matrix σ of the combined system can be split up into the two single density matrices $\rho = Tr_R\sigma$ and $\rho_R = Tr_A\sigma$ for the atom and radiation system, respectively:

$$\sigma(t) = \rho(t) \otimes \rho_R + \sigma_{correl}(t). \quad \text{(A.16)}$$

Here, $\sigma_{correl}(t)$ describes the correlation that exist between the atomic and the radiation system. To simplify the problem we assume that the radiation state ρ_R is time independent and that the correlations $\sigma_{correl}(t)$ disappear after a (very short) correlation time $\tau_c \ll \Delta t$ and therefore can be neglected. In the case where the radiation field is the vacuum state $\rho_R = |0\rangle \langle 0|$, one obtains for the evolution of the atomic density matrix [81]

$$\frac{d\rho_{aa}}{dt} = \sum_c^{\omega_c > \omega_a} \rho_{cc} \Gamma_{ca} - \sum_c^{\omega_a > \omega_c} \rho_{aa} \Gamma_{ac} \tag{A.17}$$

and

$$\frac{d\rho_{ab}}{dt} = - \left(\sum_n^{\omega_a > \omega_n} \frac{\Gamma_{an}}{2} + \sum_n^{\omega_b > \omega_n} \frac{\Gamma_{bn}}{2} \right) \rho_{ab}, \tag{A.18}$$

where the transition rates are given by

$$\Gamma_{ab} = \begin{cases} \frac{2\pi}{\hbar} \sum_{\mathbf{k},\lambda} |\langle a, \mathbf{k}\mathbf{e}_\lambda| \hat{H}_{ED} |b, 0\rangle|^2 \delta(\omega_k - \omega_{ba}) & \omega_a < \omega_b \\ 0 & \omega_a \geq \omega_b \end{cases}. \tag{A.19}$$

Bloch equations

In the above section we derived the equations of motion for a single atom in the electromagnetic vacuum. Now we assume the case, where a coherent electric field that for simplification is treated as classical is incident on the atom . Thus, the atom interacts with two fields: the incident classical field and the quantum mechanical radiation field in the vacuum state. In this approximation the Hamiltonian can be described by

$$\hat{H} = \hat{H}_A + \hat{H}_R - \hat{\mathbf{d}} \cdot (\mathbf{E}_{inc}(t) + \mathbf{E}_R) \tag{A.20}$$

where $\hat{H}_A$ and $\hat{H}_R$ are the atom and radiation Hamiltonians and $\mathbf{E}_{inc}$ and $\mathbf{E}_R$ describe the incident field and the quantum mechnical vacuum state, respectively. The external field is given by

$$\mathbf{E}_{inc} = \sum_k \mathbf{E}_{\mathbf{k}} \cos(\omega_k t) = \sum_k \frac{\mathbf{E}_{\mathbf{k}}}{2} \left(e^{i\omega_k t} + e^{-i\omega_k t} \right) \tag{A.21}$$

and the equation of motion in the interaction picture is

$$\dot{\rho} = -\frac{i}{\hbar}[\hat{\mathbf{d}} \cdot (\mathbf{E}_{inc}(t) + \mathbf{E}_R), \rho]. \tag{A.22}$$

To obtain an expression for the evolution of ρ we assume that both field contributions interact independently with the atom. In this case, the interaction of the atom with the external field $\mathbf{E}_{inc}$ is described in the RWA by

$$\hat{H}_{\tilde{E}D} = \hat{\mathbf{d}}\mathbf{E}_{inc}(t) = \frac{\hbar}{2} \sum_{k, j > i} \Omega_{ijk} |j\rangle \langle i| e^{-i\Delta\omega_{ijk} t} - \Omega_{ijk}^* |i\rangle \langle j| e^{+i\Delta\omega_{ijk} t} \tag{A.23}$$

with

$$\hbar\Omega_{ijk} = - \langle i| \hat{\mathbf{d}} |j\rangle \cdot \mathbf{E}_{\mathbf{k}} \tag{A.24}$$

and the detunings $\Delta\omega_{ijk} = \omega_{ij} - \omega_k$. The full description of the atomic density matrix ρ can be obtained by considering the interaction with the electromagnetic vacuum state, described by the damping terms in eqns (A.17) and (A.18). In this way we obtain the equation of motion of the atomic density matrix

$$\dot{\rho} = -\frac{i}{\hbar}[\hat{H}_{\tilde{E}D}, \rho] + R, \tag{A.25}$$

where the relaxation matrix R includes all relaxation effect from spontaneous decays and is given by

$$R_{a \neq b} = -\left(\sum_{n}^{\omega_a > \omega_n} \frac{\Gamma_{an}}{2} + \sum_{n}^{\omega_b > \omega_n} \frac{\Gamma_{bn}}{2} \right) \rho_{ab} \tag{A.26}$$

$$R_{aa} = \sum_{n}^{\omega_n > \omega_a} \rho_{nn} \Gamma_{na} - \sum_{n}^{\omega_a > \omega_n} \rho_{aa} \Gamma_{an}. \tag{A.27}$$

A.1.3. Two-level atom

Many effects in atomic physics are present in the simple case of a two-level atom consisting of an excited state $|e\rangle$ with decay rate Γ and a ground state $|g\rangle$. The energy of the excited state is $\hbar\omega_0$ and the frequency of the incident light field is ω. For the atomic state vector $(|e\rangle, |g\rangle)$ the interaction Hamiltonian is

$$\hat{H}_{\tilde{E}D} = \begin{pmatrix} 0 & \Omega e^{-i(\omega_0 - \omega)t} \\ \Omega e^{i(\omega_0 - \omega)t} & 0 \end{pmatrix} \tag{A.28}$$

and the relaxation matrix is given by

$$R = \begin{pmatrix} -\Gamma & -\frac{\Gamma}{2} \\ -\frac{\Gamma}{2} & \Gamma \end{pmatrix}. \tag{A.29}$$

In the stationary case ($\dot{\rho}_{ee} = \dot{\rho}_{gg} = 0$) one obtains the steady state solutions

$$\rho_{ee} = 1 - \rho_{gg} = \frac{s_0/2}{1 + s_0 + (2\Delta/\Gamma)^2} \tag{A.30}$$

$$\rho_{eg} = \rho_{ge}^* = i\frac{\Omega}{2(\Gamma/2 - i\Delta)(1 + \frac{s_0}{1+(2\Delta/\Gamma)^2})} \cdot e^{i\omega t} \tag{A.31}$$

where s_0 is the saturation parameter defined by

$$s_0 = 2\frac{|\Omega|^2}{\Gamma^2} = \frac{I}{I_s} \tag{A.32}$$

with the saturation intensity $I_s = \pi hc\Gamma/3\lambda^3$. For low saturation ($I \ll I_s$) the atomic population is mostly in the ground state, whereas in the case of high saturation ($I \gg I_s$) the excited state population ρ_{ee} approaches $1/2$. From eqn (A.30) one obtains an expression for the rate of photons scatted from the atom which is given by

$$\gamma = \Gamma\rho_{ee} = \Gamma\frac{s_0/2}{1 + s_0 + (2\Delta/\Gamma)^2}. \tag{A.33}$$

Optical cooling

For an atom in a traveling electromagnetic wave, a light pressure occurs due to the repeated absorption and emission of photons from the incident light field. In average, each absorption transfers the photon momentum $\hbar\mathbf{k}$ onto the atom, while the spontaneous emission is isotropic and therefore in average transfers no momentum onto the atom. Averaging over many absorption-emission cycles the mean force on the atom can be described by

$$\mathbf{F} = \hbar\mathbf{k}\Gamma\rho_{ee} = \hbar\mathbf{k}\Gamma\frac{s_0/2}{1 + s_0 + (2(\Delta + \omega_D)/\Gamma)^2}, \tag{A.34}$$

where $\omega_D = -\mathbf{k}\mathbf{v}$ is the Doppler shift due to the atomic velocity $\mathbf{v}$. For the case of two counterpropagating light beams the total force is approximately [67]

$$\mathbf{F_{tot}} = \frac{8\hbar k^2\Delta s_0}{\Gamma(1 + s0 + (2\Delta/\Gamma)^2)^2} \cdot \mathbf{v}_\parallel, \tag{A.35}$$

where $\mathbf{v}_\parallel$ is the projection of $\mathbf{v}$ on the direction of the incident light fields. For negative detuning ($\Delta < 0$) the force opposes the atomic velocity and thus gives rise to a damping of the atomic motion along the beam direction. This light induced damping is often called optical cooling or laser cooling. Generalizing this one dimensional scheme to a three-dimensional beam configuration allows to cool all velocity components of the atom.

The final atomic velocity can be calculated from the competition of the damping force in eqn (A.35) and the heating of the atomic velocity components due to the random direction of the spontaneous emission process. From this consideration one obtains the steady-state kinetic energy of the atom which is [67] $(\hbar\Gamma/8)(2|\Delta|/\Gamma + \Gamma/2|\Delta|)$. For $\Delta = -\Gamma/2$ this energy is minimal from which one obtains a minimum temperature of the laser cooling process (the so-called Doppler temperature) of

$$T_D = \frac{\hbar\Gamma}{2k_B}. \tag{A.36}$$

This is the minimum temperature that can be reached with the laser cooling process described above. Taking into account the Zeeman and hyperfine structure of the atom, further cooling techniques exist that allow to reach temperatures below the Doppler limit [67, 74].

Magneto optical traps

A trapping scheme widely used for neutral atoms is the magneto-optical trap (MOT) [61, 62] that relies on the position dependent Zeeman shift of the atomic transitions, induced by an external magnetic quadrupole field. For the following discussion we consider a two-level atom with an excited state $|e\rangle$ with angular momentum $F_e = 1$ and the corresponding Zeeman sublevels $m_e = \pm 1, 0$. The atomic ground state $|g\rangle$ has the angular momentum $F_g = 0$. The magnetic quadrupole field of the MOT generates a position dependent Zeeman shift of the three excited state Zeeman sublevels (see Fig. A.1). Two counterpropagating, red-detuned laser beams of opposite circular polarization are incident on the atom as depicted in Fig. A.1. If the atom is at a position $z < 0$, the transition to the excited Zeeman sublevel $m_e = +1$ will be shifted towards resonance and the atom scatters light mostly from the σ^+-polarized laser
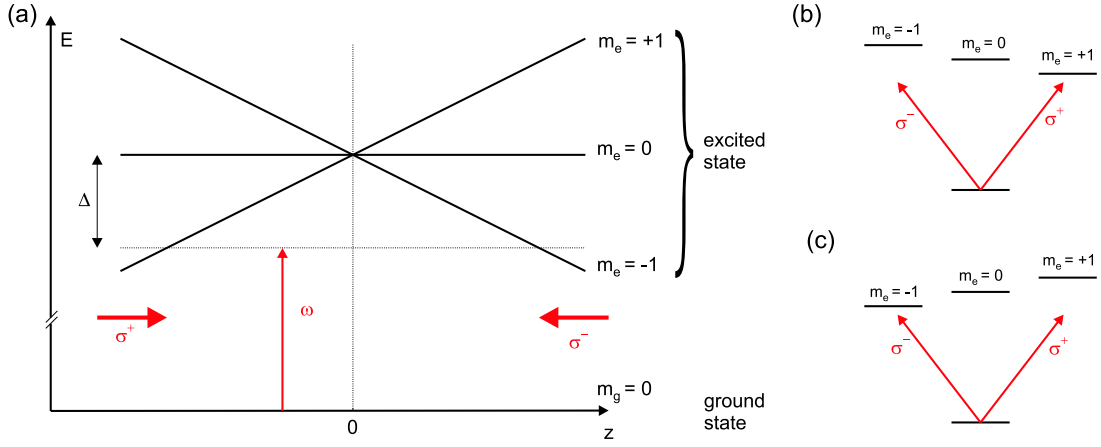
Figure A.1.: (a) Position dependent Zeeman shift of the atomic transitions in a linearly increasing magnetic field (with zero field at the position $z = 0$) as it occurs typically in a MOT. (b) Atomic level structure for $z < 0$ and (c) for $z > 0$.

beam. Thus, a light force towards the trap center ($z = 0$) appears. Similarly, an atom at $z > 0$ scatters light mostly from the σ^--polarized beam and is also driven towards the trap center. Using counterpropagating laser beams from all three spatial directions a three dimensional trapping mechanism occurs. Because the incident light fields are red-detuned relative to the atomic transition, magneto-optical traps also provide a laser cooling mechanism for the trapped atoms.

A.1.4. Four-level systems

In our experiment, the optical cooling process and the tripod-STIRAP scheme can not be described by a simple two-level system, whereas these processes can be well approximated by effective four-level systems. For a theoretical understanding of both processes we compared the theoretical predictions of our four-level models with the measured data. This section presents the interaction Hamiltonians and the corresponding relaxation matrices for both processes.

Laser cooling system

In the optical cooling process, the atom is approximated as a four level system with the two excited state hyperfine levels $|a\rangle$ and $|b\rangle$ and the two ground state hyperfine levels $|c\rangle$ and $|d\rangle$. Two light fields, the cooling light ω_{CL} – coupling the transition $|a\rangle \rightarrow |c\rangle$ – and the repump light ω_{RL} – coupling the transition $|b\rangle \rightarrow |d\rangle$ are incident on the atom (see Fig. 3.9). From

eqns (A.23), (A.26) and (A.27) we obtain for the interaction Hamiltonian

$$\hat{H}_{ED_c} = \begin{pmatrix} 0 & 0 & \Omega_{ca}e^{-i(\omega_{ca}-\omega_{CL})} & 0 \\ 0 & 0 & \Omega_{cb}e^{-i(\omega_{cb}-\omega_{CL})} & \Omega_{db}e^{-i(\omega_{db}-\omega_{RL})} \\ -\Omega_{ca}^*e^{i(\omega_{ca}-\omega_{CL})} & -\Omega_{cb}^*e^{i(\omega_{cb}-\omega_{CL})} & 0 & 0 \\ 0 & -\Omega_{db}^*e^{i(\omega_{db}-\omega_{RL})} & 0 & 0 \end{pmatrix} \quad (A.37)$$

and the relaxation term

$$R = \Gamma \cdot \begin{pmatrix} -\rho_{aa} & -\rho_{ab} & -\frac{1}{2}\rho_{ac} & -\frac{1}{2}\rho_{ad} \\ -\rho_{ba} & -\rho_{bb} & -\frac{1}{2}\rho_{bc} & -\frac{1}{2}\rho_{bd} \\ -\frac{1}{2}\rho_{ca} & -\frac{1}{2}\rho_{cb} & \rho_{aa}+\frac{1}{2}\rho_{bb} & 0 \\ -\frac{1}{2}\rho_{da} & -\frac{1}{2}\rho_{db} & 0 & \frac{1}{2}\rho_{bb} \end{pmatrix} \quad (A.38)$$

Tripod-STIRAP

Using a suitable reference frame and taking into account off-resonant transfer via the $5^2P_{1/2}$, $F' = 2$ excited hyperfine level, the STIRAP process in our experiment can be well approximated by an effective 4-level system (see Fig. 4.16). From eqns (A.23), (A.26) and (A.27) we obtain the interaction Hamiltonian

$$\hat{H}_{ED_c} = \begin{pmatrix} 0 & 0 & \Omega_{ca}e^{-i(\omega_{ca}-\omega_2)} & \Omega_{da}e^{-i(\omega_{da}-\omega_1)} \\ 0 & 0 & \Omega_{cb}e^{-i(\omega_{cb}-\omega_2)} & \Omega_{db}e^{-i(\omega_{db}-\omega_1)} \\ -\Omega_{ca}^*e^{i(\omega_{ca}-\omega_2)} & -\Omega_{cb}^*e^{i(\omega_{cb}-\omega_2)} & 0 & 0 \\ -\Omega_{da}^*e^{i(\omega_{da}-\omega_1)} & -\Omega_{db}^*e^{i(\omega_{db}-\omega_1)} & 0 & 0 \end{pmatrix} \quad (A.39)$$

and the relaxation matrix

$$R = \Gamma \cdot \begin{pmatrix} -\rho_{aa} & -\rho_{ab} & -\frac{1}{2}\rho_{ac} & -\frac{1}{2}\rho_{ad} \\ -\rho_{ba} & -\rho_{bb} & -\frac{1}{2}\rho_{bc} & -\frac{1}{2}\rho_{bd} \\ -\frac{1}{2}\rho_{ca} & -\frac{1}{2}\rho_{cb} & \frac{1}{2}\rho_{aa}+\frac{5}{6}\rho_{bb} & 0 \\ -\frac{1}{2}\rho_{da} & -\frac{1}{2}\rho_{db} & 0 & \frac{1}{2}\rho_{aa}+\frac{1}{6}\rho_{bb} \end{pmatrix}. \quad (A.40)$$

Here, $|a\rangle$ and $|b\rangle$ describe the Zeeman sublevels – involved in the STIRAP process – of the excited hyperfine level $F' = 2$ and $F' = 1$, respectively. The participating Zeeman sublevels of the $F = 2$ and $F = 1$ ground state hyperfine levels are described by $|c\rangle$ and $|d\rangle$, respectively. The incident STIRAP light fields ω_1 and ω_2 couple the transitions from the $F = 1$ respective $F = 2$ ground state to both excited states. Spontaneous decay of the atom into other Zeeman sublevels is ignored.

A.2. Spin-1 angular momentum

A.2.1. Matrix representation of the angular momentum operators

In quantum mechanics the angular momentum is represented by the operators $\hat{\mathbf{J}}^2$ and $\hat{J}_z$, that describe (the square of) the absolute value of the angular momentum and its projection onto the z-axis. For a spin-1 system ($\langle\hat{\mathbf{J}}^2\rangle = 2\hbar$), the operator $\hat{J}_z$ has three eigenstates with the corresponding eigenvalues 0, ± 1, which are given by

$$|\Psi_z\rangle_{+1} = |+1\rangle \tag{A.41}$$

$$|\Psi_z\rangle_0 = |0\rangle \tag{A.42}$$

$$|\Psi_z\rangle_{-1} = |-1\rangle . \tag{A.43}$$

Representing spin-1 states by the three dimensional vectors ($|+1\rangle, |0\rangle, |-1\rangle$) the angular momentum operators $\hat{J}_x$, $\hat{J}_y$ and J_z are given by the matrices

$$\hat{J}_x = \frac{\hbar}{\sqrt{2}} \begin{pmatrix} 0 & 1 & 0 \\ 1 & 0 & 1 \\ 0 & 1 & 0 \end{pmatrix}, \tag{A.44}$$

$$\hat{J}_y = \frac{\hbar}{\sqrt{2}} \begin{pmatrix} 0 & -i & 0 \\ i & 0 & -i \\ 0 & i & 0 \end{pmatrix} \text{ and} \tag{A.45}$$

$$\hat{J}_z = \hbar \begin{pmatrix} 1 & 0 & 0 \\ 0 & 0 & 0 \\ 0 & 0 & -1 \end{pmatrix}. \tag{A.46}$$

A.2.2. Angular momentum eigenstates

The operator of the angular momentum along the unit vector

$$\mathbf{u} = \begin{pmatrix} \sqrt{1-z^2}\cos\phi \\ \sqrt{1-z^2}\sin\phi \\ z \end{pmatrix} \tag{A.47}$$

is given by $\hat{J}_\mathbf{u} = \hat{\mathbf{J}} \cdot \mathbf{u}$, where $z\epsilon[-1,1]$ and ϕ are cylindrical coordinates. The eigenvectors of $\hat{J}_\mathbf{u}$ are the corresponding angular momentum eigenstates, given by

$$|\Psi_{z,\alpha}\rangle_{+1} = e^{-i\phi}\frac{1+z}{2}|+1\rangle + \sqrt{\frac{1-z^2}{2}}|0\rangle + e^{i\phi}\frac{1-z}{2}|-1\rangle \tag{A.48}$$

$$|\Psi_{z,\phi}\rangle_0 = -e^{-i\phi}\sqrt{\frac{1-z^2}{2}}|+1\rangle + z|0\rangle + e^{i\phi}\sqrt{\frac{1-z^2}{2}}|-1\rangle \tag{A.49}$$

$$|\Psi_{z,\phi}\rangle_{-1} = e^{-i\phi}\frac{1-z}{2}|+1\rangle - \sqrt{\frac{1-z^2}{2}}|0\rangle + e^{i\phi}\frac{1+z}{2}|-1\rangle . \tag{A.50}$$

Eigenstates to $\hat{J}_x$ and $\hat{J}_y$

From eqns (A.48-A.50) the eigenstates of $\hat{J}_x$ can be calculated and are given by

$$|\Psi_x\rangle_{+1} = \frac{1}{2}\left(|+1\rangle + \sqrt{2}\,|0\rangle + |-1\rangle\right) \tag{A.51}$$

$$|\Psi_x\rangle_0 = \frac{1}{\sqrt{2}}\left(-\,|+1\rangle + |-1\rangle\right) \tag{A.52}$$

$$|\Psi_x\rangle_{-1} = \frac{1}{2}\left(|+1\rangle - \sqrt{2}\,|0\rangle + |-1\rangle\right). \tag{A.53}$$

The eigenstates to $\hat{J}_y$ are accordingly

$$|\Psi_y\rangle_{+1} = \frac{1}{2}\left(-i\,|+1\rangle + \sqrt{2}\,|0\rangle + i\,|-1\rangle\right) \tag{A.54}$$

$$|\Psi_y\rangle_0 = \frac{i}{\sqrt{2}}\left(|+1\rangle + |-1\rangle\right) \tag{A.55}$$

$$|\Psi_y\rangle_{-1} = \frac{1}{2}\left(-i\,|+1\rangle - \sqrt{2}\,|0\rangle + i\,|-1\rangle\right) \tag{A.56}$$
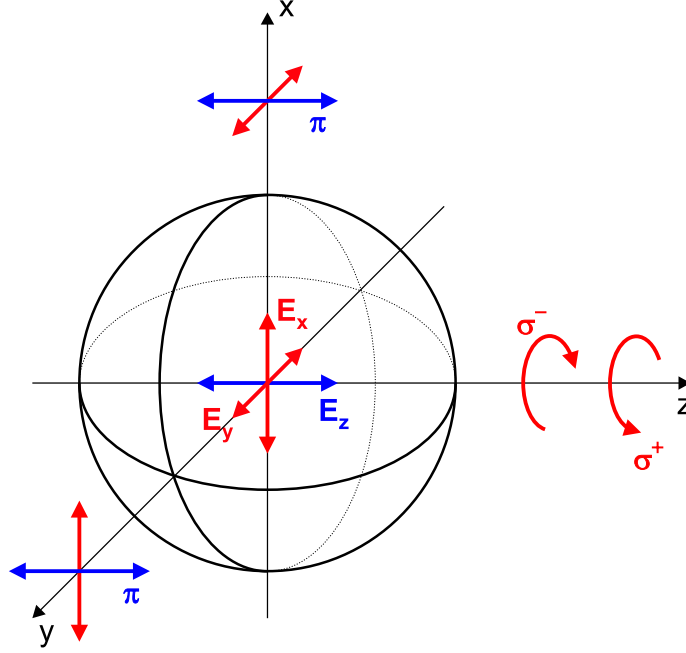
A.3. Definition of the polarization modes

Figure A.2.: Definition of polarization states in the atomic system.

The polarization of the light emitted by a single atom can be described by a superposition of the fields $\mathbf{E_x}$, $\mathbf{E_y}$ and $\mathbf{E_z}$[1] emerging from the three atomic dipoles oriented along the x-, y-, and z-axis. A different basis (used throughout this thesis) can be obtained using the following definitions

$$
\begin{aligned}
\boldsymbol{\sigma}^+ &= \tfrac{1}{\sqrt{2}} \left(\mathbf{E_x} + i\mathbf{E_y} \right) & \text{(A.57)} \\
\boldsymbol{\sigma}^- &= \tfrac{1}{\sqrt{2}} \left(\mathbf{E_x} - i\mathbf{E_y} \right) & \text{(A.58)} \\
\boldsymbol{\pi} &= \mathbf{E_z}. & \text{(A.59)}
\end{aligned}
$$

Setting the quantization axis of our system in z-direction this is the natural basis, because for this case the polarization states $\boldsymbol{\sigma}^\pm$ and $\boldsymbol{\pi}$ directly correspond to the angular momentum eigenstates $m = \pm 1$ and $m = 0$. For a photon emitted in z-direction, $\boldsymbol{\sigma}^+$-polarization e.g. corresponds to positive helicity, i.e. the photon is in the spin state $|m_f = 1\rangle$.

---

[1]$\mathbf{E_{(x,y,z)}} = \mathbf{E_{(x,y,z),0}} \cos(\omega t - k(x,y,z))$

A.4. Error estimation

In order to get an estimation for the statistical errors in the atomic state detection we use the following method. Each atomic state measurement yields the binary result *"atom in the trap"* or *"no atom in the trap"* which occurs with the probability p_{in} and $p_{out} = 1 - p_{in}$, respectively. Repeating the measurement N times, the probability $p(k)$ to observe k times the event *"atom in the trap"* is according to the binomial distribution given by

$$p(k) = \binom{N}{k} \cdot p_{in}^k \cdot (1 - p_{in})^{N-k}. \tag{A.60}$$

In the experiment, we measure the relative frequency

$$\tilde{p}_{in} = \frac{N_{in}}{N} \tag{A.61}$$

from which we want to estimate the unknown probability p_{in}. For a large number of measurements ($N\tilde{p}_{in}, N(1 - \tilde{p}_{in}) \gg 7$), $\tilde{p}_{in}$ is a good approximation of the probability p_{in} [111] and its scatter is given by the standard deviation of the measured distribution

$$\sigma = \sqrt{\frac{\tilde{p}_{in}(1 - \tilde{p}_{in})}{N}}. \tag{A.62}$$

This standard deviation is used for the description of the experimental errors throughout this thesis.

A.5. Measurement electronics

A.5.1. Pattern generator

For the control of the experimental process a pattern generator [112] is used that allows to switch the different laser systems on and off on a timescale of 20 ns. The pattern generator consists of four MByte RAM organized in 64 bit words that can be loaded from a computer via the parallel port. Each word contains 48 data bits used for the experimental control (on/off switching of the laser beams, generation of electronic control signals), 15 bits define the address of the next word and the last bit defines the duration of the current bit pattern (20 ns or 2 μs). The upper 4 bits of the address of the pattern can be accessed from the outside and thus allow the pattern generator to react to external events as e.g. the detection of the spontaneously emitted photon.

In the experiment, the loading of atoms into the trap (typically timescale 50 ms) is controlled by a personal computer. After the detection of a fluorescence signal exceeding the background level (indicating the presence of an atom in the trap) the control is handed over to the pattern generator controlling the entangling sequence and the subsequent atomic state detection.

A.5.2. Time tagging unit

The data accumulated in our experiments consists mainly of atomic fluorescence which is detected by avalanche photo diodes. The actual data collection is realized in a time tagging unit with four input ports that allow to distinguish four different detection events. By ascribing a time tag (with a resolution of 2 ns) to each event, the time tagging unit generates a list of photon events, that finally is transferred to a personal computer.

In order to identify the important detection events (as e.g. the single photon from the spontaneous decay) we use synchronization signals that are sent from the pattern generator to one input of the time tagging unit.
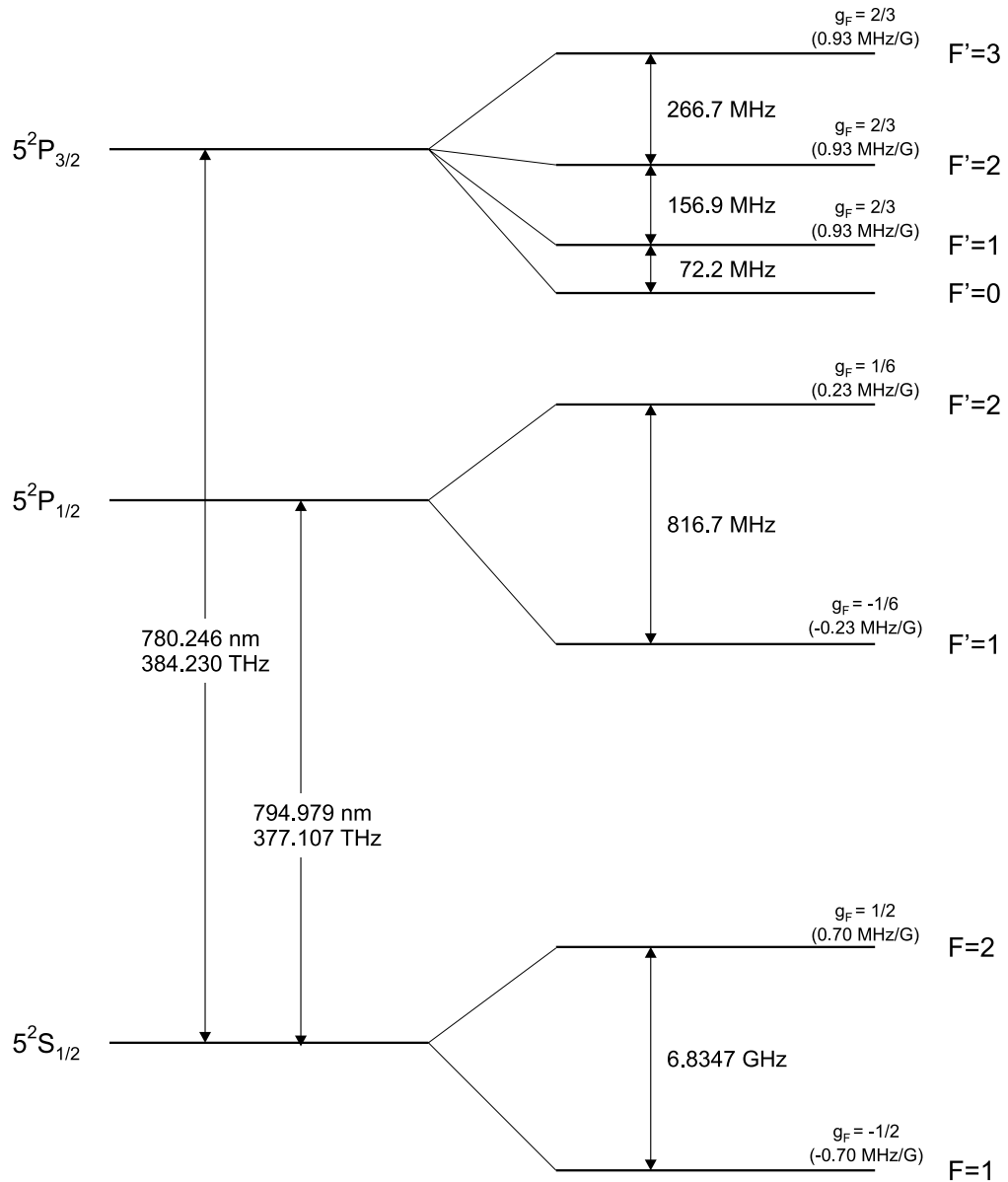
A.6. Rubidium data

A.6.1. Hyperfine structure

Figure A.3.: Hyperfine structure of the D_1 and D_2 transitions of ^{87}Rb [75].

A.6.2. Data

Atomic number	Z	37
Total nucleons	Z + N	87
Relative natural abundance		27.83(2)%
Nuclear spin	I	3/2
Atomic mass	M	86.9092 u
Vacuum wavelength D_1-transition	λ_{D_1}	794.979 nm
Vacuum wavelength D_2-transition	λ_{D_2}	780.246 nm
Lifetime $5^2P_{1/2}$	τ_{D_1}	27.70 ns
Lifetime $5^2P_{3/2}$	τ_{D_2}	26.24 ns
Natural line width D_1-transition	Γ_{D_1}	$2\pi \times 5.746(8)$ MHz
Natural line width D_2-transition	Γ_{D_2}	$2\pi \times 6.065(9)$ MHz
Ground state hyperfine splitting	ν_{HFS}	6834.68 MHz
Recoil velocity D_2-transition	v_R	5.885 mm/s
Recoil temperature D_2-transition	T_R	361.95 nK
Doppler velocity D_2-transition	v_D	11.75 cm/s
Doppler temperature D_2-transition	T_D	146 μK
Dipole matrix element D_2-transition	$\langle J| \hat{d} |J'\rangle$	$3.584(4) \times 10^{-29}$ Cm
Saturation intensity $5^2S_{1/2}, F = 2, m_F = \pm 2 \rightarrow$ $5^2P_{3/2}, F = 3, m_F = \pm 3$	I_{sat}	1.67 mW/cm^2

Table A.1.: Physical properties of ^{87}Rb [75].

A.7. Experimental setup
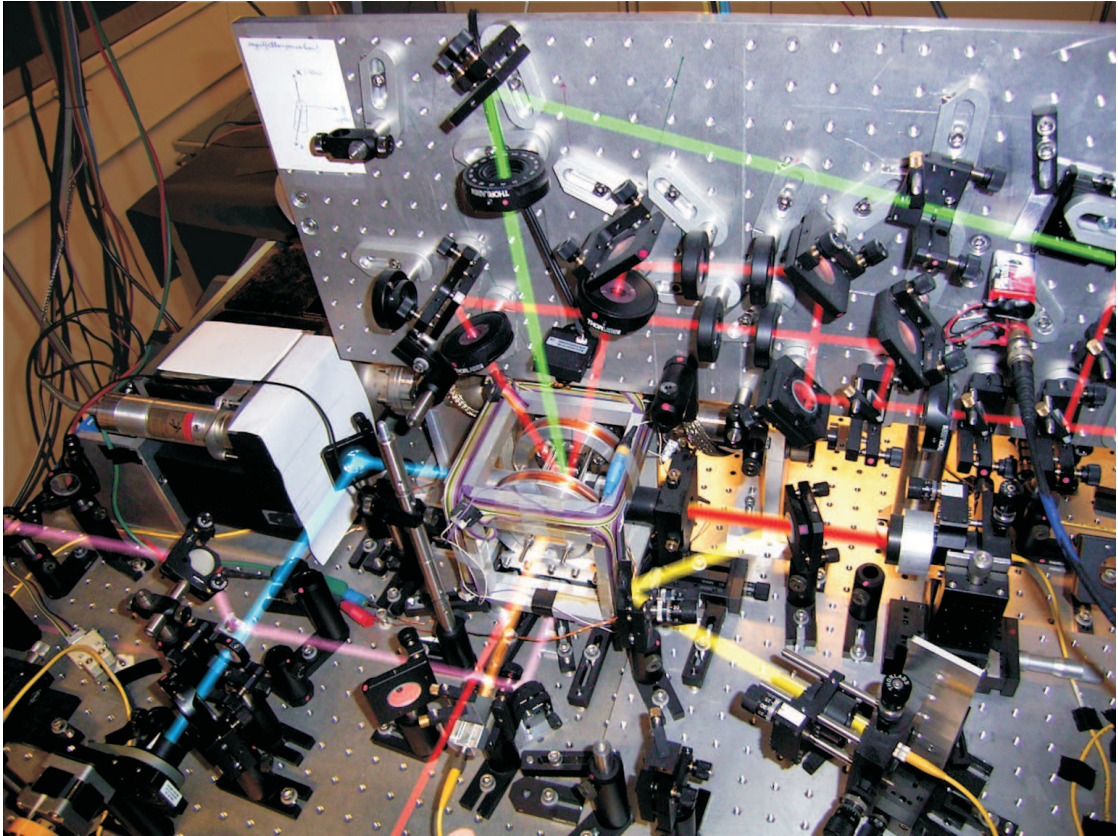
Figure A.4.: Photo of the main part of the experimental setup. The center of the picture shows the experimental area with the glass cell connected to the UHV-chamber. The depicted beams are the dipole trap laser (yellow), atomic fluorescence (red), laser cooling beams (red), optical pumping light (magenta), atomic excitation beam (orange), projection laser (green) and STIRAP laser system (blue). Picture courtesy of Wenjamin Rosenfeld.

A.8. Publications

Publications related to the presented work:

- *Observation of Entanglement of a Single Photon with a Trapped Atom.*
  J. Volz, M. Weber, D. Schlenk, W. Rosenfeld, J. Vrana, K. Saucke, C. Kurtsiefer, and H. Weinfurter
  Phys. Rev. Lett. **96**, 030404 (2006)

- *Analysis of a Single Atom Dipole Trap*
  M. Weber, J. Volz, K. Saucke, C. Kurtsiefer, and H. Weinfurter
  Phys. Rev. A **73**, 043406 (2006).

Bibliography

[1] A. Einstein, B. Podolsky, and N. Rosen. Can quantum-mechanical description of physical reality be considered complete? *Phys. Rev.*, **47**:777–780, 1935.

[2] J. S. Bell. On the Einstein-Podolsky-Rosen paradox. *Physics*, **1**:195, 1964.

[3] D. Bohm. *Quantum Theory*. Prentice-Hall, Englewood Cliffs, New York, 1951.

[4] J. F. Clauser, M. A. Horne, A. Shimony, and R. A. Holt. Proposed experiment to test local hidden-variable theories. *Phys. Rev. Lett.*, **23**:880–884, 1969.

[5] Bell J. *Foundations of Quantum Mechanics*. Academic, New York, 1971.

[6] J. F. Clauser and M. A. Horne. Experimental consequences of objective local theories. *Phys. Rev. D*, **10**:526, 1974.

[7] S. J. Freedman and J. F. Clauser. Experimental test of local hidden-variable theories. *Phys. Rev. Lett.*, **28**:938–941, 1972.

[8] J. F. Clauser and A. Shimony. Bell's theorem: experimental tests and implications. *Rep. Prog. Phys.*, **41**:1881–1927, 1978.

[9] A. Aspect, P. Grangier, and G. Roger. Experimental tests of realistic local theories via Bell's theorem. *Phys. Rev. Lett.*, **47**:460–463, 1981.

[10] A. Aspect, P. Grangier, and G. Roger. Experimental realization of Einstein-Podolsky-Rosen-Bohm Gedankenexperiment: A new violation of Bell's inequalities. *Phys. Rev. Lett.*, **49**:91–94, 1982.

[11] A. Aspect, J. Dalibard, and G. Roger. Experimental test of Bell's inequalities using time-varying analyzers. *Phys. Rev. Lett.*, **49**:1804–1807, 1982.

[12] Bell J. *Speakable and unspeakable in quantum mechanics*. University Press, Cambridge, 1993.

[13] E. Santos. Critical analysis of the empirical tests of local hidden-variable theories. *Phys. Rev. A*, **46**:3646–3656, 1992.

[14] G. Weihs, T. Jennewein, C. Simon, H. Weinfurter, and A. Zeilinger. Violation of Bell's inequality under strict Einstein locality conditions. *Phys. Rev. Lett.*, **81**:5039–5043, 1998.

[15] P. Pearle. Hidden-variable example based upon data rejection. *Phys. Rev. D*, **2**:1418–1425, 1970.

[16] E. Santos. Constraints for the violation of the Bell inequality in Einstein-Podolsky-Rosen-Bohm experiments. *Phys. Lett. A*, **200**:1–6, 1995.

[17] M. A. Rowe, D. Kielpinsky, V. Meyer, C. A. Sacket, W. M. Itano, C. Monroe, and D. J. Wineland. Experimental violation of a Bell's inequality with efficient detection. *Nature*, **409**:791–794, 2001.

[18] R. Garcia-Patron, J. Fiurasek, N. J. Cerf, J. Wenger, R. Tualle-Brouri, and P. Grangier. Proposal for a loophole-free Bell test using homodyne detection. *Phys. Rev. Lett.*, **93**:130409 1–4, 2004.

[19] D. M. Greenberger, M. Horne, and A. Zeilinger. A Bell theorem without inequalities for two particles, using inefficient detectors. *arXiv:quant-ph/0510207*, 2005.

[20] M. Zukowski, A. Zeilinger, M. A. Horne, and A. K. Ekert. "Event-ready-detectors" Bell experiment via entanglement swapping. *Phys. Rev. Lett.*, **71**:4287–4290, 1993.

[21] K. Saucke. Optische Dipolfalle für Einzelatome. Master's thesis, Ludwig-Maximilians-Universität München, 2002.

[22] C. Simon and T. M. Irvine. Robust long-distance entanglement and a loophole-free test with ions and photons. *Phys. Rev. Lett.*, **91**:110405 1–4, 2003.

[23] I. Chuang and M. Nielsen. *Quantum computation and quantum information*. Cambridge University Press, Cambridge, 2000.

[24] D. Bouwmeester, A. Ekert, and A. Zeilinger. *The Physics of Quantum Information*. Springer-Verlag, Berlin, Heidelberg, 2000.

[25] Z. Zhao, Y.-A. Chen, A.-N. Zhang, T. Yang, H.-J. Briegel, and J.-W. Pan. Experimental demonstration of five-photon entanglement and open-destination teleportation. *Nature*, **430**:54–58, 2004.

[26] N. Kiesel, C. Schmidt, U. Weber, G. Tóth, O. Gühne, R. Ursin, and H. Weinfurter. Experimental analysis of a four-qubit photon cluster state. *Phys. Rev. Lett.*, **95**:210502 1–4, 2005.

[27] P. Walther, K. J. Resch, T. Rudolph, E. Schenck, H. Weinfurter, V. Vedral, M. Aspelmeye, and A. Zeilinger. Experimental one-way quantum computing. *Nature*, **434**:169–176, 2005.

[28] R. G. Häffner, W. Hänsel, C. F. Roos, J. Benhelm, D. Chek-al kar, M. Chwalla, T. Körber, U. D. Rapol, M. Riebe, P. O. Schmidt, C. Becher, O. Gühne, W. Dur, and R. Blatt. Scalable multiparticle entanglement of trapped ions. *Nature*, **438**:643–646, 2005.

[29] D. Leibfried, E. Knill, S. Seidelin, J. Britton, R. B. Blakestad, J. Chiaverini, D. B. Hume, W. M. Itona, J. D. Jost, C. Langer, R. Ozeri, R. Reichle, and D. J. Wineland. Creation of a six-atom 'Schrödinger cat' state. *Nature*, **438**:639–642, 2005.

[30] M. Greiner, O. Mandel, T. Esslinger, T. W. Hänsch, and I. Bloch. Quantum phase transition from a superfluid to a Mott insulator in a gas of ultracold atoms. *Nature*, **415**:39–44, 2002.

[31] A. Ekert. Quantum cryptography based on Bell's theorem. *Phys. Rev. Lett.*, **67**:661–663, 1991.

[32] C. H. Bennett, G. Brassard, C. Crépeau, R. Jozsa, A. Peres, and W. K. Wootters. Teleporting an unknown quantum state via dual classical and Einstein-Podolsky-Rosen channels. *Phys. Rev. Lett.*, **70**:1895–1899, 1993.

[33] D. Bouwmeester, J.-W Pan, K. Mattle, M. Eibl, Weinfurterm H., and Zeilinger. Experimental quantum teleportation. *Nature*, **390**:575–579, 1997.

[34] J.-W. Pan, D. Bouwmeester, H. Weinfurter, and A. Zeilinger. Experimental entanglement swapping: Entangling photons that never interacted. *Phys. Rev. Lett.*, **80**:3891–3894, 1998.

[35] K. Mattle, H. Weinfurter, P. G. Kwiat, and A. Zeilinger. Dense coding in experimental quantum communication. *Phys. Rev. Lett.*, **76**:4656–4659, 1996.

[36] C. F. Roos, M. Riebe, H. Häffner, W. Hänsel, J. Benhelm, G. P. T. Lncaster, C. Becher, F. Schmidt-Kaler, and R. Blatt. Control and measurement of three qubit entangled states. *Science*, **304**:1478–1480, 2004.

[37] J. Chiaverini, J. Britton, D. Leibfried, E. Knill, M. D. Barrett, R. B. Blakestad, W. M. Itano, J. D. Jost, C. Lange, R. Ozeri, T. Schaetz, and D. J. Wineland. Implementation of the semiclassical quantum Fourier transform in a scalable system. *Science*, **308**:997–1000, 2005.

[38] D. Schrader, I. Dotsenko, M. Khudaverdyan, Y. Miroshnychenko, A. Rauschenbeutel, and D. Meschede. Neutral atom quantum register. *Phys. Rev. Lett.*, **93**:150501 1–4, 2004.

[39] R. Raussendorf and H.-J. Briegel. A one-way quantum computer. *Phys. Rev. Lett.*, **86**:5188–5191, 2001.

[40] H.-J. Briegel, W. Dür, J. I. Cirac, and P. Zoller. Quantum repeaters: The role of imperfect local operations in quantum communication. *Phys. Rev. Lett.*, **81**:5932–5935, 1998.

[41] X. Maître, E. Hagley, Noguesm G., C. Wunderlich, P. Goy, M. Brune, J. M. Raimond, and S. Haroche. Quantum memory with a single photon cavity. *Phys. Rev. Lett.*, **79**:769–772, 1997.

[42] Matsukevich D. N. and A. Kuzmich. Quantum state transfer between matter and light. *Science*, **306**:663–666, 2004.

[43] B. Julsgaard, J. Sherson, J. I. Cirac, J. A. Fiurasek, and E. S. Polzik. Experimental demonstration of quantum memory for light. *Nature*, **432**:482–486, 2004.

[44] A. Auffeves, P. Maioli, T. Meunier, S. Gleyzes, G. Nogues, M. Brune, J. M. Raimond, and S. Haroche. Entanglement of a mesoscopic field with an atom induced photon graininess in a cavity. *Phys. Rev. Lett.*, **91**:230405 1–4, 2003.

[45] D. N. Matsukevich, T. Chanelieére, M. Bhattacharya, S.-Y. Lan, S. D. Jenkins, T. A. B. Kennedy, and A. Kuzmich. Entanglement of a photon and a collective atomic excitation. *Phys. Rev. Lett.*, **95**:040405, 2005.

[46] B. B. Blinov, D. L. Moehring, L.-M. Duan, and C. Monroe. Observation of entanglement between a single trapped atom and a single photon. *Nature*, **428**:153–157, 2004.

[47] J. Oreg, F. T. Hioe, and J. H. Eberly. Adiabatic following in multilevel systems. *Phys. Rev. A*, **29**:690–697, 1984.

[48] J. R. Kuklinski, U. Gaubatz, F. T. Hioe, and K. Bergmann. Adiabatic population transfer in a three-level system driven by delayed laser pulses. *Phys. Rev. A*, **40**:6741–6744, 1989.

[49] G. W. Coulston and K. Bergmann. Population transfer by stimulated Raman scattering with delayed pulses: Analytic results for multilevel systems. *J. Chem. Phys.*, **96**:3467–3475, 1991.

[50] T. A. Laine and S. Stenholm. Adiabatic processes in three-level systems. *Phys. Rev. A*, **53**:2501–2512, 1996.

[51] N. V. Vitanov and S. Stenholm. Population transfer via a decaying state. *Phys. Rev. A*, **56**:1463–1471, 1997.

[52] N. V. Vitanov and S. Stenholm. Ananlytic properties and effective two-level problems in stimulated Raman adiabatic passage. *Phys. Rev. A*, **55**:648–660, 1997.

[53] S. L. Braunstein, A. Mann, and M. Revzen. Maximal violation of Bell inequalities for mixed states. *Phys. Rev. Lett.*, **68**:3259–3261, 1992.

[54] N. Bohr. Can quantum-mechanical description of physical reality be considered complete? *Phys. Rev.*, **48**:696–702, 1935.

[55] E. Schrödinger. Die gegenwärtige Situation in der Quantenmechanik. *Naturwissenschaften*, **23**:807–849, 1935.

[56] D. C. Burnham and D. L. Weinberg. Observation of simultaneity in parametric production of optical photon pairs. *Phys. Rev. Lett.*, **25**:84–87, 1970.

[57] J. G. Rarity and P. R. Tapster. Experimental violation of Bell's inequality based on phase and momentum. *Phys. Rev. Lett.*, **64**:2495–2498, 1990.

[58] P. G. Kwiat, K. Mattle, H. Weinfurter, A. Zeilinger, A. V. Sergienko, and Y. Shih. New high-intensity source of polarization entangled photon pairs. *Phys. Rev. Lett.*, **75**:4337–4341, 1995.

[59] M. O. Scully and M. Zubairy. *Quantum Optics*. Cambridge University Press, Cambridge, 1997.

[60] J. D. Jackson. *Classical electrodynamics*. Wiley, New York, 1962.

[61] D. E. Pritchard, E. L. Raab, V. S. Bagnato, C. E. Wieman, and R. N. Watts. Light traps using spontaneous forces. *Phys. Rev. Lett.*, **57**:310–313, 1986.

[62] E. L. Raab, E. L. Prentiss, A. Cable, S. Chu, and D. E. Pritchard. Trapping of neutral sodium atoms with radiation pressure. *Phys. Rev. Lett.*, **59**:2631–2634, 1987.

[63] A. L. Migdall, J. V. Prodan, W. D. Phillips, T. H. Bergemann, and H. J. Metcalf. First observation of magnetically trapped neutral atoms. *Phys. Rev. Lett.*, **54**:2596–2599, 1985.

[64] T. H. Bergeman, G. Erez, and H. J. Metcalf. Magnetostatic trapping fields for neutral atoms. *Phys. Rev. A*, **35**:1535–1545, 1987.

[65] S. Chu, J. E. Bjorkholm, A. Ashkin, and A. Cable. Experimental observation of optically trapped atoms. *Phys. Rev. Lett.*, **57**:314–317, 1986.

[66] R. Grimm, M. Weidemüller, and Y. B. Ovchinnikov. Optical dipole traps for neutral atoms. *Adv. At. Mol. Opt. Phys.*, **42**:95, 2000.

[67] H. J. Metcalf and P. van Straten. *Laser Cooling and Trapping*. Springer, New York, Berlin, Heidelberg, 1999.

[68] M. Weber. *Quantum Optical Experiments towards Atom-Photon Entanglement*. PhD thesis, Ludwig-Maximilians-Universität München, 2005.

[69] N. Schlosser, G. Reymond, I. Protsenko, and P. Grangier. Sub-poissonian loading of single atoms in a microscopic dipole trap. *Nature*, **411**:1024–1027, 2001.

[70] N. Schlosser, G. Reymond, and P. Grangier. Collisional blockade in microscopic optical dipole traps. *Phys. Rev. Lett.*, **89**:023005, 2002.

[71] J. Dalibard and W. Philips. Stability and damping of radiation pressure traps. *Bull. Am. Phys. Soc.*, **30**:748, 1985.

[72] S. Chu, L. Hollberg, J. E. Bjorkholm, A. Cable, and A. Ashkin. Three-dimensional viscous confinement and cooling of atoms by resonance radiation pressure. *Phys. Rev. Lett.*, **55**:48–51, 1985.

[73] P. D. Lett, R. N. Watts, C. E. Tanner, A. L. Rolston, W. D. Philips, and C. I. Westbrook. Optical molasses. *J. Opt. Soc. Am B*, **6**:2084–2107, 1989.

[74] J. Dalibard and C. Cohen-Tannoudji. Laser cooling below the Doppler limit by polarization gradients: Simple theoretical models. *J. Opt. Soc. Am. B*, **6**:2023–2045, 1989.

[75] D. A. Steck. Rubidium 87 D Line Data. *http://steck.us/alkalidata*.

[76] S. D. Gensemer, P. L. Gould, P. J. Leo, E. Tiesinga, and C. J. Williams. Ultracold ^{87}Rb ground-state hyperfine-changing collisions in the presence and absence of laser light. *Phys. Rev. A*, **62**:030702, 2000.

[77] R. C. Nesnidal and T. G. Walker. Light-induced ultracold spin-exchange collisions. *Phys. Rev. A*, **62**:030701, 2000.

[78] S. J. M. Kuppens, K. L. Corwin, K. L. Miller, T. E. Chupp, and C. E. Wieman. Loading an optical dipole trap. *Phys. Rev. A*, **62**:013406, 2000.

[79] R. Hanbury Brown and R. Q. Twiss. *Nature*, **177**:27, 1956.

[80] R. Loudon. *The Quantum Theory of Light*. Oxford Univ. Press, Oxford, 2001.

[81] C. Cohen-Tannoudji, J. Dupont-Roc, and G. Grynberg. *Atom-Photon Interactions, Basic Processes and Applications*. Wiley, New York, 1998.

[82] M. Schubert, I. Siemers, R. Blatt, W. Neuhauser, and P. E. Toschek. Photon antibunching and non-Poissonian fluorescence of a single three-level ion. *Phys. Rev. Lett.*, **68**:3016–3019, 1992.

[83] S. Reynaud. *Ann. Phys. (Paris)*, **8**:351, 1983.

[84] V. Gomer, B. Ueberholz, F. Knappe, F. Strauch, D. Frese, and D. Meschede. *Appl. Phys. B*, **67**:689–697, 1998.

[85] T. Legero, T. Wilk, M. Hennrich, G. Rempe, and A. Kuhn. Quantum beat of two single photons. *Phys. Rev. Lett.*, **93**:070503, 2004.

[86] F. Schuda, C. Stroud Jr, and M. Hercher. Observation of the resonant Stark effect at optical frequencies. *J. Phys. B*, **7**:L198, 1974.

[87] F. Y. Wu, R. E. Grove, and S. Ezekiel. Investigation of the spectrum of resonance fluorescence induced by a monochromatic field. *Phys. Rev. Lett.*, **35**:1426–1429, 1975.

[88] R. E. Grove, F. Y. Wu, and S. Ezekiel. Measurement of the spectrum of resonance fluorescence from a two-level atom in an intense monochromatic field. *Phys. Rev. Lett.*, **15**:227–233, 1977.

[89] W. Hartig, W. Rasmussen, R. Schieder, and H. Walther. Study of the frequency distribution of the fluorescent light induced by monochromatic radiation. *Z. Phys. A*, **278**:205–210, 1976.

[90] H. M. Gibbs and T. N. C. Ventkatesan. Direct observation of fluorescence narrower than the natural linewidth. *Opt. Commun.*, **17**:87, 1976.

[91] C. I. Westbrook, R. N. Watts, C. E. Tanner, S. L. Rolston, W. D. Phillips, and P. D. Lett. Localization of atoms in a three-dimensional standing wave. *Phys. Rev. Lett.*, **65**:33–36, 1990.

[92] P. S. Jessen, C. Gerz, P. D. Lett, W. D. Phillips, S. L. Rolston, R. J. C. Spreeuw, and C. I. Westbrook. Observation of quantized motion of Rb atoms in an optical field. *Phys. Rev. Lett.*, **69**:49–52, 1992.

[93] Y. Stalgies, I. Siemers, B. Appasamy, T. Altevogt, and P. E. Toschek. The spectrum of single-atom resonance fluorescence. *Europhys. Lett.*, **35**:259–264, 1996.

[94] J. T. Höffges, H. W. Baldauf, W. Lange, and H. Walther. Heterodyne measurement of the resonance fluorescence of a single ion. *J. Mod. Opt.*, **44**:1999–2010, 1997.

[95] J. T. Höffges, H. W. Baldauf, T. Eichler, S. R. Helmfrid, and H. Walther. Heterodyne measurement of the fluorescent radiation of a single trapped ion. *Opt. Commun.*, **133**:170–174, 1997.

[96] B. R. Mollow. Power spectrum of light scattered by two-level systems. *Phys. Rev.*, **188**:1969–1975, 1969.

[97] T. Legero, A. Wilk, A. Kuhn, and G. Rempe. Characterization of single photons using two-photon interference. *arXiv:quant-ph/0512023*, 2005.

[98] R. G. Unanyan, M. Fleischhauer, B. W. Shore, and K. Bergmann. Robust creation and phase-sensitive probing of superposition states via stimulated Raman adiabatic passage (STIRAP) with degenerate dark states. *Opt. Commun.*, **155**:144–154, 1998.

[99] H. Theuer, R. G. Unanyan, C. Habscheid, K. Klein, and K. Bergmann. Novel laser controlled variable matter wave beamsplitter. *Opt. Exp.*, **4**:77–83, 1999.

[100] R. G. Unanyan, B. W. Shore, and K. Bergmann. Laser-driven population transfer in four-level atoms: Consequences of non-Abelian geometrical adiabatic phase factors. *Phys. Rev. A*, **59**:2910–2919, 1999.

[101] F. Vewinger, M. Heinz, R. G. Fernandez, V. Vitanov, and K. Bergmann. Creation and measurement of a coherent superposition of quantum states. *Phys. Rev. Lett.*, **91**:213001, 2003.

[102] H. Dehmelt. *Bull. Am. Phys. Soc.*, **20**:60, 1975.

[103] J. Vrana. State selective Detection of a Single Atom. Master's thesis, Ludwig-Maximilians-Universität München, 2004.

[104] D. Schlenk. Atom-Photon Verschränkung. Master's thesis, Ludwig-Maximilians-Universität München, 2004.

[105] U. Fano. Description of states in quantum mechanics by density matrix and operator techniques. *Rev. Mod. Phys.*, **29**:74–93, 1957.

[106] D. Boschi, S. Branca, F. de Martini, L. Hardy, and A. Popescu. Experimental realization of teleporting an unknown pure quantum state via dual classical and Einstein-Podolsky-Rosen Channels. *Phys. Rev. Lett.*, **80**:1121–1125, 1998.

[107] A. K. Pati. Remote state preparation and measurement of a single photon. *arXiv:quant-ph/0212164*, 2002.

[108] T. B. Pittman and J. D. Franson. Violation of Bell's inequality with photons from independent sources. *Phys. Rev. Lett.*, **90**:240401, 2003.

[109] T. Jennewein, G. Weihs, J.-W. Pan, and A. Zeilinger. Experimental nonlocality proof of quantum teleportation and entanglement swapping. *Phys. Rev. Lett.*, **88**:017903, 2002.

[110] W. Dürr, H.-J. Briegel, J. I. Cirac, and P. Zoller. Quantum repeaters based on entanglement purification. *Phys. Rev. A*, **59**:169–181, 1999.

[111] J. Lehn and H. Wegmann. *Einführung in die Statistik*. Teubner Studienbücher, 2000.

[112] C. Kurtsiefer. *A programmable pattern generator.*, 2002. unpublished.

Danksagung

An dieser Stelle möchte ich mich bei allen Personen bedanken, die zum gelingen dieser Arbeit beigetragen haben. Zuallererst gilt mein Dank meinem Doktorvater Harald Weinfurter, der es mir ermöglicht hat an diesem faszinierenden Projekt zu arbeiten und der immer für Fragen offen war, uns gleichzeitig aber viel Freiraum gelassen hat in der Realisierung des Experiments. Mein besonderer Dank gilt meinem langjährigen Kollegen Markus Weber, für die vielen spannenden und abwechslungsreichen Stunden, die wir damit verbracht haben dieses Experiment aufzubauen (und für seinen durch nichts zu erschütternden Optimismus, mit dem er einem auch in den frustrierendsten Momenten immer wieder Mut gemacht hat).

Weiterhin möchte ich mich bei Christian Kurtsiefer bedanken, der (nicht zuletzt durch das Design der Elektronik) viel zum Gelingen unseres Experiments beigetragen hat und immer für physikalische Diskussionen offen war. Ein herzliches Dankeschön gilt allen an der erfolgreichen Realisierung dieses Experiment beteiligten Personen: Karen Saucke, die mit uns an diesem Projekt die etwas schleppende Anfangszeit durchgemacht hat, Johannes Vrana und meinem Mitschwaben Daniel Schlenk, der sich beim Experiment und bei vielen anderen Dingen als guter Schüler erwies und mir immer für einen strategischen Überredungsversuch zur Seite stand. Ein besonderer Dank gilt Wenjamin Rosenfeld, dessen Ausdauer bei den langen Nacht- und Wochenendmessungen die guten Resultate möglich machte und der immer bereit war zu ausgiebigen physikalischen Diskussionen. Bei den neuen Mitgliedern am Experiment: Stefan Berner, Peter Krebs, Florian Henkel und Michael Krug möchte ich mich besonders für die vielen interessanten Fragen, die mich von der Monotonie des Schreibens abgelenkt haben, bedanken und für deren Geduld hinsichtlich der Fertigstellung meiner Arbeit.

Desweiteren bedanke ich mich bei meinen ehemaligen Zimmergenossen Oliver Schulz, Henning Weier und Chunlang Wang für ihre Beratung bei den häufigen Computerproblemen und die vielen physikalischen Diskussionen, die sie mit mir durchführen mussten. Ein besonderer Dank geht an Nadja Regner und Martin Fürst für ihre großen Verdienste bei der Sicherstellung der Versorgung der Gruppe (Nadja, danke für den Kuchen [104]) und an unseren verdienten Schwaben ehrenhalber (und Meister der Timestamp-Karte) Tobias Schmitt-Manderbach.

Zum Schluss noch ein Dankeschön an alle momentanen und ehemaligen Mitarbeiter der AG Weinfurter: Asli Ugur, Carsten Schuck, Christian Schmid, Christoph Braig, Gerhard Huber, Ivan Ordavo, Julia Lau, Johannes Schachaneder, Magdalena Kaminska, Manfred Eibl, Markus Oberparleiter, Matthäus Halder, Mohamed Bourennane, Nikolai Kiesel, Patrick Zarda, Pavel Trojek, Ruprecht Steinhübl, Sascha Gärtner, Sonja Mayer, Ulrich Weber, Witlef Wieczorek und Yousef Nazirizadeh für deren Hilfe bei diversen Problemen und ihre (teils unfreiwillige) Großzügigkeit im Umgang mit optischen und mechanischen Komponenten. Ebenso gilt mein